Topological proximity effect in bilayer systems and stochastic approach to interacting topological phases

Philipp Wilhelm Klein

INSTITUT POLYTECHNIQUE DE PARIS

NNT : 2021IPPAX058

Thèse de doctorat

Topological proximity effect in bilayer systems and stochastic approach to strongly correlated topological phases

Thèse de doctorat de l'Institut Polytechnique de Paris
préparée à l'École Polytechnique

École doctorale n°626
École doctorale de l'Institut Polytechnique de Paris (EDIPP)
Spécialité de doctorat : Physique de la matière condenseé

Thèse présentée et soutenue à Palaiseau, le 08 septembre 2021, par

PHILIPP WILHELM KLEIN

Composition du Jury :

Sylvain Capponi Professor, LPT, Université de Toulouse	Président
Nathan Goldman Professor, CENOLI, Université Libre de Bruxelles (ULB)	Rapporteur
Mark-Oliver Goerbig Directeur de Recherche, LPS, Université Paris-Sud	Rapporteur
Thierry Jolicoeur Directeur de Recherche, Institut de Physique Théorique, CEA Scalay	Examinateur
Luca Perfetti Professor, LSI, École Polytechnique	Examinateur
Tim Ziman Directeur de Recherche, LPMC, Institut Laue Langevin	Examinateur
Karyn Le Hur Directrice de Recherche, CPHT, École Polytechnique	Directrice de thèse
Silke Biermann Professor, CPHT, École Polytechnique	Invitée

Contents

Chapter 1

Introduction

A phase of matter is a region in the corresponding physical parameter space throughout which all physical properties of a material are essentially uniform [1]. Landau was able to establish a classification mechanism for different phases of matter on the basis of symmetries underlying the physical system [2, 3]. The notion of the Landau paradigm is that while physical systems are *disordered* at high temperatures, they do acquire *order* due to spontaneous symmetry breaking below a critical temperature T_c. That means that below T_c a local magnetic order parameter becomes finite, such that the system establishes some long-range order. Quantitatively, the symmetry breaking can be captured by the behavior of a local order parameter at the phase transition. At a first order phase transition the local order parameter changes discontinuously, whereas at a second order phase transition the change is continuous [4, 5].

Von Klitzing [6] described in 1980 the quantization of the Hall conductivity in a two dimensional electron gas that was exposed to an external magnetic field. This effect, known as the Integer Quantum Hall Effect (IQHE), is one of the most important discoveries that describes physics *beyond* the Landau paradigm.

As it turns out, the classification of a Quantum hall phase cannot rely on some *local* order parameter. Rather, it became clear that a different kind of mechanism

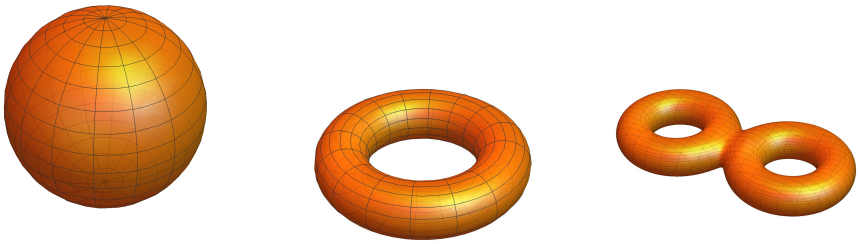

FIGURE 1.1: Topological manifolds with different genera g. Left: A sphere with $g = 0$. Middle: A torus with $g = 1$. Right: A double-torus with $g = 2$.

is at play that involves *global* properties of the underlying wave function. Mathematically, the field of *topology* came into play.

Topology is the mathematical study that is concerned with the description and classification of the shape of things. Topology considers two mathematical objects as equivalent as long as they can be continuously deformed into each other, i.e. there is a continuous map between them [7]. In the pursuit of classifying ground states in the absence of symmetry breaking, a phase obeys *topological order* when the degeneracy of the ground state depends on the topology of the underlying manifold [8]. More specifically, the ground state degeneracy is 2^{2g} where g is the genus of the manifold [9]. The genus of a connected, orientable surface is an integer representing the maximum number of cuttings along non-intersecting closed simple curves without cutting the surface into pieces [10]. More intuitively, the genus g counts the number of *holes* in a manifold, see Fig. 1.1.

Based on the topology of the lattice, the ground state of a system with topological order can be separated into different topological sectors [8]. Each sector corresponds to a distinct ground state wave function which contributes to the degeneracy of the ground state. The *global* nature of topological order is expressed in the fact that there is no local order parameter which can account for the ground

state degeneracy (based on all wave functions of all sectors), and therefore, Landaus theory is not applicable [11, 8, 9].

In this thesis

In chapter 2, we introduce the reader to the main concepts of topological band theory, graphene as a Dirac metal and the Haldane honeycomb model - the prototypical model of a Chern insulator. First, we review the main concepts of Berry phases [12] and introduce based on them the notion of Berry curvature and the first Chern number. Furthermore, we recap the gauge independent computation of those quantities on a discrete lattice.

Afterwards, we introduce the concept of a Dirac metal at the example of graphene [13]. We dive into its mathematical description within a tight binding approach and flesh out its rich low energy phenomenology.

Then, we follow in the footsteps of Haldane [14] and explore his path to finding a way to realize a quantum Hall effect without the application of an external magnetic field in a sheet of graphene.

In chapter 3, we reveal a proximity effect between a topological band (Chern) insulator described by a Haldane model and spin-polarized Dirac particles of a graphene layer. We show that by coupling these two systems weakly (i.e. by proximity), we are able to induce non-trivial topology in the bulk of the graphene layer. We dive deep the underlying mechanisms and explore in detail the rich phenomenology of this system. Importantly, we present experimental protocols designed to reveal the effects described mathematically. In particular, we propose a generalized Haldane bilayer model that is designed to observe the topological proximity effect in a cold atom experimental setup.

In chapter 4, we leave the realm of exactly solvable models and consider strong correlations in a Chern insulator. During the past decade some progress

has been made in the description of interacting Chern systems, in the bosonic case [15, 16], and both for spinless [15, 17, 18, 19] and spinfull [20, 21, 22, 23, 24] systems. However, the system we wish to study in this chapter, i.e. the *spinless* interacting Haldane model has not been convincingly solved by means of an approximative model. Therefore, we develop a new stochastic description of the topological properties of the Haldane honeycomb model in the presence of strong interactions. We confirm the Mott transition's first-order nature which has been previously speculated [15] by means of a variational mean-field approach supported by density matrix renormalization group results and Ginzburg-Landau arguments.

Most importantly, we introduce a new quantity dubbed *stochastic Chern number* which provides a measure for the topology in the system in the presence of strong correlations. In particular, this quantity counts stochastically the number of particle hole pairs produced due to interaction effects which act on the ground state Chern number. We utilize the dichroism of light to build a bridge in quantifying excited quasi particles and show an analogy between interaction-induced particle- hole pairs and temperature effects.

Finally, in chapter 5, we revisit the Kane-Mele-Hubbard model. Similarly to the interacting Haldane model in chapter 4, we develop a variational approach to strong-correlated $\mathbb{Z}_2$ topological insulator. We present two different methods to calculate the Mott transition. In particular we point out an analytical approach starting from our stochastic decoupling scheme that allows to describe the Mott transition line with one equation.

Thesis publications

The following research papers have been published as peer reviewed articles or pre-prints during the preparation of this thesis.

Peng Cheng et al. "Topological proximity effects in a Haldane graphene bilayer system". In: *Phys. Rev. B* 100 (8 2019), p. 081107. DOI: 10.1103/PhysRevB.100.081107. URL: https://link.aps.org/doi/10.1103/PhysRevB.100.081107

Philipp W. Klein, Adolfo G. Grushin, and Karyn Le Hur. "Interacting stochastic topology and Mott transition from light response". In: *Phys. Rev. B* 103 (3 2021), p. 035114. DOI: 10.1103/PhysRevB.103.035114. URL: https://link.aps.org/doi/10.1103/PhysRevB.103.035114

Joel Hutchinson, Philipp W. Klein, and Karyn Le Hur. "Analytical approach for the Mott transition in the Kane-Mele-Hubbard model". In: *Phys. Rev. B* 104 (7 2021), p. 075120. DOI: 10.1103/PhysRevB.104.075120. URL: https://link.aps.org/doi/10.1103/PhysRevB.104.075120

Chapter 2

Concepts of topological band theory

2.1 Topology in condensed matter physics

2.1.1 The Berry Phase

Consider some time-varying Hamiltonian $\mathcal{H}(\boldsymbol{R})$ where is $\boldsymbol{R} \equiv \boldsymbol{R}(t)$ is a vector of parameters that depends on time. Now, we want to investigate the evolution of the system when moving adiabatically, i.e. slowly in comparison to other energy scales [11] along some path through parameter space. To this end, we diagonalize the Hamiltonian $\mathcal{H}(\boldsymbol{R})$ at each point in the parameter space and orthonormal eigenbasis $|n(\boldsymbol{R})\rangle$. In fact, the eigenbasis $|n(\boldsymbol{R})\rangle$ can be determined up to a phase factor. In order to avoid arbitrariness (which can be interpreted as choice of *gauge*) of this phase factor, we require the phase to evolve smoothly when moving along a path in parameter space spanned by the components of the parameter vector $\boldsymbol{R}$.

Now assume that we start moving along a path in parameter space, where we start with the inital eigenstate $|n(\boldsymbol{R}(0))\rangle$. According to the adiabatic theorem [28], the system described by the Hamiltonian $\mathcal{H}(\boldsymbol{R})$ and starting in the inital, instantaneous eigenstate $|n(\boldsymbol{R}(0))\rangle$ will along an adiabatic drive through parameter space remain in its eigenstate. Now, we assume that the phase factor mentioned

above is indeed the only degree of freedom that remains to be computed [11]. Let us define the phase factor $\theta(t)$ as [12, 11]

$$|\Psi\rangle = \exp(-i\theta(t))|n(\boldsymbol{R}(t))\rangle. \tag{2.1}$$

Therefore, the energy evolution of the system is described by the equation [11]

$$\mathcal{H}(\boldsymbol{R}(\boldsymbol{t}))|\Psi\rangle = i\hbar\frac{\mathrm{d}}{\mathrm{d}t}|\Psi\rangle. \tag{2.2}$$

The phase $\theta(t)$ can in fact not be zero, since it needs to contain at least capture the energetic evolution of the eigenstate through parameter space, the so-called *dynamic phase* [28]. To our surprise, solving the differential equation associated with Eq. 2.2 [11] yields more than that, i.e.

$$\theta(t) = \frac{1}{\hbar}\int_0^t E_n(\boldsymbol{R}(t'))\mathrm{d}t' - i\int_0^t \langle n(\boldsymbol{R}(t'))|\frac{\mathrm{d}}{\mathrm{d}t}|n(\boldsymbol{R}(t')\rangle \mathrm{d}t'. \tag{2.3}$$

The first term is the dynamic phase related to an energy integral. The second part is an - a priori - unexpected term which is called the *Berry phase* which we denote by γ_{Berry}, i.e.

$$\gamma_{Berry} = i\int_0^t \langle n(\boldsymbol{R}(t'))|\frac{\mathrm{d}}{\mathrm{d}t}|n(\boldsymbol{R}(t')\rangle \mathrm{d}t'. \tag{2.4}$$

The Berry phase arises from the fact that the states at t and $t + \mathrm{d}t$ are not identical [11], or in other words, it originates from the geometrical properties of the parameter space of the Hamiltonian [12].

From now on, let us consider only *closed* paths $\mathcal{C}$ in paramter space. First, let us write Eq. 2.4 without the direct time dependance as [11]

$$\gamma_{Berry} = i\oint_{\mathcal{C}} \langle n(\boldsymbol{R})|\nabla_{\boldsymbol{R}}|n(\boldsymbol{R})\rangle \mathrm{d}\boldsymbol{R}. \tag{2.5}$$

Then, we can in analogy to transport on manifolds define the *Berry connection* as

$$\boldsymbol{A}(\boldsymbol{R}) = i\langle n(\boldsymbol{R})|\frac{\partial}{\partial \boldsymbol{R}}|n(\boldsymbol{R}\rangle, \tag{2.6}$$

and then again with this definition the Berry phase is

$$\gamma_{Berry} = \oint_{\mathcal{C}} \mathrm{d}\boldsymbol{R} \cdot \boldsymbol{A}(\boldsymbol{R}). \tag{2.7}$$

Now, we remind ourselves that the eigenstates $|n(\boldsymbol{R})\rangle$ are determined up to a phase, i.e. $|n(\boldsymbol{R})\rangle \rightarrow \exp(i\theta)|n(\boldsymbol{R})\rangle$, where θ is here a smooth function in parameter space $\theta \equiv \theta(\boldsymbol{R})$. From a physical point of view, it would be appropriate to call the Berry connection $\boldsymbol{A}(\boldsymbol{R})$ in fact the *Berry vector potential*. As such, it is gauge dependent according to the the choice of θ, i.e.

$$\boldsymbol{A}(\boldsymbol{R}) \rightarrow \boldsymbol{A}(\boldsymbol{R}) - \frac{\partial\theta(\boldsymbol{R})}{\partial \boldsymbol{R}}. \tag{2.8}$$

Hence, the Berry phase as line integral of the Berry vector potential, Eq. 2.7 changes by [11]

$$\gamma_{Berry} \rightarrow \gamma_{Berry} + \theta(\boldsymbol{R}_0) - \theta(\boldsymbol{R}_1) \tag{2.9}$$

where $\boldsymbol{R}_0$ and $\boldsymbol{R}_1$ are the start and end point of the path $\mathcal{C}$, respectively. Since $\mathcal{C}$ is a closed path, we must have $\boldsymbol{R}_0 = \boldsymbol{R}_1$, and because the eigenstate basis is here chosen single valued [11], we also have $|n(\boldsymbol{R}_0)\rangle = |n(\boldsymbol{R}_1)\rangle$ since we moved along $\mathcal{C}$ adiabatically. Therefore, in the case under consideration here, the only possible solution for the closed path is [11]

$$\theta(\boldsymbol{R}_0) - \theta(\boldsymbol{R}_1) = 2\pi\omega \tag{2.10}$$

where ω must be an integer. The number ω can be interpreted as a *winding number* where the sign of ω determines the orientation with which we move around the

path $\mathcal{C}$

Furthermore, note that in the case of graphene, which we will have a closer look at in chapter 2.2.2, we consider a lattice Hamiltonian with chiral symmetry. We will point out that encircling the so-called Dirac points of the hexagonal lattice will yield Berry phases of $\pm\pi$ such that we can identify these points as topological defects.

2.1.2 Berry curvature, first Chern number and Hall conductivity

For a closed path, we can make use of Stokes theorem [7] so that we can Eq. 2.7 express as

$$\gamma_{Berry} = \oint_{\mathcal{C}} \mathrm{d}\boldsymbol{R} \cdot \boldsymbol{A}(\boldsymbol{R}) = \int_{\mathcal{S}} \mathrm{d}\mathcal{S} \cdot (\nabla_{\boldsymbol{R}} \times \boldsymbol{A}(\boldsymbol{R}))\,. \tag{2.11}$$

Here, we transformaed a line integral along the closed path $\mathcal{C}$ into a surface integral over the surface $\mathcal{S}$ where $\partial\mathcal{S} = \mathcal{C}$. Also, note that we assumed here a two dimensional parameter space such that we could use the rotation operator applied to the Berry connection, i.e. $\nabla_{\boldsymbol{R}} \times \boldsymbol{A}(\boldsymbol{R})$. This expression is called the *Berry curvature* $\mathcal{F}$, i.e.

$$\mathcal{F}(\boldsymbol{R}) \equiv \nabla_{\boldsymbol{R}} \times \boldsymbol{A}(\boldsymbol{R}) \tag{2.12}$$

which reads (in this two dimensional case) explicitly [7, 11]

$$\mathcal{F}_{ij}(\boldsymbol{R}) = \frac{\partial \mathcal{A}_i(\boldsymbol{R})}{\partial \boldsymbol{R}^j} - \frac{\partial \mathcal{A}_j(\boldsymbol{R})}{\partial \boldsymbol{R}^i}. \tag{2.13}$$

We saw previously that the Berry connection needs to be integrated to result a physical quantity, namely the Berry phase. That means, the Berry connection is as vector potential primarily a mathematical tool (in the same way as the electromagnetic vector potential in electrodynamics [29]). On the other hand, the Berry curvature is a gauge-invariant local manifestation of the geometric properties of

the wavefunctions in the parameter space [30]. Hence, we can make the analogy between the Berry curvature and the magnetic field in electrodynamics [29].

Having the notion of the Berry phase and the definition of the Berry curvature at hand, we can now define the *first Chern number*. In direct correspondance with the insight we gained for the Berry phase, cf. Eq. 2.10, we define the first Chern number as [7]

$$C = \frac{1}{2\pi} \int_{\mathcal{S}'} \mathrm{d}\mathcal{S} \;\; \mathcal{F}(\boldsymbol{R}) \tag{2.14}$$

$$= \frac{1}{2\pi} \int_{\mathcal{S}'} \mathrm{d}\mathcal{S} \left(\frac{\partial \mathcal{A}_i(\boldsymbol{R})}{\partial \boldsymbol{R}^j} - \frac{\partial \mathcal{A}_j(\boldsymbol{R})}{\partial \boldsymbol{R}^i} \right). \tag{2.15}$$

Here, the integral is defined over a closed surface $\mathcal{S}'$ (i.e. without boundary). In practice, this surface will be either the sphere or a torus. For example in chapter 2.1.3, we assume the Brillouin to have periodic boundary conditions, such that it can be mapped on a torus. Furthermore, note that we can always make the connection to Eq. 2.11 where $\mathcal{S}$ was a surface with boundary, by cutting the closed surface $\mathcal{S}'$ into two pieces, e.g. the sphere can be cut into two hemispheres.

With our previous discussion of the Berry phase, this formula seems well motivated. From the physical side however, motivating the first Chern number cannot be done without mentioning the Integer Quantum Hall Effect (IQHE) [6]. Von Klitzing [6] realized the IQHE in a two-dimensional electron gas which was exposed to a homogenous magnetic field oriented perpendicular to the gas. Experimentally, it was found that the system is an insulator in the bulk, i.e. longitudinal elements of the conductivity tensor σ vanish, i.e. $\sigma_{xx} = \sigma_{yy} = 0$. On the other hand, the transverse element σ_{xy} was found to be quantized as [11]

$$\sigma_{xy} = \frac{e^2}{h} C \tag{2.16}$$

where C is an integer, and is indeed the first Chern number. The gas being a bulk

insulator, the transverse conductivity must be connected to transport properties at the edges [31]. Indeed, chiral edge modes carry C units $\frac{e^2}{h}$ of conductance, where the sign of C determines the orientation of the edge transport. Mathematically, the connection with first Chern number was described by Thouless, Kohmoto, Nightingale, and de Nijs [32] who showed that the number C could indeed by computed using Eq. 2.15. The first Chern number is therefore sometimes also called the TKNN invariant [31].

One important aspect of a system with a non-zero Chern number is its phenomenology in experimental realizations. The question is, how can it be that we obtain e.g. in a system that shows an IQHE a bulk insulator and a non-zero Hall conductivity which indicates transport taking place in the system [11]. The solution to this question points to the occurence of *edge modes*, i.e. conductive modes that only occur at an interface of the system at hand with another system that has a different topological bulk invariant. While we will at this point only consider the following intuitive argument, we will in the following sections closer look at systems that exhibit such modes, namely the Haldane and Kane-Mele models. If we *create* an edge in a material hosting a bulk non-zero topological number, the material is interfaced with the vacuum which has trivial topological order. This induces a mismatch in terms of topological invariants at the edge which can only be resolved by the system through the creation of gapless edge or surface states [11] . This link between a topological invariant of a system and the emergence of surface states is the bulk-boundary correspondence

2.1.3 Gauge independent numeric computation of the Berry curvature and Chern number

The parameter space $\boldsymbol{R}$ introduced in previous sections, will in practice be for the momentum space in two dimensions. Explicitly, we discretize Eq. 2.14 and 2.15

in momentum space using

$$\boldsymbol{k} = \frac{2\pi}{N}\boldsymbol{l} \tag{2.17}$$

where the Brillouin zone of the momentum space is divided into N discrete points and $l_{x,y} = 1, \ldots, N-1$. Note that we assume periodic boundary conditions for the Brillouin zone such that it can effectively be mapped on a torus. The Chern number[1] and Berry curvature, cf. Eq. 2.14 and 2.15, then read

$$C = \frac{1}{2\pi} \sum_{\boldsymbol{k}\in \mathrm{BZ}} \mathrm{d}k_x \mathrm{d}k_y \;\; \mathcal{F}(\boldsymbol{k}) \tag{2.18}$$

and

$$\mathcal{F}(\boldsymbol{k}) = \frac{\partial \mathcal{A}_x(\boldsymbol{k})}{\partial k_y} - \frac{\partial \mathcal{A}_y(\boldsymbol{k})}{\partial k_x}. \tag{2.19}$$

Although it might be tempting to just use these equations in order to compute the local Berry curvature or the global Chern number, it is unfortunately not that straight forward. The Berry connection $\mathcal{A}$ is *not* gauge independent. In practice, this means that we get a different random phase when we diagonalize the Hamiltonian of the system one by one for each fixed wave vector $\boldsymbol{k}$ such that the resulting eigenstates are not smoothly connected. In order to compute the Berry curvature and Chern number in a gauge independent manner, we follow Ref. [33].

First, we note that we can change the gauge of an eigenstate $|n(\boldsymbol{k})\rangle$ at wave vector $\boldsymbol{k}$ according to U(1) gauge transformation

$$|n(\boldsymbol{k})\rangle \to \exp(i\theta)|n(\boldsymbol{k})\rangle \tag{2.20}$$

where θ is a smooth function.

On the level of the Berry connection, this results in the gauge transformation that we saw in Eq. 2.8. Then, we define U(1) link variables which capture relative

[1] We will from now on call the first Chern number just *Chern number*.

phases of eigenstates on neighboring lattice sites as [33]

$$\mathcal{U}_\mu(\boldsymbol{k}) = \frac{\langle n(\boldsymbol{k})|n(\boldsymbol{k}+\boldsymbol{\mu})\rangle}{|\langle n(\boldsymbol{k})|n(\boldsymbol{k}+\boldsymbol{\mu})\rangle|} \tag{2.21}$$

where $\mu = x, y$, $\boldsymbol{\mu}$ is the unit vector in direction μ with length $2\pi/N$, and the eigenstate $|n\rangle$ is the eigenstate corresponding to the n-th band.

Next, we define a lattice field strength by taking the product of all relative phases around the boundary of a plaquette (which consists of neighboring lattice sites at each vertex) [33]

$$\tilde{\mathcal{F}}(\boldsymbol{k}) = \log\Big(\mathcal{U}_x(\boldsymbol{k})\mathcal{U}_y(\boldsymbol{k}+\boldsymbol{x})\mathcal{U}_x^{-1}(\boldsymbol{k}+\boldsymbol{y})\mathcal{U}_y^{-1}(\boldsymbol{k})\Big) \tag{2.22}$$

where we select the default branch of the logarithm as $-\pi < \tilde{\mathcal{F}}(\boldsymbol{k})/i \leq \pi$. In fact, we have $\tilde{\mathcal{F}}(\boldsymbol{k}) = \mathcal{F}(\boldsymbol{k})$ if it holds that $-\pi < \tilde{\mathcal{F}}(\boldsymbol{k})/i \leq \pi$. If $\tilde{\mathcal{F}}(\boldsymbol{k})$ is outside this range, it means that we have vortex in the plaquette [8] (which as we shall see later on relates to a singularity in the corresponding wave functiion), and we can bring $\tilde{\mathcal{F}}(\boldsymbol{k})$ back to $(-\pi, \pi]$ which means that we picked effectively up phase factor of 2π. Thus, the field strength $\tilde{\mathcal{F}}(\boldsymbol{k})$ counts the net number of vortices in the Brillouin zone and the sum

$$C = \frac{1}{2\pi}\sum_{k\in \mathrm{BZ}} \tilde{\mathcal{F}}(\boldsymbol{k}) \tag{2.23}$$

is the Chern number.

Finally, we refer to Fig. 2.1 which describes numerical method for the reconstruction and visulzation of the Berry curvature in the Brillouin zone. This method will be used several times in this PhD thesis.

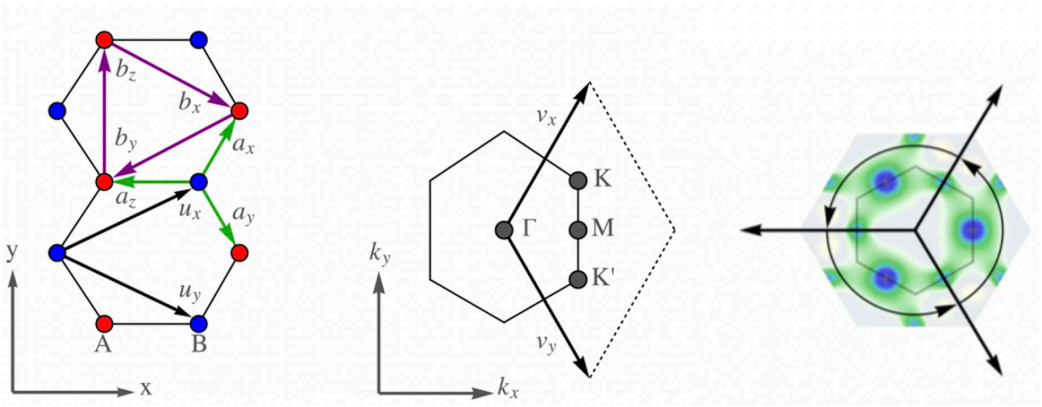

FIGURE 2.1: Graphene lattice, lattice vectors, and (next) nearest neighbor displacements. Center: Brillouin zone, reciprocal lattice vectors and high symmetry points. Right: Reconstruction of the Brillouin zone for the Berry curvature plot using the C_3 symmetry of the Haldane model, see following section. For each plot, the result of the Berry curvature is normalised to one, i.e. each data set is divided by the maximum absolute Berry curvature value contained in the data set.

2.2 Graphene

2.2.1 Hexagonal lattice structure

First, we define the lattice structure of graphene, the called the hexagonal or honeycomb lattice. The lattice vectors, see Fig. 2.1, are given by [11, 13]

$$\mathbf{u}_x = \frac{1}{2}\left(3, \sqrt{3}\right) \qquad \mathbf{u}_y = \frac{1}{2}\left(3, -\sqrt{3}\right). \qquad \mathbf{u}_z = (0, 0) \tag{2.24}$$

where we set the bond length to unity. Furthermore, we denote nearest neighbor displacements by [13]

$$\mathbf{a}_x = \frac{1}{2}\left(1, \sqrt{3}\right) \qquad \mathbf{a}_y = \frac{1}{2}\left(1, -\sqrt{3}\right) \qquad \mathbf{a}_z = \frac{1}{2}\left(-1, 0\right). \tag{2.25}$$

In momentum space, we define the reciprocal lattice vectors as [13]

$$\boldsymbol{\nu}_x = \frac{2\pi}{3}\left(1, \sqrt{3}\right) \qquad \boldsymbol{\nu}_y = \frac{2\pi}{3}\left(1, -\sqrt{3}\right) \tag{2.26}$$

which satisfy the orthogonality condition

$$\boldsymbol{u}_i \cdot \boldsymbol{v}_j = 2\pi\delta_{ij}. \tag{2.27}$$

Note that the hexagonal lattice consists of unit cells containing two sites each. In fact, the hexagonal can be seen as being made out of two interpenetrating triangular lattices [13]. One finds two distinct symmetry points $\boldsymbol{K}$ and $\boldsymbol{K}'$ at the vertices of the Brillouin zone of the reciprocal hexagonal lattice, cf. Fig. 2.1, at which most of the interesting phenomena in graphene physics occur [13]. These points are located at

$$\mathbf{K} = \frac{2\pi}{3}\left(1, \frac{1}{\sqrt{3}}\right) \qquad \mathbf{K}' = \frac{2\pi}{3}\left(1, -\frac{1}{\sqrt{3}}\right), . \tag{2.28}$$

Now, we also introduce the next nearest neighbour displacements in a basis of the $\mathbf{a}_i$, which will be helpful later on. These are then expressed as

$$\mathbf{b}_i = \mathbf{a}_j - \mathbf{a}_k, \tag{2.29}$$

where (i, j, k) is a cyclic permutation of (x, y, z). However, note that using an $\mathbf{a}_i$ basis does not yield a Hamiltonian in Bloch form. In practice, we therefore employ a basis given by the lattice vectors $\mathbf{u}_i$ (which corresponds to a gauge transforming the Hamiltonian to the new basis) and define next nearest neighbour displacements $\mathbf{b}_i$ accordingly in terms of the $\mathbf{u}_i$.

2.2.2 Graphene tight binding Hamiltonian

Next, we write down the Hamiltonian of the simplest graphene model on the honeycomb lattice including only nearest neighbor hoppings

$$\mathcal{H}_g = -\sum_{\langle i,j \rangle} t_1 c_i^\dagger c_j. \tag{2.30}$$

In momentum space, this Hamiltonian assumes the form

$$\mathcal{H}_g = \sum_{\boldsymbol{k}} \sum_{p\in\{x,y,z\}} c_{\boldsymbol{k}}^{\dagger} \begin{pmatrix} 0 & -g\left(\boldsymbol{k}\right) \\ -g^{*}\left(\boldsymbol{k}\right) & 0 \end{pmatrix} c_{\boldsymbol{k}}. \tag{2.31}$$

Here, $\boldsymbol{k}$ runs over the whole Brillouin zone, and p runs over the links $\{x, y, z\}$. Furthermore, the spinor basis consists of the two components $c_{\boldsymbol{k}}^{\dagger} = \left(c_{\boldsymbol{k}A}^{\dagger}, c_{\boldsymbol{k}B}^{\dagger}\right)$ where A and B denote the two different sites in each unit cell, cf. Fig. 2.1. Most importantly, the function g is defined as

$$g\left(\boldsymbol{k}\right) = t_1 \sum_{p\in\{x,y,z\}} \left(\cos\left(\boldsymbol{k}\cdot\boldsymbol{a}_p\right) - i\sin\left(\boldsymbol{k}\cdot\boldsymbol{a}_p\right)\right). \tag{2.32}$$

We can also choose to write the Hamiltonian Eq. 2.31 using Pauli matrices σ^p as

$$\mathcal{H}_g = \sum_{\boldsymbol{k}} c_{\boldsymbol{k}}^{\dagger} \left(\boldsymbol{d}_g \cdot \boldsymbol{\sigma}\right) c_{\boldsymbol{k}}. \tag{2.33}$$

The interpretation of this form is that the itinerating electrons interact with a the pseudo magnetic field $\boldsymbol{d}_g$ consisting of the components

$$\begin{aligned} d_g^x(\mathbf{k}) &= -t_1 \sum_p \cos(\mathbf{k}\cdot\mathbf{a}_i) \\ d_g^y(\mathbf{k}) &= -t_1 \sum_p \sin(\mathbf{k}\cdot\mathbf{a}_i) \\ d_g^z(\mathbf{k}) &= 0. \end{aligned} \tag{2.34}$$

The dispersion relation of graphene can be computed by diagonalization of the matrix in Eq. 2.31. This results in two energy bands with corresponding eigenenergies [13]

$$E_{\pm}\left(\boldsymbol{k}\right) = \pm t_1 \sqrt{3 + 2\cos\left(\sqrt{3}k_y\right) + 4\cos\left(\frac{\sqrt{3}}{2}k_y\right)\cos\left(\frac{3}{2}k_x\right)}. \tag{2.35}$$

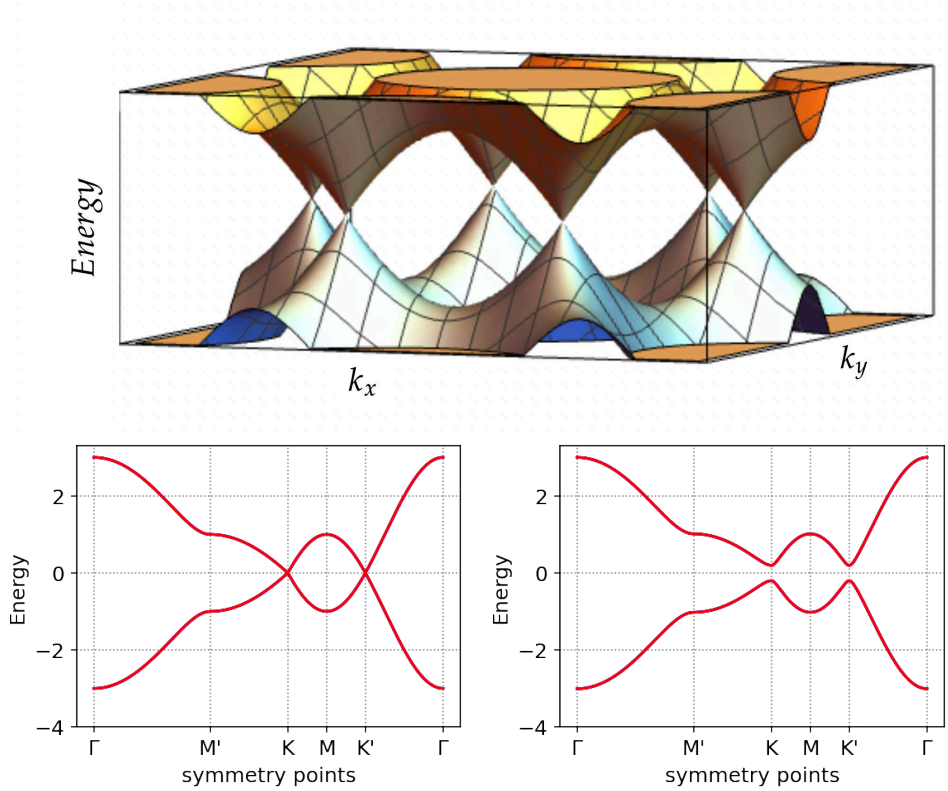

FIGURE 2.2: Top: the three dimensional band structure of Graphene in the Brillouin zone. Crossings of cone shape appear at the Dirac points - so called *Dirac cones*. Bottom left: Two dimensional band structure of graphene along high symmetry points, cf. Fig. 2.1. Bottom right: Two dimensional band structure of graphene along high symmetry points, with non-zero Semenoff mass. This breaks inversion symmetry and opens a gap at the Dirac points. Energy scales are given in terms of the nearest neighbor hopping amplitude t_1.

Fig. 2.2 shows the numeric result. As it can be seen, the upper and lower bands cross exactly six points. These are in fact the $\boldsymbol{K}$ and $\boldsymbol{K}'$ points of the Brillouin zone. These points are also called *Dirac points* - a naming that we need to motivate. To this end, we diagonalize the Hamiltonian density matrix in Eq. 2.31 around the crossings at $\boldsymbol{K}$ and $\boldsymbol{K}'$. For small deviations from the Dirac points

$\boldsymbol{q} = (q_x, q_y)$ we obtain in the two regions the approximative Hamiltonian densities

$$\mathcal{H}_{\mathbf{K}}(\mathbf{q}) = \begin{pmatrix} 0 & v_F(-iq_x + q_y) \\ v_F(iq_x + q_y) & 0 \end{pmatrix} \tag{2.36}$$

and

$$\mathcal{H}_{\mathbf{K}'}(\mathbf{q}) = \begin{pmatrix} 0 & v_F(-iq_x - q_y) \\ v_F(iq_x - q_y) & 0 \end{pmatrix}, \tag{2.37}$$

where $v_F = \frac{3}{2}t_1$ is called the Fermi velocity. These types of Hamiltonians is that of massless Dirac fermions of relativistic quantum mechanics in two spatial dimensions [34, 11, 13], where the role of the velocity of light is essentially played by v_F.

Finally, we point out that a straightforward diagonalization of the above matrices yields the eigenstates

$$\Psi^{g}_{\pm,\mathbf{K}}(\phi_{\mathbf{q}}) = \frac{1}{\sqrt{2}} \begin{pmatrix} 1 \\ \pm e^{i\phi_{\mathbf{q}}} \end{pmatrix}, \qquad \Psi^{g}_{\pm,\mathbf{K}'}(\phi_{\mathbf{q}}) = \frac{1}{\sqrt{2}} \begin{pmatrix} 1 \\ \pm e^{-i\phi_{\mathbf{q}}} \end{pmatrix}, \tag{2.38}$$

where $iq_x + q_y = q \cdot e^{i\phi_{\mathbf{q}}}$ and $q = |\mathbf{q}|$. The $\pm$ sign refers to the positive and and negative energy bands.

The fact that the above wave functions have two components can be associated with existence of the A and B sublattices in the hexagonal lattice. At the same time, the reminiscence with the form of a spin $1/2$ wave function, leads to the introduction of the term *pseudospin* for this degree of freedom.

Furthermore, the graphene Hamiltonian has another property called *chirality*. As we have seen, the wave functions Eq. 2.38 in each K point valley (i.e. the region in proximity to either the Dirac point), take different forms. The fact that each electrons in either valley have different chirality points to the fact that the

pseudospin in either valley depends on the direction of the electronic momentum. In fact, this has important implications for the Berry phases we find when encircling either Dirac point. First of all, we note that when we use Eq. 2.7 to compute Berry phase when encircling either Dirac point, we find an absolute Berry phase of π (in contrast to the winding number Eq. 2.10 which is a multiple of 2π since we considered single valued wave functions). Secondly, when considering the opposite chirality in the two valleys (which is for example reflected in the fact that ϕ_q in Eq. 2.38 comes with different signs in each valley), we find that the Berry phase in one valley is $+\pi$ while in the other valley $-\pi$. Therefore, the Dirac points in the Brillouin zone of the hexagonal lattice can be identified as topological defects. We shall see below how Haldane used the existence of this defects to engineer a topological insulator from graphene by breaking time reversal symmetry of the graphene Hamiltonian.

2.2.3 Symmetry protection of the Dirac cones

In Fig. 2.2 we observed cone shape crossings in the Brillouin zone. These *Dirac cones* are protected by symmetries that preserve the system from opening a gap.

The first of these symmetries is *time reversal* symmetry. It can easily be seen that the above derived local effective Hamiltonians Eq. 2.36 and 2.37 fulfill [11]

$$\mathcal{H}^*_{\mathbf{K}'}(\mathbf{q}) = \mathcal{H}_{\mathbf{K}}(-\mathbf{q}) \tag{2.39}$$

which agrees with the condition for spinless Bloch Hamiltonians to respect time reversal symmetry [11].

Time reversal symmetry is, however, not a sufficient condition for the existence of the gapless Dirac cones. In fact, we can introduce a mass term M on the diagonal of the matrices Eq. 2.36 and 2.37 where we give M a different sign on

each of the two sublattices, i.e. we have

$$\mathcal{H}_{\mathbf{K}}(\mathbf{q}) = \begin{pmatrix} M & v_F\left(-iq_x + q_y\right) \\ v_F\left(iq_x + q_y\right) & -M \end{pmatrix}, \tag{2.40}$$

and in the same way for $\mathcal{H}_{\mathbf{K}'}(\mathbf{q})$. The mass term M is called a staggered potential or Semenoff mass [35]. Indeed, upon introduction of the mass term M, the time reversal condition Eq. 2.39 is still fulfilled, however we open up a gap at the Dirac points, cf. Fig. 2.2.

The non-zero Semenoff mass term M manually breaks another symmetry that protects the Dirac cones - sublattice inversion symmetry. The inversion operator acting in sublattice space can be expressed as the Pauli matrix σ^x. This operator changes sublattice $A \rightarrow B$ and vice versa. Using again the matrices Eq. 2.36 and 2.37, we can easily verify that the condition [11]

$$\mathcal{H}_{\mathbf{K}'}(\mathbf{q}) = \sigma^x \mathcal{H}_{\mathbf{K}}(-\mathbf{q})\,\sigma^x \tag{2.41}$$

is fulfilled. Due to the bipartite nature of the honeycomb lattice, we noted that we have two distinct Dirac points. However, now we see that they are closely related by symmetry, as in Eq. 2.39 and 2.41.

2.3 The Haldane honeycomb model

2.3.1 Quantum Hall state in graphene without external magnetic field

The previously mentioned IQHE [6] was realized by the application of an external magnetic to a two dimensional electron gas. This system was then found to exhibit a quantized Hall conductivity σ_{xy}. In the 1980s Haldane came to the realization [14] that the source for the orbital magnetic field that generates the Hall

conductivity is not the external magnetic field itself but the time reversal symmetry breaking induced by it. Haldane started from the graphene tight binding model which we introduced in the previous section and set out to construct a model that could realize a quantized Hall conductivity *without* the necessity of an external magnetic field. This model, the *Haldane honeycomb model* realizes the quantum *anomalous* Hall effect (QAHE).

The Haldane honeycomb model is therefore the prototypical model of what we call today a *Chern insulator* [11, 36]. In fact, its name arises from the fact that its crucial defining property is the existence of a non-zero Chern number. A Chern insulator is an insulator in the bulk that exihibits, as we shall see, gapless chiral modes located at the edges. The Chern number Eq. 2.14 is therefore the characterizing invariant in this system.

Haldane pointed out in this seminal paper [14] that the model he proposed was of theoretical interest, however, it might never be realized in an experimental setting. Fortunately, this is not the case and the Haldane honeycomb model has eventually been realized [36, 11] in quantum materials [37], graphene [38], photonic systems [39, 40, 41, 42, 43, 44] and cold atoms in optical lattices [45, 46].

2.3.2 The Haldane Hamiltonian

The Haldane honeycomb model [14] consists of two parts

$$\mathcal{H}_h = -\sum_{\langle i,j\rangle} t_1 c_i^\dagger c_j - \sum_{\langle\langle i,j\rangle\rangle} t_2 e^{\pm i\Phi} c_i^\dagger c_j. \tag{2.42}$$

The first term is the nearest neighbor hopping on the honeycomb lattice with hopping amplitude t_1 that we already know from the graphene tight binding model, cf. Eq. 2.30. The second term adds complex valued next-nearest neighbor hopping on the honeycomb lattice. Refer to Fig. 2.1 and Eq. 2.29 where we defined the next-nearest neighbor displacements. Furthermore, $t_2 \exp(\pm i\Phi)$ is

the *complex* hopping amplitude, Φ is the Peierls phase which we will fix from now on to $\Phi = \pi/2$. Crucially, the $\pm$ sign refers to the hopping orientation. We choose the positive sign if we move clockwise around the hexagonal plaquette and the negative sign if we move counterclockwise around the hexagonal plaquette.

The complex hopping amplitude accomplishes the breaking of time reversal symmetry. At the same time, the different sign when moving from $A \to A$ sublattice sites or $B \to B$ sublattice sites induces an effective staggered fluxes such that the total net flux in each hexagonal plaquette is zero [31].

Similarly to Eq. 2.33 and 2.34, we can choose to write the Haldane honeycomb Hamiltonian in momentum space using a magnetic field vector $\boldsymbol{d}_h$ as

$$\mathcal{H}_h = \sum_{\boldsymbol{k}} c_{\boldsymbol{k}}^\dagger \left(\boldsymbol{d}_h \cdot \boldsymbol{\sigma} + \epsilon_h \cdot \mathcal{I} \right) c_{\boldsymbol{k}}. \tag{2.43}$$

The components of the magnetic field $\boldsymbol{d}_h$ are the same for the x and y components as for graphene, cf. Eq. 2.34, i.e. $d_h^x(\mathbf{k}) = d_g^x(\mathbf{k})$ and $d_h^y(\mathbf{k}) = d_g^y(\mathbf{k})$. On the other hand, the z component now reads

$$d_h^z(\mathbf{k}) = M - 2t_2 \sin\Phi \sum_p \sin(\mathbf{k} \cdot \mathbf{b}_i), \tag{2.44}$$

and we have furthermore a 0-component ϵ_h which is defined as

$$\epsilon_h = -2t_2 \cos\Phi \sum_p \cos(\mathbf{k} \cdot \mathbf{b}_i) \tag{2.45}$$

and $\mathcal{I}$ is the 2×2 identity matrix.

Furthermore, in the following work we will find it useful to write the Haldane honeycomb model in matrix form analogous to the graphene matrix Hamiltonian

Eq. 2.42. In this form, if we fix $\Phi = \pi/2$, we can write Eq. 2.42 as [47]

$$\mathcal{H}_h = \sum_{\boldsymbol{k}} \sum_{p\in\{x,y,z\}} c_{\boldsymbol{k}}^\dagger \begin{pmatrix} \gamma(\boldsymbol{k}) & -g(\boldsymbol{k}) \\ -g^*(\boldsymbol{k}) & -\gamma(\boldsymbol{k}) \end{pmatrix} c_{\boldsymbol{k}}. \tag{2.46}$$

Here, the function $g(\boldsymbol{k})$ is defined as in Eq. 2.32. Here, we define (for $\Phi = \pi/2$) the function $\gamma(\boldsymbol{k})$ as

$$\gamma(\boldsymbol{k}) = M - 2t_2 \sum_p \sin(\boldsymbol{k}\cdot\boldsymbol{b}_p), \tag{2.47}$$

where M is the Semenoff mass introduced in the previous section.

2.3.3 Haldane phase diagram

We remember that we had a vanishing z component in the graphene model $\boldsymbol{d}_g$, cf. Eq. 2.31 and in particular we noticed that (for Semenoff mass $M = 0$) we had gapless modes at the Dirac points. Both, the introduction of a non-vanishing Semenoff mass M and the introduction of complex next-nearest neighbor hoppings as in introduced by Haldane, add a finite z component to the model, cf. Eq. 2.44, which opens up a gap. The Semenoff mass M breaks inversion symmetry, while complex next-nearest neighbor hopping breaks time reversal symmetry - the two symmetries we found to protect the Dirac cones.

In fact, we find for the z component d_h^z for some small wave vector $\boldsymbol{q}$ close to the Dirac points that

$$d_{h,\boldsymbol{K}}^z(\mathbf{q}) = M - 3\sqrt{3}t_2\sin(\Phi) \tag{2.48}$$

$$d_{h,\boldsymbol{K}'}^z(\mathbf{q}) = M + 3\sqrt{3}t_2\sin(\Phi). \tag{2.49}$$

This result points to a crucially different behavior of the inversion symmetry breaking Semenoff mass M and the complex next-nearest neighbor hopping t_2. The Semenoff mass does not change sign when moving from $\boldsymbol{K}$ to $\boldsymbol{K}'$, while the

t_2 term does. In chapter 3.3.1, we will show in more mathematical detail that this change of sign is of deep importance. The change of sign refers in fact to a band inversion at *one* of the two Dirac points due to the t_2 term. In order to explain what this mean for the topology in the system, let us start from the pure graphene model. As we know, graphene is a Dirac semimetall with zero Chern number. However, one can still define a Berry phase [12] of $\pm\pi$ associated with local pseudo-spin effects in momentum space when linearizing the band structure around the two inequivalent Dirac points [13]. That means, when we consider the lower energy band, and we encircle the $\boldsymbol{K}$ point, we find a Berry phase of π, while we find a Berry phase of $-\pi$ for $\boldsymbol{K}'$. For the upper energy band, we find the signs to be inverted. We will highlight this fact in more detail in chapter 3.2 (refer to Fig. 3.3). In particular this means that overall, we find a net Chern number of zero since for each band the contributions from the two Dirac points sum to zero, i.e. $\pi - \pi = 0$. Crucially, the additional t_2 term in the Haldane model now induces a band inversion at one of the Dirac points. This means that the two contributions do not sum to zero but rather to $\pm 2\pi$ (positive sign for the lower band, negative sign for the upper band) resulting in a net Chern number of ± 1 in the bands.

Let us refer back to Eq. 2.48 and 2.49. We can deduce from these equations that depending on the choice of parameters M, t_2 and Φ, there are points where the gap at one of the Dirac points closes, i.e. where $d^z_{h,\boldsymbol{K}/\boldsymbol{K}'} = 0$. For the $\boldsymbol{K}$ point this happens for example for $M = 3\sqrt{3}t_2 \sin(\Phi)$. In the same way we invert the bands at one Dirac points when opening a gap when going from $t_2 = 0$ to $t_2 \neq 0$, the band closing that occurs at $|M| = 3\sqrt{3}t_2 \sin(\Phi)$ inverts the bands at one of the Dirac points and thus marks a phase transition between a topologically trivial state with zero Chern number and a topological state with Chern number ± 1. The situation where we close one of the Dirac points is shown in Fig. 2.4 (bottom right). Overall, we can deduce the phase diagram [14] in Fig. 2.3.

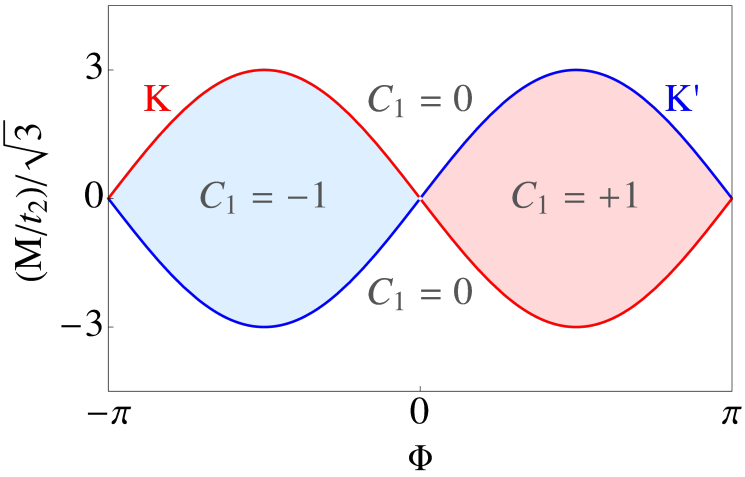

FIGURE 2.3: Phase diagram of the topological Haldane honeycomb model. Here, the Chern number C_1 refers to the lower, filled band. The red and blue borders (marked with K and K′, respectively) that separate the topological and trivial phases indicate at which of the two Dirac points the gap closes when transitioning between phases.

2.3.4 Bulk and edge band structure of the Haldane model

Lastly, we will explore the phenomenology of the Haldane honeycomb model in some more detail. Let us start with the bulk band structure.

Starting from graphene at $t_2 = 0$, setting some non zero t_2 will open a gap at the Dirac points. As we can see from Eq. 2.48 and 2.49, the gap size grows linearly in t_2 and for small t_2 the low energy physics will be located at the Dirac points (where we find smallest band gap), see Fig. 2.4. At $t_2 = \frac{1}{3\sqrt{3}}t_1$ (where $\frac{1}{3\sqrt{3}} \approx 0.19$) the bands become noticeably flat in an area spanned by the M and K points in Brillouin zone [47]. From this point onward (for further increasing t_2), the minimal gap size Δ will remain constant at $\Delta = 2t_1$. In fact, for $t_2 > \frac{1}{3\sqrt{3}}t_1$ the low energy physics and the smallest band gap is located at the M symmetry points in the Brillouin zone, see Fig. 2.4.

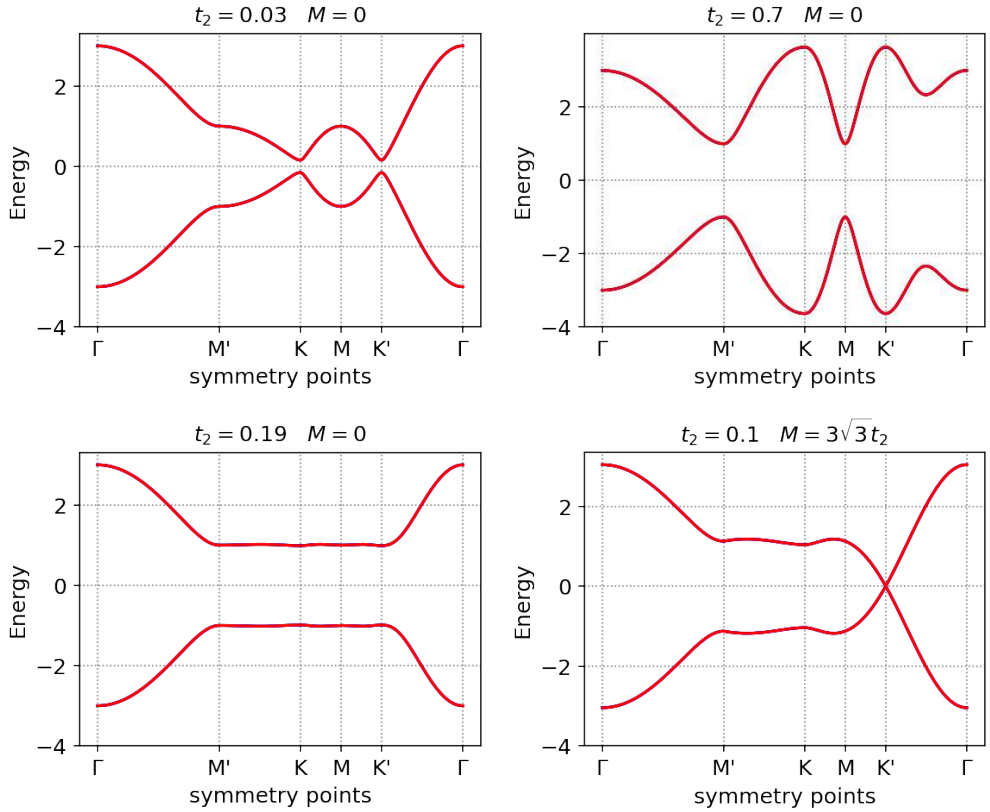

FIGURE 2.4: Haldane honeycomb model bulk band structures for different parameter configurations (where we fixed the Peierls phase to $\Phi = \pi/2$ and the energy scale is given in terms of the nearest neighbor hopping amplitude t_1). Top left: small t_2 with low energy physics located at the Dirac points. Top right: large t_2 with low energy physics located at the M points. Bottom left: flat bands for $t_2 = 0.19$. Bottom right: gap closing at one of the Dirac points for $M = 3\sqrt{3}t_2$.

It is important to notice these two parameter regimes

$$t_2 > \frac{1}{3\sqrt{3}}t_1 \qquad \text{K point physics} \tag{2.50}$$

$$t_2 < \frac{1}{3\sqrt{3}}t_1 \qquad \text{M point physics.} \tag{2.51}$$

We will see in chapter 4 that it can be helpful to restrict a model to the K point regime (small t_2) since it can be quite insightful to construct model on the basis of Dirac point properties as we saw in our introduction to graphene. Dirac point

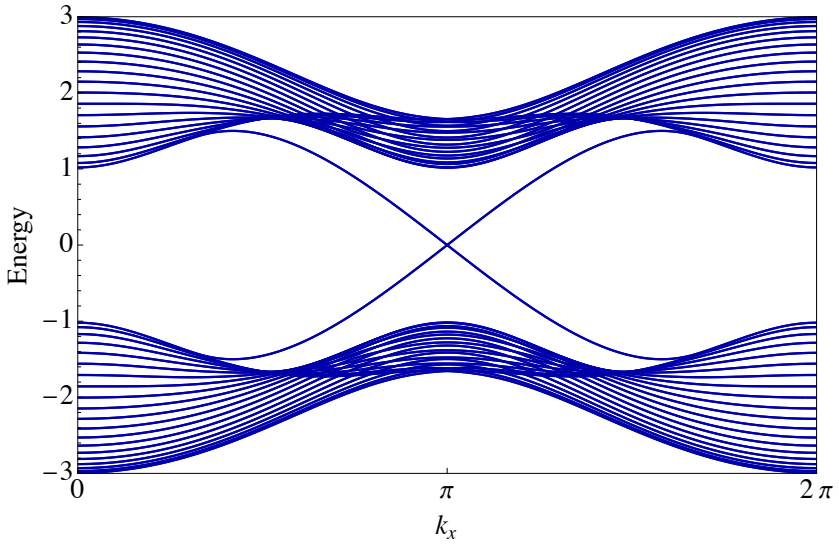

FIGURE 2.5: Edge spectrum of the Haldane honeycomb model for $t_1 = 1$, $t_2 = 1/3$, and $\Phi = \pi/2$. Bulk bands are gapped, only the chiral modes located at the two edges are gapless.

properties are the source of the topology in the Haldane, thus we should seek to exploit their rich phenomenology.

Finally, let us visually verify the presence of a non-zero Chern number in the Haldane model. The computation of bulk bands (as in Fig. 2.4) assumes translational invariance in the lattice, and thus a lattice without edges that extends infinitely. In order to verify the emergence of chiral edge modes in the Haldane honeycomb model, we need to mathematically *create* an edge. That means we intentionally break translational symmetry in one direction, say k_y [48, 11]. Since k_y is then not a good quantum number any more, we need to translate the k_y component back to real space such that we end up with a Hamiltonian in a mixed form (real and momentum space) such that we can visualize modes that are located in the bulk as well as at the edges of the system. Fig. 5.1 shows the edge spectrum of the Haldane honeycomb model. Bulk bands are gapped and only two chiral edge modes cross the Fermi level corresponding to the lower and upper energy bands which carry Chern number $+1$ and -1.

2.3.5 Probing Chern numbers via the circular dichroism of light

In this last section on the topologic Haldane model, we describe an intriguing experimental protocol to probe the topology of a Chern insulator.

The circular dichroism of light has been suggested as a measure of the Chern number [49, 50]. Shining light on a Chern insulator induces a population of the states in the upper band, above the band gap. The associated depletion rates and photocurrents [51] depend on the orientation of the circular drive. The Chern number is encoded in the difference of rates with opposite orientation.

The following discussion will be of us for us in later chapters especially with regard to the application to the topological Haldane. However, the results in Ref. [49] where derived under the assumption of any two-dimensional, non-interacting spinless gas in a generic lattice, initially filled lower band, gapped bulk bands and broken time reversal symmetry such that the topology in the system is describe by a Chern number. Let us assume this two band system is described by a time-independent Hamiltonian $\mathcal{H}_0$ and subjected to a time-periodic ciruclar drive such that the total time-dependent Hamiltonian reads [49]

$$\mathcal{H}_{\pm}(t) = \mathcal{H}_0 + 2E\left(\cos(\omega t)\hat{x} \pm \sin(\omega t)\hat{y}\right) \tag{2.52}$$

where E is a constant electric field, $\pm$ refers to the orientation of the drive, $\hat{x}$ and $\hat{y}$ are position operators, and ω is the frequency of the drive. The second part of Eq. 2.52 can be attributed to a scalar potential $\mathcal{V}_{\pm}$

$$\mathcal{V}_{\pm}(x, y) = 2E(\cos(\omega t)x \pm \sin(\omega t)y) \tag{2.53}$$

which is defined such that $\boldsymbol{\mathcal{E}}_\pm = -\nabla\mathcal{V}_\pm$. Here, $\boldsymbol{\mathcal{E}}_\pm$ is the circularly polarized electric field that takes the form

$$\boldsymbol{\mathcal{E}}_\pm = 2E(\cos(\omega t)\boldsymbol{e}_x \pm \sin(\omega t)\boldsymbol{e}_y) \tag{2.54}$$

This *heating* of the system through irradiation with circularly polarized light leads to a promotion of a total number of $N_\pm$ particles from the lower to the upper band. In other words, the lower bands is depleted at a rate $\Gamma_\pm$ where [49]

$$\delta N_\pm(t) \approx -\Gamma_\pm t. \tag{2.55}$$

We can then use *Fermi's golden rule* [49, 52] which reads for a two band model with bands l and u

$$\Gamma_\pm(\omega) = \frac{2\pi}{\hbar}E^2|\langle l|\hat{x} \pm i\hat{y}|u\rangle|^2\delta^t(\epsilon_u - \epsilon_l - \hbar\omega) \tag{2.56}$$

where E is the strength of the drive or the electric field in the original basis, $|u\rangle$ and $|l\rangle$ are the eigenstates corresponding to the lower and upper bands, $\epsilon_{l,u}$ their eigenenergies, and the $\pm$ selects the polarization orientation.

The electric field introduced in Eq. 2.54 can be related to a dependent vector potential $\boldsymbol{\mathcal{A}}_\pm$ via $\boldsymbol{\mathcal{E}}_\pm = -\partial_t\boldsymbol{\mathcal{A}}_\pm$ such that the vector potential takes the form

$$\boldsymbol{\mathcal{A}}_\pm = -\frac{2E}{\omega}(\sin(\omega t)\boldsymbol{e}_x \mp \cos(\omega t)\boldsymbol{e}_y). \tag{2.57}$$

Minimal coupling of the vector potential with the current operator $-\partial_k\mathcal{H}_0$ gives a time-dependent Hamiltonian which now reads in momentum space

$$\mathcal{H}_\pm(t) \approx \mathcal{H}_0(\boldsymbol{k}) + \frac{2E}{\hbar\omega}\left(\sin(\omega t)\frac{\partial\mathcal{H}_0(\boldsymbol{k})}{\partial k_x} \mp \cos(\omega t)\frac{\partial\mathcal{H}_0(\boldsymbol{k})}{\partial k_y}\right). \tag{2.58}$$

In Ref. [49], the authors obtained this result by performing a unitary transformation on the Hamiltonian in Eq. 2.52 as $\mathcal{H}_\pm \to \mathcal{R}_\pm \mathcal{H}_\pm \mathcal{R}_\pm^{-1}$ generated by the operator

$$\mathcal{R}_\pm = \exp\left(i\frac{2E}{\hbar\omega} \left(\sin(\omega t)\hat{x} \mp \cos(\omega t)\hat{y}\right)\right). \tag{2.59}$$

In Eq. 2.58, higher order terms in E have been omitted. Then, the depletion rates can be expressed as [49]

$$\Gamma^\pm_{l\to u}\left(\omega_{\boldsymbol{k}}, \boldsymbol{k}\right) = \frac{2\pi}{\hbar}\left(\frac{E}{\hbar\omega}\right)^2 \left|\mathcal{A}^\pm_{l\to u}\right|^2 \delta\left(\epsilon^{\boldsymbol{k}}_u - \epsilon^{\boldsymbol{k}}_l - \hbar\omega\right) \tag{2.60}$$

where $\epsilon^{\boldsymbol{k}}_{l,u}$ are the eigenenergies of the lower and upper bands, and

$$\Gamma^\pm_{l\to u}\left(\omega_{\boldsymbol{k}}\right) = \sum_{\boldsymbol{k}\in \mathrm{BZ}} \Gamma^\pm_{l\to u}\left(\omega_{\boldsymbol{k}}, \boldsymbol{k}\right). \tag{2.61}$$

Here, the transition amplitude is given by

$$\mathcal{A}^\pm_{l\to u} = \langle u_{\boldsymbol{k}}| \frac{1}{i}\frac{\partial \mathcal{H}_0}{\partial k_x} \mp \frac{\partial \mathcal{H}_0}{\partial k_y} |l_{\boldsymbol{k}}\rangle \tag{2.62}$$

We will use these equations for the depletion rates in an adapted form later on in order to find a framework to describe the topology in the Haldane honeycomb model in the presence of interactions.

In order to relate the depletion rates to the Chern number of the system, we need to integrate the depletion rates over all frequencies ω (such that ω is larger than $\Delta_{gap}/\hbar$ where Δ_{gap} is the band gap). This calculation yields the integrated rates $\Gamma^{int}_\pm$. The idea is now that depending on the polarization direction of the light, the integrated difference will *not* give the same result. The difference can be associated to the chiral nature of the system. Hence, the integrated difference $\Delta\Gamma^{int} = \Gamma^{int}_+ - \Gamma^{int}_-$ should encode the Hall conductivity and therefore should be

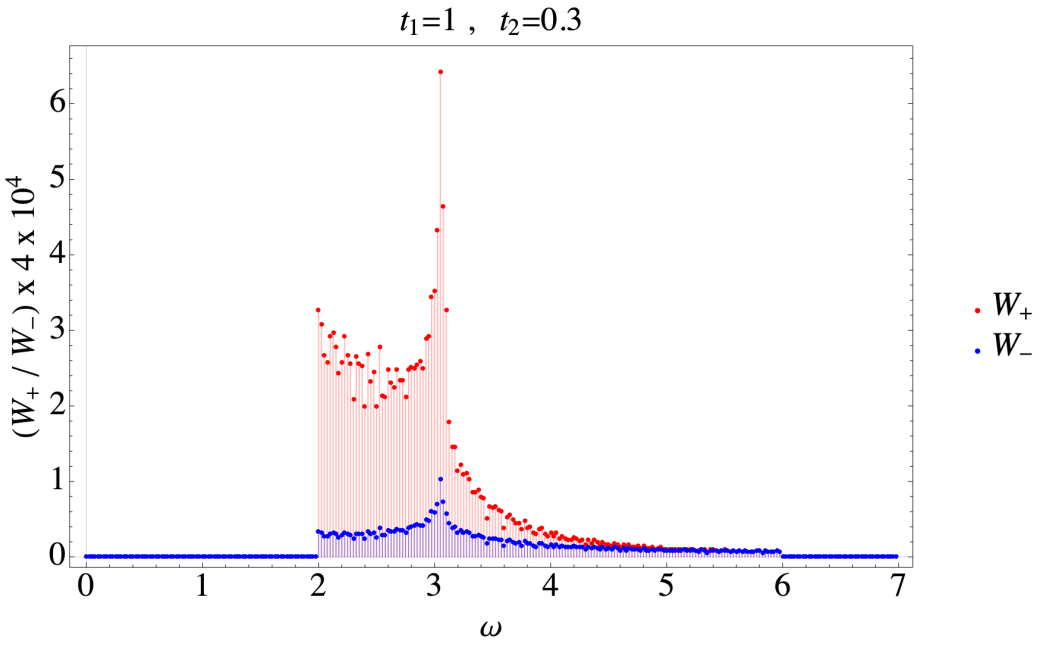

FIGURE 2.6: Numeric application of the dichroism of light to the Haldane honeycomb model on $N_{\text{size}} \times N_{\text{size}}$ lattice, where $N_{\text{size}} = 200$.

quantized. In fact, one finds that [49]

$$\Delta\Gamma^{int} = 4\pi \frac{E^2}{\hbar^2} \text{Im} \left(\sum_{\boldsymbol{k}} \frac{\langle l|\partial_{k_x}\mathcal{H}_0|u\rangle\langle u|\partial_{k_y}\mathcal{H}_0|l\rangle}{(\epsilon_u - \epsilon_l)^2} \right) \tag{2.63}$$

which resembles the transverse conductivity σ_{xy} of the quantum Hall system when expressed using the Kubo formula [32, 8].

Finally, a numeric example for the application of the dichroism of light to the Haldane honeycomb model is presented in Fig. 2.6. We consider a $N_{\text{size}} \times N_{\text{size}}$ lattice, where $N_{\text{size}} = 200$. Then, we compute the distribution of the matrix elements [49]

$$W_\pm = \frac{2\pi}{\hbar} \left(\frac{E}{\hbar\omega} \right)^2 |\mathcal{A}^\pm_{l\to u}|^2 \tag{2.64}$$

in dependence on the transition frequency ω.

In particular, the figure shows $W_\pm$ as an averaged number per pre-defined frequency interval of width $\Delta_\omega = 0.025/\hbar$. Integrating the two curves numerically

and computing the difference between the red and the blue curve, yields a Chern number

$$\frac{\Delta_\omega}{2}\frac{\hbar^2}{E^2(2\pi N_{\text{size}})^2}(\Gamma_+^{int}-\Gamma_-^{int})=1, \tag{2.65}$$

where $\Gamma_\pm^{int}$ is computed in each frequency interval as the average number $W_\pm$ times the corresponding density of states [49]. The density of states is computed in each interval as $\rho(\omega) = N_{\text{trans}}/\hbar\Delta_\omega$ where N_{trans} is the number of counted transitions within the frequency interval that belongs to ω.

Chapter 3

Topological proximity effects in the Haldane-graphene model

In this chapter, we study the Haldane honeycomb model which we introduced in the theory section, interfaced with a two-dimensional layer of graphene. It is our goal to reveal a proximity effect between a topological band (Chern) insulator (the Haldane honeycomb model) and spin-polarized Dirac particles of the graphene layer.

Previously, proximity effects have been studied [53, 54] in classical systems where a local order parameter (e.g. capturing superconductivity) penetrates into a coupled material (e.g. a metallic system). More recently, *topological* proximity effects have been proposed [55, 56, 57]. In this case, non-trivial topology (in the sense of a non-zero Chern number) is induced by means of proximity into the bulk of a topologically trivial system.

In Ref. [55], a metallic ultrathin film and a three-dimensional topological insulator were experimentally coupled. To this end, one bilayer of bismuth metal was grown on the three-dimensional topological insulator material $TlBiSe_2$. The authors then used spin- and angle-resolved photoemission spectroscopy, to find evidence that the topological Dirac-cone state migrates from the surface of $TlBiSe_2$ to the attached one-bilayer bismuth.

The first theoretical study on the subject was done in Ref. [56]. In stark contrast to Ref. [55], Ref. [56] considers two coupled systems of the same dimension. Therefore, in this case we speak of a *bulk* topological proximity effect. The authors study a generic Chern insulator coupled to a topologically trivial system. They show that by proximity a Chern number of e.g. +1 then induces an *inverse* topological number -1 into the bulk of the coupled system.

In this chapter, we study the proximity effect when tunnel coupling a Haldane model with a layer of graphene [58, 13]. We assume spinless particles in both layers and the tunnel process couples the same sublattice in the two layers. As we shall see, particle-hole processes at the interface open a gap as a result of pseudospin effects, inducing an inverse topological order in the graphene system when both layers are half-filled. While this is to be expected with Ref. [56] in mind, we will go into a detailed description of the mechanisms at play.

In fact, the topological Chern insulator induces a gap and an opposite Chern number on the Dirac particles at half-filling resulting in a sign flip of the Berry curvature at one Dirac point. We study different aspects of the bulk-edge correspondence and present protocols to observe the evolution of the Berry curvature as well as two counter-propagating (protected) edge modes with different velocities. In the strong-coupling limit, the energy spectrum shows flat bands. Therefore we build a perturbation theory and address further the bulk-edge correspondence. We also show the occurrence of a topological insulating phase with Chern number one when only the lowest band is filled. Finally, we generalize the effect to Haldane bilayer systems with asymmetric Semenoff masses.

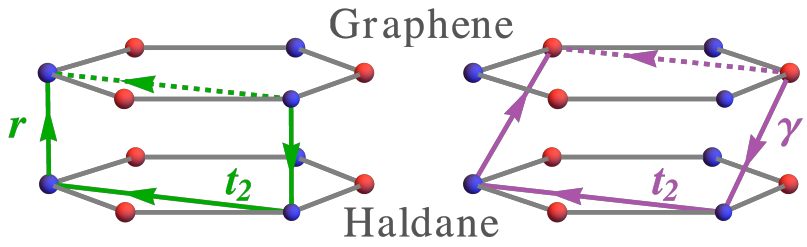

FIGURE 3.1: Schematic of the system and of the coupling parameters between the two systems. Left: Interlayer hopping between the same sublattice sites with hopping amplitude r. Right: Interlayer hopping between neighboring sublattice sites with hopping amplitude γ.

3.1 The Haldane-graphene model

We consider the Hamiltonian

$$\mathcal{H} = \mathcal{H}_g + \mathcal{H}_h + \mathcal{H}_r, \tag{3.1}$$

where $\mathcal{H}_g$ describes a graphene layer, $\mathcal{H}_h$ the topological Haldane model, and $\mathcal{H}_r$ the tunnel coupling between the layers with amplitude r. We emphasize here that we consider no displacement in the stack of the two layers. That means, the interlayer hopping that we consider is only of the type as in Fig. 3.1 (left).

We use the definitions where t_1 means nearest neighbor hopping element on the honeycomb lattice, t_2 next-nearest neighbor tunneling element with the associated phases $\pm\Phi$ for sublattices A and B as defined in the theory section 2.

In momentum space, the Hamiltonian takes the form

$$\mathcal{H} = \int \frac{\mathrm{d}\mathbf{k}}{(2\pi^2)} \mathcal{H}(\mathbf{k}), \tag{3.2}$$

where

$$\mathcal{H}(\mathbf{k}) = \begin{pmatrix} \mathbf{d}_g \cdot \boldsymbol{\sigma} & r \cdot \mathcal{I} \\ r \cdot \mathcal{I} & \mathbf{d}_h \cdot \boldsymbol{\sigma} + \epsilon_h \cdot \mathcal{I} \end{pmatrix} \tag{3.3}$$

with the pseudo-spin Pauli matrices $\boldsymbol{\sigma}$ acting in the Hilbert space of sublattice A and sublattice B of each layer g and h, respectively [34].

In order to make an analogy with two $1/2$ spins in $\mathbf{k}$-space, one could also choose to introduce two different sets of Pauli matrices $\boldsymbol{\sigma}_1$ and $\boldsymbol{\sigma}_2$; the results derived below can be simplified in notations through the introduction of one set of Pauli matrices.

In Eq. 3.3, we chose to write the previously introduced Haldane honeycomb and graphene models using magnetic fields $d^{h,g}_{x,y,z}$. These fields were introduced in Eq. 2.33 and 2.43.

We assume that the nearest-neighbor tunneling amplitudes are identical in both layers (for the simplicity of notations but without loss of generality). Therefore, we have

$$d^g_x(\mathbf{k}) = d^h_x(\mathbf{k}) \tag{3.4}$$

$$d^g_y(\mathbf{k}) = d^h_y(\mathbf{k}) \tag{3.5}$$

Initially, for graphene (when $r = 0$) the magnetic field in $\mathbf{k}$-space resides in the equatorial plane $d^g_z(\mathbf{k}) = 0$, i.e. graphene has a zero Chern number. In the numerical calculations below, we fix the phase $\Phi = \pi/2$.

3.2 Proximity effect in the Haldane-graphene model

Mapping the first Brillouin zone on a torus onto the sphere S^2, the Haldane model at $r = 0$ is characterized by the normalized magnetic field

$$d^* = (\sin\theta(\mathbf{k})\cos\phi(\mathbf{k}), \sin\theta(\mathbf{k})\sin\phi(\mathbf{k}), \cos\theta(\mathbf{k})) \tag{3.6}$$

such that the Chern number associated with the two bands of the topological Haldane insulator can be defined as

$$C^h_\pm = \frac{1}{2\pi}\int_{S^2}\mathcal{F}_\pm = \mp\frac{1}{4\pi}\int_{S^2} d\Omega = \mp 1, \tag{3.7}$$

with the relation between the Berry curvature and the solid angle on the sphere S^2

$$\mathcal{F}_\pm = \mp\sin\theta d\theta d\phi = \mp\frac{d\Omega}{2}. \tag{3.8}$$

In Fig. 3.2 top left, we show the Berry curvature associated with the lowest energy band of the Haldane model, corresponding to the Chern number $C^h_- = C_1 = +1$. The Chern number of such spin-1/2 models on the sphere S^2 has been measured in circuit Quantum electrodynamics by applying a one-dimensional path on the Bloch sphere going from north to south poles [59, 60, 61].

The Berry curvature of the Haldane model has also been reconstructed in cold atoms [46] through momentum space density which is obtained from time of flight images of

$$n(\mathbf{k}) = f(\mathbf{k})[1 - \sin\theta(\mathbf{k})\cos\phi(\mathbf{k})], \tag{3.9}$$

where $f(\mathbf{k})$ corresponds to the broad envelope associated with the momentum distribution of the Wannier function [62]. In order to measure accurately the two angles, one can create a chemical potential offset between the two sub-lattices

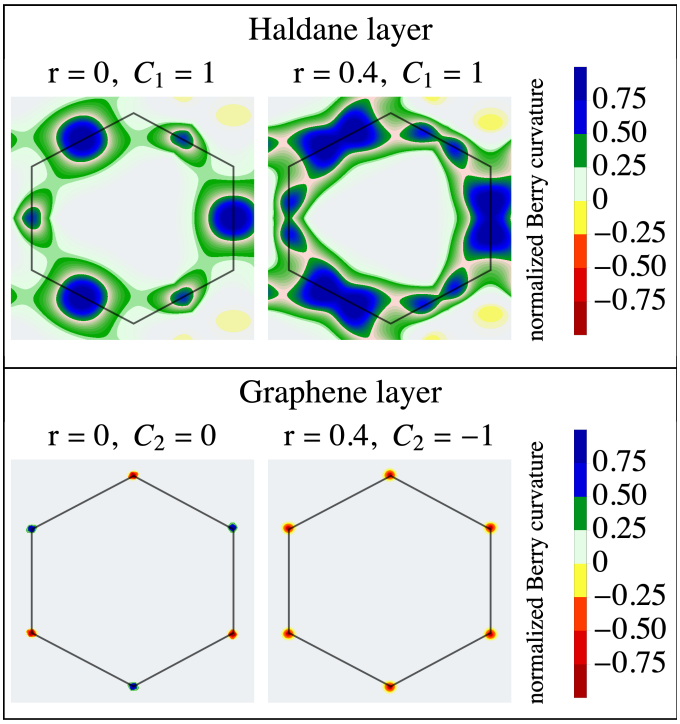

FIGURE 3.2: Berry curvature in the Brillouin zone for the Haldane and graphene layers at $r = 0$ and small r, showing the Berry phase jump effect. Here, we choose the parameters $t_1 = 1$ and $t_2 = 1/3$ and the Berry curvatures and Chern numbers were calculated using the numeric methods outlined in chapter 2.1.3.

Δ_{AB}, which then acts in the quasi-momentum representation as a rotation (in momentum space), such that

$$\phi(\mathbf{k}) \to \phi(\mathbf{k}) + \Delta_{AB} t/\hbar \tag{3.10}$$

where $\hbar = h/(2\pi)$ is the (reduced) Planck constant [62, 46]. The topology of the Bloch bands can also be accessed through Wilson line measurements [63] and coupling with circularly polarized light [38, 50].

The Chern number of the graphene system is equal to $C_{\pm}^{g} = C_2 = 0$ in the absence of coupling with the topological layer, i.e. $r = 0$. One can still define a Berry phase [12] $\pm\pi$ associated with local pseudo-spin effects in $\mathbf{k}$-space when linearizing the band structure around the two inequivalent Dirac points [13], see

Fig. 3.2 (bottom left).

Fig. 3.2 shows that when we start with a Haldane and a graphene layer without coupling (the two plots on the left), and then turn on the interlayer coupling $r > 0$, we induce an inverse Chern number -1 in the graphene layer. In the graphene layer, the Berry curvature flips at *one* of the two Dirac points - an effect which we will explore in more mathematical detail shortly. On the other hand, the Berry curvature in the Haldane layer does not change much qualitatively, and the layer retains its Chern number $+1$.

Now, we wish to understand in some more detail how an effective d_z^g magnetic field component can be induced in the graphene layer through the presence of the d_z^h term in the Haldane system. One way [25] is to build a path integral approach in the small $r \ll (t_1, t_2)$ limit integrating out degrees of freedom of the Haldane model. Assuming that the r tunneling term couples mostly the same sublattice of the different layers then the partition function of the graphene layer becomes [25]

$$\begin{aligned} Z_g &= \int \mathrm{D}\Psi_g(\mathbf{k})\mathrm{D}\bar{\Psi}_g(\mathbf{k}) \exp -\Big(\int_0^\beta d\tau \int \frac{d^2k}{2\pi^2} \bar{\Psi}_g(\mathbf{k}) \big[\partial_\tau \\ &+ \mathbf{d}_g(\mathbf{k})\sigma - \frac{r^2}{|\mathbf{d}_h(\mathbf{k})|^2}(1 - e^{-\epsilon\tau})\mathbf{d}_h(\mathbf{k})\sigma\big] (\Psi_g(\mathbf{k}))^T\Big), \end{aligned} \tag{3.11}$$

with $\Psi_g(\mathbf{k}) = (c_{gA}(\mathbf{k}), c_{gB}(\mathbf{k}))$ describing an electron annihilation operator in the graphene layer, at sublattice A and B respectively, and ϵ an energy scale close to t_2.

However, it might seem more insightful to understand the procedure in an intuitive manner from geometric considerations. We refer back to Fig. 3.1. Consider a particle that starts from the graphene layer in sublattice A, then takes the same sublattice interlayer hopping r to the Haldane layer, and after the action of the next-nearest neighbor tunneling term t_2 picking up a phase Φ, the particle goes back to the graphene layer thereby producing an effective hopping t_{eff} term

in the graphene layer proportional to

$$t_{eff} \propto -\frac{|r|^2}{|d_z^h|^2} d_z^h \sigma^z \tag{3.12}$$

The perturbation theory produces an additional minus sign to second-order in perturbation theory, and should also reveal that for the B sublattice the perturbation theory gives an opposite sign because of the nature of the Haldane t_2 term in the Haldane layer.

Finally, we check that the proximity effect remains stable as long as $r \neq 0$ when introducing a more general coupling between layers, as illustrated in Fig. 3.1 (right) through the γ term, which then allows for a coupling between different sub lattices in the two layers. The main reason is that $\sum_p \boldsymbol{a}_p = 0$, therefore when coupling a site A in the graphene layer with three sites B in the Haldane layer gives a (much) smaller contribution.

3.3 Mathematical description of the Berry phase shift

3.3.1 Singularities in the eigenstates of the Haldane-graphene model

In order to study the Berry phase shift of 2π that occurs in this scenario at one Dirac point, we investigate the low energy version of the effective graphene Hamiltonian in more detail. To this end, we first expand the term

$$d_z^h(\mathbf{k}) = -2t_2 \sin(\Phi) \sum_j \sin\left(\mathbf{k} \cdot \mathbf{b}_j\right) \tag{3.13}$$

around the Dirac points $\mathbf{K}$ and $\mathbf{K}'$ to first order for small wave vectors $\mathbf{q} = \left(q_x, q_y\right)$. We obtain

$$d_z^h(\pm\mathbf{K} + \mathbf{q}) \approx \pm 3\sqrt{3} t_2 \sin(\Phi), \tag{3.14}$$

where the positive sign corresponds to **K** and the negative sign to **K′**. Having Eq. 3.12 in mind, we define the effective mass term induced in the graphene layer

$$\pm m \equiv \pm r^2\sqrt{3}/(9\sin\Phi t_2) \tag{3.15}$$

which has different signs at the two Dirac points.

Expanding the off-diagonal terms $d_x^g(\mathbf{k})$ and $d_y^g(\mathbf{k})$ around **K** and **K′** respectively yields the corresponding low energy Hamiltonians [13]

$$\mathcal{H}_{\mathbf{K}}(\mathbf{q}) = \begin{pmatrix} m & v_F(-iq_x + q_y) \\ v_F(iq_x + q_y) & -m \end{pmatrix} \tag{3.16}$$

and

$$\mathcal{H}_{\mathbf{K}'}(\mathbf{q}) = \begin{pmatrix} -m & v_F(-iq_x - q_y) \\ v_F(iq_x - q_y) & m \end{pmatrix}, \tag{3.17}$$

with $v_F = 3t_1/2$ the Fermi velocity. Remember that in the case of pure graphene ($m = 0$) diagonalization results the normalized eigenstates

$$\Psi^g_{\pm,\mathbf{K}}(\phi_{\mathbf{q}}) = \frac{1}{\sqrt{2}}\begin{pmatrix} 1 \\ \pm e^{i\phi_{\mathbf{q}}} \end{pmatrix}, \qquad \Psi^g_{\pm,\mathbf{K}'}(\phi_{\mathbf{q}}) = \frac{1}{\sqrt{2}}\begin{pmatrix} 1 \\ \pm e^{-i\phi_{\mathbf{q}}} \end{pmatrix}, \tag{3.18}$$

where $iq_x + q_y = q \cdot e^{i\phi_{\mathbf{q}}}$ and $q = |\mathbf{q}|$. Note that $\phi_{\mathbf{q}} \to -\phi_{\mathbf{q}}$ relates the Dirac points **K** and **K′** for the same energy band (denoted $+$ or $-$) as

$$\Psi^g_{\pm,\mathbf{K}}(\phi_{\mathbf{q}}) = \Psi^g_{\pm,\mathbf{K}'}(-\phi_{\mathbf{q}}). \tag{3.19}$$

A straightforward diagonlization of the matrices Eq. 3.16 and 3.17 with $m \neq 0$ yields the normalized eigenstates

$$\tilde{\Psi}_{\pm,\mathbf{K}}\left(\phi_{\mathbf{q}}\right) = \frac{1}{\sqrt{v_F^2 q^2 + \left(E_\pm\left(\mathbf{q}\right) - m\right)^2}} \begin{pmatrix} v_F q \\ e^{i\phi_{\mathbf{q}}}\left(E_\pm\left(\mathbf{q}\right) - m\right) \end{pmatrix} \tag{3.20}$$

$$\tilde{\Psi}_{\pm,\mathbf{K}'}\left(\phi_{\mathbf{q}}\right) = \frac{1}{\sqrt{v_F^2 q^2 + \left(E_\pm\left(\mathbf{q}\right) + m\right)^2}} \begin{pmatrix} v_F q \\ -e^{-i\phi_{\mathbf{q}}}\left(E_\pm\left(\mathbf{q}\right) + m\right) \end{pmatrix} \tag{3.21}$$

where the corresponding energy eigenvalues are

$$E_\pm\left(\mathbf{q}\right) = \pm\sqrt{v_F^2 q^2 + m^2}. \tag{3.22}$$

The wavefunctions $\tilde{\Psi}_{-,\mathbf{K}}$ and $\tilde{\Psi}_{+,\mathbf{K}'}$ are well defined in the limit $\mathbf{q} \to 0$. Crucially however, $\tilde{\Psi}_{+,\mathbf{K}}$ and $\tilde{\Psi}_{-,\mathbf{K}'}$ become singular as $E_\pm(q) \xrightarrow{\mathbf{q}\to 0} \pm m$. Hence, the wavefunction $\tilde{\Psi}_{+,\cdot}$ has a singularity in $\mathbf{K}$ and the wavefunction $\tilde{\Psi}_{-,\cdot}$ has a singularity in $\mathbf{K}'$. The emergence of these singularities in the wavefunctions signals that the coupling to the Haldane layer induced some non-trivial topology in the graphene layer. Non-trivial topology arises when no global phase convention can be determined in the Brillouin zone causing the wavefunction to develop singularities [8]. However, the singularities can be avoided.

3.3.2 Lifting the singularities

First, note that the wave functions Eq. 3.20 and 3.21 fulfill the following identities

$$\tilde{\Psi}_{\pm,\mathbf{K}}\left(\phi_{\mathbf{q}}\right) = \tilde{\Psi}_{\mp,\mathbf{K}'}\left(-\phi_{\mathbf{q}}\right). \tag{3.23}$$

Hence, contrary to Eq. 3.19 for pure graphene, substituting $\phi_{\mathbf{q}} \to -\phi_{\mathbf{q}}$ relates the wavefunction of the positive (negative) energy band at $\mathbf{K}$ with the wavefunction of the negative (positive) energy band at $\mathbf{K}'$. In line with this, we can conclude

that in the pure graphene limit $m \to 0$ we regain:

$$\tilde{\Psi}_{\pm,\mathbf{K}}\left(\phi_{\mathbf{q}}\right) \xrightarrow{m\to 0} \Psi^{g}_{\pm,\mathbf{K}}\left(\phi_{\mathbf{q}}\right), \qquad \tilde{\Psi}_{\pm,\mathbf{K}'}\left(\phi_{\mathbf{q}}\right) \xrightarrow{m\to 0} \Psi^{g}_{\mp,\mathbf{K}'}\left(\phi_{\mathbf{q}}\right). \tag{3.24}$$

We now follow the method outlined in [8] and divide the Brillouin zone into two sectors $\mathcal{S}$ and $\mathcal{S}'$, where sector $\mathcal{S}$ contains $\mathbf{K}$ and sector $\mathcal{S}'$ contains $\mathbf{K}'$. We focus on the negative energy band. $\tilde{\Psi}_{-,\cdot}$ is well defined in $\mathcal{S}$, but becomes singular in $\mathcal{S}'$. As $\tilde{\Psi}_{-,\mathbf{K}}\left(\phi_{\mathbf{q}}\right) = \tilde{\Psi}_{+,\mathbf{K}'}\left(-\phi_{\mathbf{q}}\right)$ we can identify $\tilde{\Psi}_{+,\mathbf{K}'}\left(-\phi_{\mathbf{q}}\right)$ as a well defined wavefunction in $\mathcal{S}'$ of the negative energy band. This indicates that for $\mathbf{K}'$ the positive and negative energy bands exchanged their nature upon coupling the graphene and Haldane layers. In fact, it is suggestive to redefine the wavefunctions as follows where the new wavefunction $\Psi_{\pm,\cdot}$ is valid in each respective sector and energy band

$$\begin{aligned}
\Psi_{+,\mathbf{K}}\left(\phi_{\mathbf{q}}\right) &\equiv \tilde{\Psi}_{-,\mathbf{K}}\left(-\phi_{\mathbf{q}}\right), & \Psi_{+,\mathbf{K}'}\left(\phi_{\mathbf{q}}\right) &\equiv \tilde{\Psi}_{+,\mathbf{K}'}\left(\phi_{\mathbf{q}}\right), \\
\Psi_{-,\mathbf{K}}\left(\phi_{\mathbf{q}}\right) &\equiv \tilde{\Psi}_{-,\mathbf{K}}\left(\phi_{\mathbf{q}}\right), & \Psi_{-,\mathbf{K}'}\left(\phi_{\mathbf{q}}\right) &\equiv \tilde{\Psi}_{+,\mathbf{K}'}\left(-\phi_{\mathbf{q}}\right).
\end{aligned}$$

Writing these wavefunctions explicitly yields

$$\Psi_{\pm,\mathbf{K}/\mathbf{K}'}\left(\phi_{\mathbf{q}}\right) = \frac{1}{\sqrt{v_F^2 q^2 + \left(E_{\pm}\left(\mathbf{q}\right) \pm m\right)^2}} \begin{pmatrix} v_F q \\ \mp e^{\mp i\phi_{\mathbf{q}}}\left(E_{\pm}\left(\mathbf{q}\right) \pm m\right) \end{pmatrix}. \tag{3.25}$$

This "patching" of wavefunctions in sectors is allowed as long as the wavefunctions are connected by a smooth gauge transformation at the boundary between the sectors [8]. Note that $\Psi_{\pm,\cdot}$ is of the same form in $\mathcal{S}$ and $\mathcal{S}'$. Therefore, the gauge transition function between $\mathcal{S}$ and $\mathcal{S}'$ is the identity. This means that $\mathbf{K}$ and $\mathbf{K}'$ have the same Berry phase

$$\gamma_K = \gamma_{K'} = -\frac{1}{2}\oint \nabla\phi(\mathbf{k}) \cdot d\mathbf{k} = -\pi. \tag{3.26}$$

The integration follows a closed path around a Dirac point. We numerically check [33] that a $-\pi$ Berry phase occurs at both Dirac points of graphene, Fig. 3.2. This is reminiscent of the Haldane model when $t_2 \ll t_1$, thus the behavior in the graphene layer is similar to that of an Haldane model *but* only close to the Dirac points. We also check that for the upper band of graphene

$$C_+^g = +1 = -C_+^h \tag{3.27}$$

or in other words

$$\gamma_K = \gamma_{K'} = \pi. \tag{3.28}$$

This is equivalent to changing $m \to -m$ at a Dirac point or $d_z^h \to -d_z^h$.

This effective model could be perhaps realized in a bilayer graphene by applying circularly polarized light, then opening a Haldane gap in one layer [38]. If this gap is larger than the tunnel coupling, then one could rewrite the effective tunnel coupling at the Dirac points justifying this low-energy model. Below, we will address a generalized bilayer Haldane model which can be realized in cold atoms.

The Berry phases could be directly measured as demonstrated in Refs. [46, 63]. Information on Berry phases could also be reconstructed from quantum Hall conductivity [32, 64] quantum circular dichroism by shining light [50], scanning probe [65, 66] and Klein paradox [67, 68] measurements.

Note that this analysis holds for small t_2 (in comparison to t_1) when the low energy physics of the Haldane model are centred around the Dirac points, cf. Fig. 2.4. In the Haldane layer with $t_2 \sim t_1$, the pseudo-spin $1/2$ is polarized close to the Dirac point, and the structure of the Berry curvature is strongly modified: its dominant contribution occurs close to the highly-symmetric M points now, cf. Fig 2.4. Futhermore, note that Berry curvatures in the Haldane layer remain almost unchanged from $r = 0$ to $r = 0.4$, see Fig. 3.2.

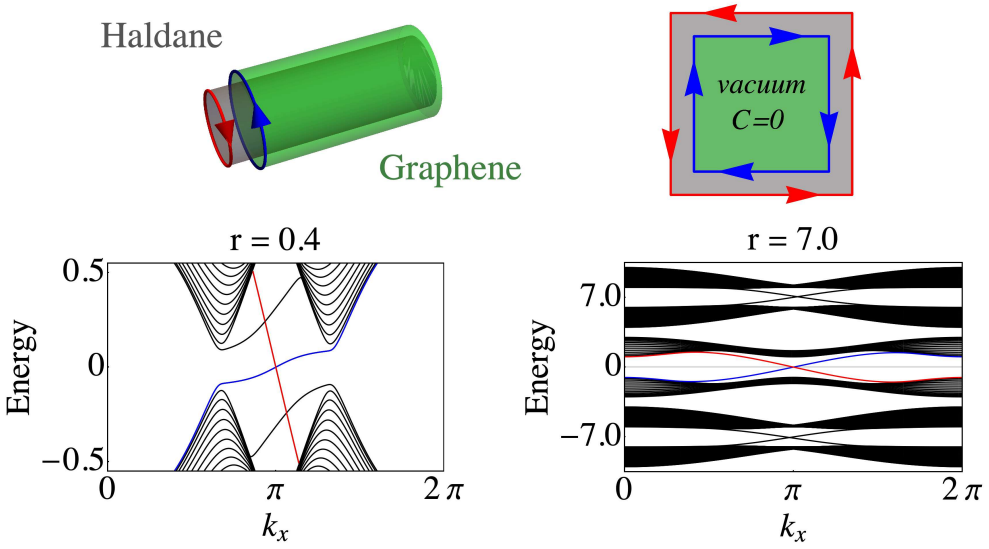

FIGURE 3.3: Band structures for $t_1 = 1$ and $t_2 = 1/3$ in the weak and strong-coupling limits for a cylinder geometry; the lattice spacing is $a = 1$. On the left, we zoom on the two low-energy graphene bulk bands. In the green region of 60 unit cells, the total Chern number of the two lowest bands is zero and in the grey region (of 14 unit cells) the system is a Haldane model. We observe two counter-propagating edge modes with different velocities at zero energy until $r \sim t_2$. For very strong couplings, at zero energy, the counter-propagating edge modes are only linked to properties of the Haldane region.

In summary, upon imposing a finite coupling r between the two layers of the Haldane-graphene honeycomb model, the wavefunction becomes singular in one sector. The singularity can be lifted upon exchanging positive and negative energy bands in this sector. Therefore, the Berry phase jumps by 2π at only *one* of the two Dirac points.

3.4 Edge properties and strong coupling limit

3.4.1 Counter-propagating edge modes at different velocities

Now, we study in more detail the edge properties. For Haldane and graphene layers of equal size, for $r \neq 0$, we find the formation of a gap at the edges at half-filling, resulting from the hybridization of the zig-zag edge mode of graphene —

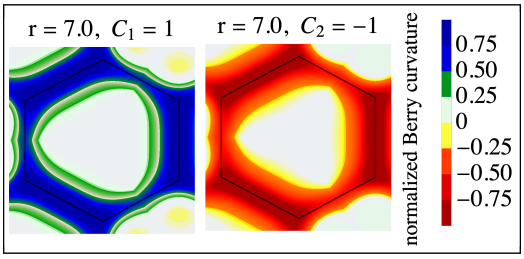

FIGURE 3.4: Berry curvature for the two lowest energy bands at strong coupling $r = 0.7$ ($t_1 = 1$ and $t_2 = 1/3$).

present at $r = 0$ — with the topological edge mode (see black edge modes in Fig. 3.3 (left) corresponding to the right boundary of the green cylinder). This is also consistent with the Kane-Mele model [69], where the r coupling at the edges corresponds to a spin-flip process which breaks the $\mathcal{Z}_2$ symmetry and opens a gap similar to the effect of the Mott transition [47, 70]. To confirm that a chiral edge state has now appeared in the graphene layer at half-filling moving in opposite direction as the edge state in the Haldane layer, in agreement with

$$(C_-^h - C_-^g) = 2 \tag{3.29}$$

in the bulk for $r \neq 0$ [71], we suggest to suppress smoothly the r tunnel coupling at the left edge. Numerically, we check that for more than 10 unit cells in the grey region, results are stable. Fig. 3.3 then shows two counter-propagating edge modes with different velocities, due to the different gaps in the two layers, crossing the chemical potential at half-filling (or energy zero). Alternatively, one could build a slightly smaller layer and observe two counter-propagating edge modes, one in each layer.

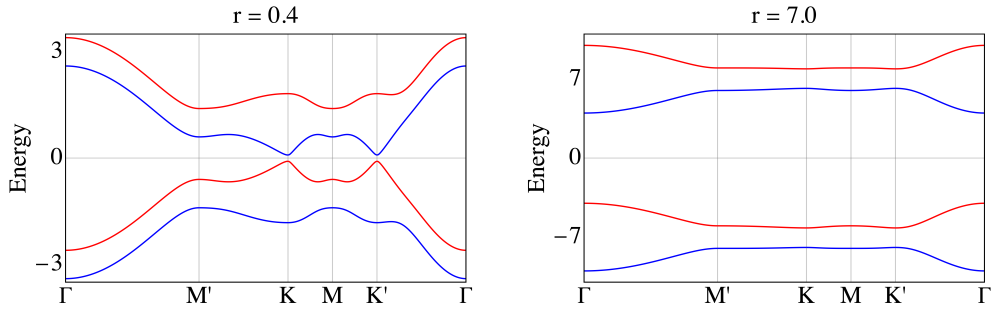

FIGURE 3.5: Evolution of the four energy eigenstates for two values of the tunnel coupling element r between layers with $t_1 = 1$ and $t_2 = 1/3$. The right figure with $r = 7.0$ corresponds to the strong coupling case. The bands are now coloured according to their Chern number. Blue means Chern number $+1$ and red Chern number -1. The Γ, K, K', M and M' points are defined in the theory section. The energy scale is in terms of the nearest neighbor hopping amplitude t_1.

3.4.2 Strong coupling limit

The strong coupling limit of the Haldane-graphene model describes the case where the hopping parameter between the two layers r is large, i.e.

$$r \gg (t_1, t_2). \tag{3.30}$$

Analytically, we define the field operators

$$\zeta_{\pm} = 1/\sqrt{2}(c_{gA} \pm c_{hA}) \tag{3.31}$$

hybridizing the sublattices A of the two layers and

$$\chi_{\pm} = 1/\sqrt{2}(c_{gB} \pm c_{hB}) \tag{3.32}$$

hybridizing the sublattices B of the two layers. Here, $c^{\dagger}_{hA}$ and $c^{\dagger}_{hB}$ represent creation operators at sublattice A and B in the Haldane layer and analogously for $c^{\dagger}_{gA,B}$ in the graphene layer.

To show that the strong-coupling description is very general we introduce the magnetic fields $\mathbf{d}_1$ and $\mathbf{d}_2$ associated with the two layers, that we shall rewrite in the hybridized basis. To find the effective Hamiltonian in the basis $[\zeta-, \chi_-, \zeta+, \chi_+]$, we can equivalently perform a unitary transformation on the Hamiltonian such that the Hamiltonian becomes

$$\tilde{\mathcal{H}}(\mathbf{k}) = \begin{pmatrix} -r\mathcal{I} + \frac{(\mathbf{d}_1+\mathbf{d}_2)}{2} \cdot \boldsymbol{\sigma} & \frac{(\mathbf{d}_1-\mathbf{d}_2)}{2} \cdot \boldsymbol{\sigma} \\ \frac{(\mathbf{d}_1-\mathbf{d}_2)}{2} \cdot \boldsymbol{\sigma} & r\mathcal{I} + \frac{(\mathbf{d}_1+\mathbf{d}_2)}{2} \cdot \boldsymbol{\sigma} \end{pmatrix}. \tag{3.33}$$

The energy spectrum shows two pairs of bands centered around $\pm r$, see Fig. 3.5, and described by a Haldane model with an effective magnetic field in $\mathbf{k}$ space which is equivalent to $(\mathbf{d}_1 + \mathbf{d}_2) \cdot \boldsymbol{\sigma}/2$. The off-diagonal terms couple band pairs of different energy which do not affect the low-energy theory. For the Haldane-graphene bilayer with $\mathbf{d}_1 = \mathbf{d}_g$ and $\mathbf{d}_2 = \mathbf{d}_h$, Berry curvatures of the two lowest bands for $r \gg t_2$ are shown in Fig. 3.4.

In the strong coupling case at $r = 7.0$ of Fig. 3.3, the two lowest "hybrid" bands are still described by a total Chern number zero and the bulk green region now behaves as the vacuum. Furthermore, we now observe two counter-propagating edge modes with equal velocities at zero energy, when suppressing the tunnel coupling at one edge in the cylinder geometry (in the grey region). By making one layer slightly larger than the other, the two edges modes now entirely connect to the Haldane bulk bands of the grey region.

Note that at quarter filling (implying that the particle density of the two layers satisfy $(n_g = n_h = 1/4)$) only the lowest band in Fig. 3.3 (right) should be filled, and the system reveals a topological phase with Chern number 1. The edge structure shows on average $1/2$ particle in one layer moving together with $1/2$ particle in the other layer.

3.5 Experimental realization

3.5.1 The Haldane honeycomb model in ultra cold atoms

Before we can make suggestion on how to observe the bilayer effects outlined above, we need to understand how the topological Haldane model can be realized in ultra cold atoms experiments [25, 46].

In optical lattices, one can apply a time-dependent force $\mathbf{F}(t) = -m\ddot{\mathbf{r}}_{lat}(t)$ corresponding to a periodic shaking protocol of the lattice. The Hamiltonian then becomes

$$\mathcal{H}_{lat} = \mathcal{H}_0 + \sum_i (\mathbf{F}(t) \cdot \mathbf{r}_i) c_i^\dagger c_i. \tag{3.34}$$

Here, c_i corresponds to an atom at site i with mass m on a honeycomb optical lattice and $\mathcal{H}_0$ corresponds to the Hamiltonian of graphene with nearest-neighbor tunneling coupling. The additional momentum can be absorbed by going to the reference frame $-\mathbf{q}_{lat} = -m\dot{\mathbf{r}}_{lat}(t)$. In this frame, the tight-binding Hamiltonian corresponding to nearest-neighbor tunneling becomes modified as

$$\mathcal{H}'_{lat} = \sum_{\langle i;j \rangle} e^{i\mathbf{q}_{lat}\cdot\mathbf{r}_{ij}} t_{ij} c_i^\dagger c_j. \tag{3.35}$$

In the case of a periodically driven system, where $\mathcal{H}'_{lat}$ and therefore $\mathbf{r}_{lat}(T)$ are periodic functions in time, one can then apply the Floquet theory, where an effective Hamiltonian is obtained from the unitary time-evolution operator $U(T,0)$ over one period T of driving, such that

$$\frac{i\hbar}{T} \log(U(T,0)) = \mathcal{H}_{eff}. \tag{3.36}$$

Using the shaking procedure for the honeycomb optical lattice, one can then realize an effective Hamiltonian in the wave-vector space [46]

$$\mathcal{H}(\mathbf{k}) = \begin{pmatrix} M + \sum_i 2t_{AA}\cos(\mathbf{k}\cdot\mathbf{b}_i) & \sum_i 2t_{AB}e^{-i\mathbf{k}\cdot\mathbf{a}_i} \\ \sum_i 2t_{AB}e^{i\mathbf{k}\cdot\mathbf{a}_i} & -M + \sum_i 2t_{BB}\cos(\mathbf{k}\cdot\mathbf{b}_i) \end{pmatrix}, \tag{3.37}$$

acting on the Hilbert space of sublattices A and B. The offset M between A and B sites corresponds to the Semenoff mass [35]. The hopping term t_{AB} contributes to the nearest-neighbor graphene term t_1, whereas t_{AA} and t_{BB} generate the t_2 terms in the Haldane model. To realize the topological phase of the Haldane model, the key point is to use phase factors in the time-modulation of the lattice such that $t_{AA} = -t_{BB}$ and $t_{AA} = |t_2|e^{i\Phi}$, where the phase Φ corresponds to the Peierls phase.

3.5.2 The case of the bilayer system

The goal is to build, for instance, two graphene optical lattices. Then, one could apply the same time-dependent force or Floquet modulation on the two layers, as described above, to implement the same parameters t_1 and t_2 in the two layers.

In the next step, laser assisted tunneling generates the coupling of atoms of one layer to those of the other layer, such that the r tunnel coupling would couple sublattices A of the two layers on the one hand and sublattices B of the two layers on the other hand. Another possibility would be to use one optical lattice and two species (of synthetic dimensions).

In practice, one would however encounter a crucial problem when attempting to realize a Haldane-graphene bilayer model. When setting up one layer of a Haldane model by globally shaking the lattice, the shaking would necessarily also occur in the other layer (the graphene layer), thus turning both layers into Haldane layers.

However, there is a way around that would allow us to distinguish the two layers. We propose the following idea. Instead of attempting to realize a Haldane-graphene bilayer system in a optical lattice context, one would rather consider a Haldane-Haldane bilayer system. In order to be able to distinguish between the two layers and to force a Berry curvature jump in *one layer at a time* (when increasing the coupling parameter r), we propose to induce static and asymmetric Semenoff masses M_1 and M_2 in the layers. The net offset Semenoff mass will force one of the layers to encounter a Berry phase jump at smaller r than the other.

3.5.3 The Haldane-Haldane model

In order to propose an experimental setup that would allow to observe the Berry phase jump as it occurs in the Haldane-graphene bilayer model, cf. Fig. 3.3, we propose a Haldane-Haldane bilayer model.

Mathematically, we define this model analogously to the Haldane-graphene Hamiltonian, Eq. 3.3, as

$$\mathcal{H}_{hh}(\mathbf{k}) = \begin{pmatrix} \mathbf{d}_{h1} \cdot \boldsymbol{\sigma} + \epsilon_h \cdot \mathcal{I} & r \cdot \mathcal{I} \\ r \cdot \mathcal{I} & \mathbf{d}_{h2} \cdot \boldsymbol{\sigma} + \epsilon_h \cdot \mathcal{I} \end{pmatrix}, \tag{3.38}$$

where $\mathbf{d}_{h1,2}$ describe Haldane models that come with the same set of parameters for nearest and next-nearest neighbor hopping t_1 and t_2, but that differ in their corresponding static Semenoff masses. To this end, we adjust the z component of the magnetic field $d_z^{h1,2}$ (cf. Eq. 2.34) to contain the Semenoff mass $M_{1,2}$

$$d_z^{h1,2}(\mathbf{k}) = M_{1,2} - 2t_2 \sin\Phi \sum_p \sin(\mathbf{k} \cdot \mathbf{b}_p). \tag{3.39}$$

To observe the jumps of the Berry phases as described for the Haldane-graphene bilayer model Fig. 3.3, we suggest to start with two different off-sets M_1 and M_2

in the two Haldane layers. In both layers, one starts with M_1 and M_2 smaller than

$$|d_z(\mathbf{k} \sim \pm\mathbf{K})| = 3\sqrt{3}t_2 \sin\Phi. \tag{3.40}$$

That means in the absence of coupling between the two layers, the two lowest Bloch bands are described by a Chern number $+1$, producing a phase with total Chern number $C = 2$. That means, we start with both layers in the topological phase of the Haldane model, cf. Fig. 2.3.

Assuming unequal masses M_1 and M_2, we observe two phase transitions by switching on the coupling parameter r. At the two transitions, we report a jump of Berry phase at one Dirac point only by analogy to the situation of the Haldane-graphene layers' situation at small r. If we start with $M_2 > M_1$, cf. Fig. 3.6, the gap for the bands 2 at the $\mathbf{K}'$ point is (much) smaller than the gap separating the upper and lower bands 4 and 1 and therefore second-order processes or particle-hole pair virtual processes through these bands can still affect the gap of band 2, which then explains the gap closing at the $\mathbf{K}'$ point at the first transition. We qualitatively predict that the gap would close at the $\mathbf{K}'$ point roughly when

$$3\sqrt{3}t_2 \sin\Phi - M_2 - r^2/(3\sqrt{3}\sin\Phi t_2 - M_1) \approx 0. \tag{3.41}$$

Here, we consider the effective mass term in one of the Haldane layers, by taking into account that through interlayer coupling r, another effective mass term is also added to this layer due to topology in the other layer. This is essentially the mass term that we saw was previously introduced in the graphene layer of the Haldane-graphene model through the effective hopping amplitude t_{eff}, Eq. 3.12.

We check numerically that this equation reproduces the features of the first transition line. At large r, the total Chern number of the two lowest bands must be zero in agreement with the theory. We show the band structure and Berry curvature evolve as a function of r, in particular for the intermediate region with

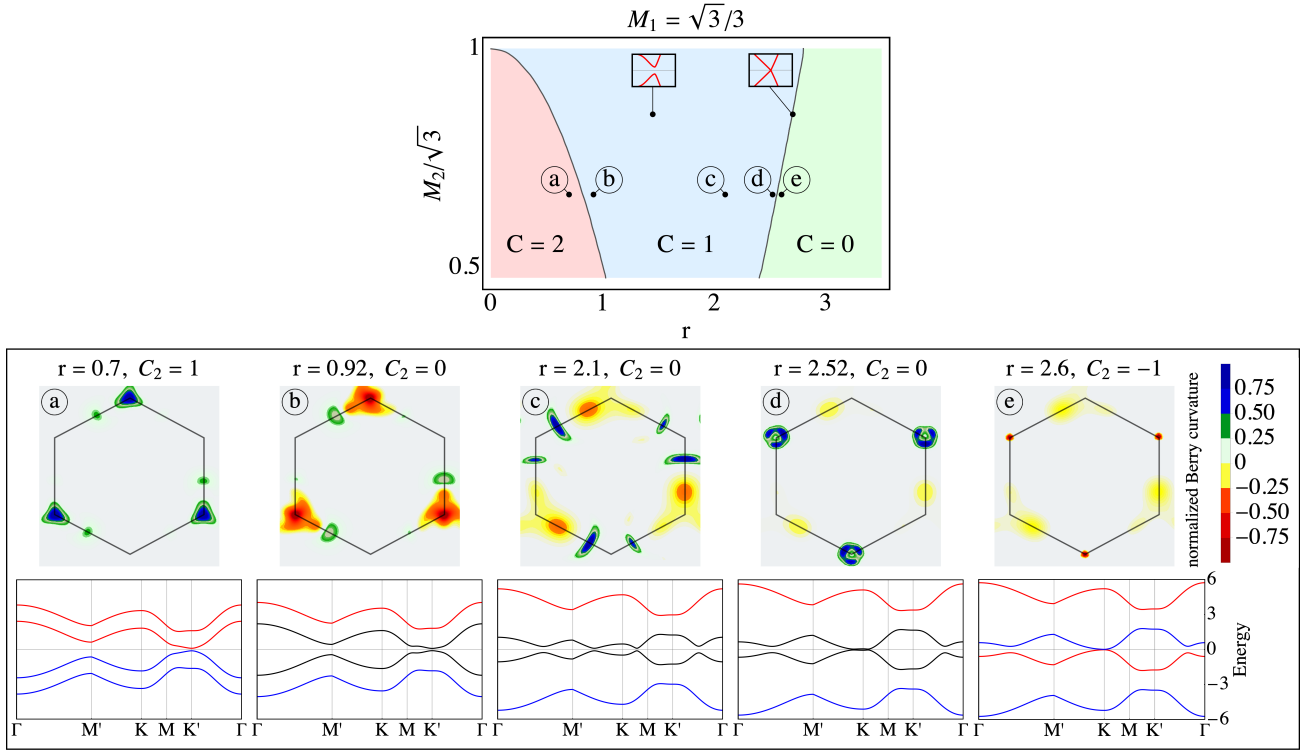

FIGURE 3.6: Upper: Numerical Phase diagram for two Haldane layers at half-filling ($t_1 = 1$, $t_2 = 1/3$, $\Phi = \pi/2$) with different Semenoff masses, where $M_1 = \sqrt{3}/3$ is fixed. Lower: Berry curvatures and band structures for increasing coupling r along $M_2 = 2\sqrt{3}/3$. At the first (second) phase transition, the bands touch at the $\mathbf{K}'$ ($\mathbf{K}$) point and the Berry curvature flips sign in its vicinity. In the band structures, the colors refer to the Chern number of the bands: Blue means Chern number $+1$, black Chern number 0, and red Chern number -1. The properties of the Bloch bands could be checked with fermions and bosons, at a single particle level.

$C = 1$, where the gap at the **K** point progressively diminishes whereas the gap at the **K**′ point now stays finite. When the gap closes at the **K** point, then we again observe a sign change of the Berry curvature at this point, then producing the entrance towards the $C = 0$ phase. Essentially, to enter the $C = 0$ phase, the band 2 must flip its Chern number to $C_2 = -1$ then closing the gap at the **K** point.

For equal masses $M_1 = M_2$, a band crossing effect occurs in the intermediate region for $r \sim 0.9$, therefore the total Chern number of the two lowest bands seemed to progressively change from $C = 2$ to $C = 0$, as described in Fig. 3.7.

The two phase transitions then do not occur for this case, and there is a band inversion between band 2 and band 3 when $r = 3t_1$ for $t_2 = 1/3$. But, as soon as $M_1 \neq M_2$, the system tends to restore the $C = 1$ region as well as the two transitions associated with the changes in the Berry curvatures at the Dirac points.

While in fact, from our discussion the physical meaning of the region with band crossing effects is not quite clear, the issue has in the meantime been addressed in another work, Ref. [72]. In fact, the band crossing effect was found to hide a topological semimetal with topological number $C = 1/2$ per plane.

3.6 Conclusion

To summarize, we have presented a proximity effect from a topological Chern insulator on a graphene layer. Particle-hole processes at the interface induce a gap in the graphene layer and therefore, the two lowest filled energy bands show inverse quantized Chern numbers $+1$ and -1. We have illustrated the bulk-edge correspondence in relation with the Kane-Mele model [73], and with general bulk-edge correspondence in the ultra strong-coupling limit.

The effective model built in **k**-space close to the Dirac points could be realized in graphene bilayers through circularly polarized light coupling to one layer more prominently [38]. We have generalized the Berry phase jump phenomenon

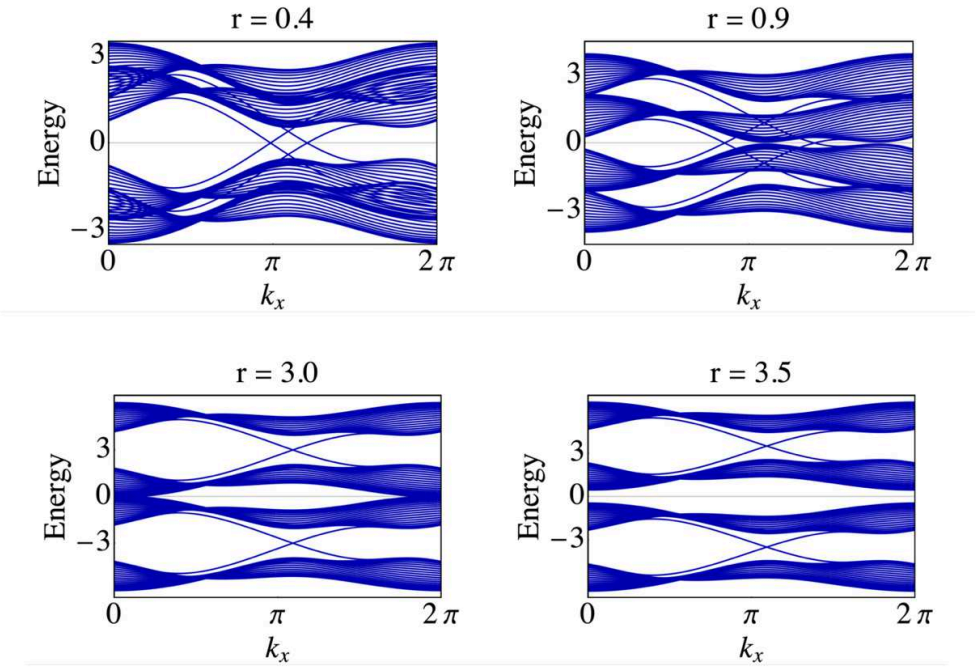

FIGURE 3.7: Evolution of edge spectra in the case of two Haldane layers, with masses $M_1 = M_2 = \sqrt{3}/3$. Again, we fix $t_1 = 1$, $t_2 = 1/3, \Phi = \pi/2$.

to bilayer Haldane model. Furthermore, we have discussed implementations in cold atom thoroughly.

Chapter 4

Interaction effects in the Haldane honeycomb model

The system under consideration in the previous chapter was analytically solvable and thus allowed for a straight forward analysis in terms of band theory which made its rich phenomenology accessible. In this chapter, we will progress beyond the analytic regime by introducing electron-electron interaction effects in the Haldane honeycomb model.

Studying the effects of electron-electron interactions on a system can be done with different goals or points of view. On the one hand, it is an important question to understand the stability of a phase (in this case the stability of a Chern insulator phase) towards the presence of interactions. On the other hand, interaction effects can lead to the emergence of new phenomena such as the Kondo effect [74] or the Mott transition [75].

In this chapter we study the important example of the interacting Haldane honeycomb model and address two main questions: Firstly, how can we effectively describe the stability of the topological phase in the Haldane honeycomb model towards electron-electron interactions? And secondly, how and when are topological properties of the model destroyed when interaction effects become more important, i.e. what is the nature of the Mott transition?

Note that while some progress has been made in the description of interacting Chern systems, in the bosonic case [15, 16], and both for spinless [15, 17, 18, 19] and spinfull [20, 21, 22, 23, 24] fermions, and more generally in the description of interacting topological systems [31], several central questions remain open. Most importantly, the system we wish to study in this chapter, i.e. the interacting *spinless* interacting Haldane model has not been convincingly solved by means of an approximative model. The nature of the Mott transition has previously been studied using methods of exact diagonalization [15, 17] and suggested it be of first order. We will revisit this question within our approach and provide an explanation that reaffirms this result.

4.1 Stochastic variables and Mean field theory

4.1.1 The model Hamiltonian

We start by introducing a model Hamiltonian which we aim to turn into an effective Hamiltonian via mean field theory. We consider the model Hamiltonian

$$\mathcal{H} = \mathcal{H}_0 + \mathcal{H}_V, \tag{4.1}$$

where $\mathcal{H}_0$ is the Haldane honeycomb model for spinless fermions at half-filling [14] and $\mathcal{H}_V$ is the nearest neighbor interaction, i.e.

$$\begin{aligned} \mathcal{H}_0 &= -\sum_{\langle i,j\rangle} t_1 c_i^\dagger c_j - \sum_{\langle\langle i,j\rangle\rangle} t_2 e^{\pm i\Phi} c_i^\dagger c_j \\ \mathcal{H}_V &= V \sum_{\langle i,j\rangle} \left(n_i - 1/2\right)\left(n_j - 1/2\right). \end{aligned} \tag{4.2}$$

Here, t_1 represents the nearest-neighbor hopping strength which we set to unity hereafter $(t_1 = 1)$. Furthermore, $t_2 e^{\pm i\Phi}$ represents the next-nearest neighbor hopping term where we fix the Peierls phase to $\Phi = \pi/2$, for simplicity. Here, the

positive (negative) sign refers to (counter-) clockwise hopping and the second nearest-neighbors are represented through the lattice vectors $\boldsymbol{u}_i$ that we introduced in Eq. 2.24.

We can then write the next-nearest neighbor $\boldsymbol{b}_p$ displacements on the honeycomb lattice in terms of the nearest neighbor $\boldsymbol{a}_p$ displacements that we introduced in Eq. 2.25. That means, we write $\boldsymbol{b}_p$ as $\boldsymbol{b}_i = \boldsymbol{a}_j - \boldsymbol{a}_k$ where the tuple (i, j, k) is a permutation of the bond-tuple (x, y, z). As in Ref. [25], the $\boldsymbol{a}_p$ basis does not yield a Hamiltonian in Bloch form. Rather, we perform a gauge transform on the Hamiltonian to the basis, given by the lattice vectors $\boldsymbol{u}_i$, see Fig. 2.1.

4.1.2 General remarks on the decoupling scheme

The model Hamiltonian that we considered in chapter 3 came in a quadratic form. Therefore, we were able to treat it directly by means of band theory. In this chapter, we consider interaction effects. Hence, we need to find a treatment of the quartic terms such as

$$c_i^\dagger c_i c_j^\dagger c_j \tag{4.3}$$

that appear in our Hamiltonian $\mathcal{H}$. Previous studies [19, 18] have suggested that at a mean field level the quartic interaction term can be decoupled into a charge density wave (CDW) order parameter which then acts as a staggered potential in sublattice space on $\mathcal{H}_0$. Hence, decoupling into this channel results in a order parameter that controls the band gap of the Haldane model at the K-points and therefore has a direct influence on the topological nature of the bands. This seems like a reasonable approach and a straightforward way, proposed in Ref. [18], would be to rewrite $\mathcal{H}_V$ exactly as

$$\mathcal{H}_V = V \sum_{\langle i,j \rangle} (n_i - 1/2)\,(n_j - 1/2) = \frac{V}{4} \sum_{\langle i,j \rangle} (n_i - n_j)^2 \tag{4.4}$$

in order to find a simple mean-field theory for the CDW order.

Crucially however, this ansatz does not take into account the fact that the correlator $\langle c_i^\dagger c_j \rangle$ is finite in the Haldane model (in the form of nearest neighbor hopping) and therefore contributes to the overall interaction energy $\langle c_i^\dagger c_i c_j^\dagger c_j \rangle$. Hence, a valid decoupling scheme involving particle-hole channels has not been considered previously in the case of interacting topological phases [19, 18]. When particle-hole channels are not included, one finds the Mott phase transition to be second-order [18].

Therefore, we propose to construct the most general decoupling scheme possible that includes all contributing channels. We will verify this scheme by validating our through energy computations in chapter 4.2.

4.1.3 Decomposition of the quartic term

Let us start by rewriting

$$\begin{aligned} \mathcal{H}_V &= V \sum_{i,p} \left(n_i - \frac{1}{2} \right) \left(n_{i+p} - \frac{1}{2} \right) && (4.5) \\ &= V \sum_{i,p,r} \eta_r \left(c_i^\dagger \sigma^r_{i,i+p} c_{i+p} \right)^2 \\ &- \frac{V}{2} \sum_{i,p} \left(c_i^\dagger c_i + c_{i+p}^\dagger c_{i+p} - \frac{1}{2} \right), && (4.6) \end{aligned}$$

where i denotes a unit cell, p runs over the links (x, y, z), r runs over $(0, x, y, z)$ and σ^r denotes the Pauli matrices acting on sublattice space with basis $(i(A), i + p(B))$.

Here, we introduced the coefficients η_r in the second line. The above transformation (from Eq. 4.5 to Eq. 4.6) is exact as long as the coefficients η_r fulfill the the following relations

$$\eta_0 = -\eta_z, \qquad \eta_x = \eta_y, \qquad \frac{1}{4} = \eta_0 - \eta_x. \tag{4.7}$$

As previously noted, we wish in principle to choose the η_r such that the decoupling scheme incorporates particle-hole channels (i.e. $\eta_{x,y} \neq 0$) that contribute to the total energy. A priori, a generic choice of the η_r that will ultimately minimize the total energy of the effective Hamiltonian correctly, is not obvious. Rather, a choice of coefficients η_r needs to be justified by means of energetic analysis which will be conducted in chapter 4.2.

A posteriori, from the energetic point of view the correct choice of coefficients η_r is

$$-\eta_0 = \eta_x = \eta_y = \eta_z = -\frac{1}{8}. \tag{4.8}$$

We can now write down the partition function and action in momentum space as

$$\begin{aligned} \mathcal{Z} &= \int \mathrm{D}(\Psi, \Psi^\dagger) e^{-\mathcal{S}}, \\ \mathcal{S} &= \int_0^\beta \mathrm{d}\tau \sum_{\boldsymbol{k}} \Psi_{\boldsymbol{k}}^\dagger \left(\partial_\tau + \boldsymbol{h}_0(\boldsymbol{k}) \cdot \boldsymbol{\sigma}\right) \Psi_{\boldsymbol{k}} + \mathcal{H}_V \end{aligned} \tag{4.9}$$

with the spinor basis $\Psi_{\boldsymbol{k}}^\dagger = \left(c_{\boldsymbol{k}A}^\dagger, c_{\boldsymbol{k}B}^\dagger\right)$ such that

$$\begin{aligned} h_0^x(\boldsymbol{k}) &= -t_1 \sum_p \cos(\boldsymbol{k} \cdot \boldsymbol{a}_p), \\ h_0^y(\boldsymbol{k}) &= -t_1 \sum_p \sin(\boldsymbol{k} \cdot \boldsymbol{a}_p), \\ h_0^z(\boldsymbol{k}) &= -2t_2 \sum_p \sin(\boldsymbol{k} \cdot \boldsymbol{b}_p). \end{aligned} \tag{4.10}$$

4.1.4 Hubbard-Stratonovich transformations

Now, we decouple the quartic interaction term $\mathcal{H}_V$ via a Hubbard-Stratonovich transformation. We follow [76] and distinguish between $r \in \{x, y, z\}$ and $r \in \{0\}$ since the corresponding exponential terms come with different signs (due to the choice of the η_r in Eq. 5.26).

For $r \in \{x, y, z\}$ we obtain

$$\exp\left(\frac{V}{8}\sum_{i,p}\left(c_i^\dagger \sigma^r_{i,i+p} c_{i+p}\right)^2\right) = \int \mathrm{D}\phi^r \exp\left(-\sum_{i,p} 2V(\phi^r_{i+p/2})^2 + V\phi^r_{i+p/2}\left(c_i^\dagger \sigma^r_{i,i+p} c_{i+p}\right)\right), \tag{4.11}$$

and for $r = 0$

$$\exp\left(-\frac{V}{8}\sum_{i,p}\left(c_i^\dagger \sigma^0_{i,i+p} c_{i+p}\right)^2\right) = \int \mathrm{D}\phi^0 \exp\left(-\sum_{i,p} 2V(\phi^0_{i+p/2})^2 + iV\phi^0_{i+p/2}\left(c_i^\dagger \sigma^0_{i,i+p} c_{i+p}\right)\right). \tag{4.12}$$

Here we introduced for each r an auxiliary field $\phi^r_{i+p/2}$ on each link between lattice sites i (on sublattice A) and $i+p$ (on sublattice B). The fields ϕ^x and ϕ^y are particle-hole channels, ϕ^0 corresponds to a chemical potential and ϕ^z to a staggered chemical potential in sublattice space that captures CDW order. Importantly, ϕ^z acts at the same time as a Semenoff mass term on the Haldane model and therefore controls the topological Chern number of the bands.

Now, we rewrite the decoupled interaction part in Fourier space and obtain the partition function and action

$$\mathcal{Z} = \int \mathrm{D}(\Psi, \Psi^\dagger, \phi^0, \phi^x, \phi^y, \phi^z) e^{-\mathcal{S}}, \tag{4.13}$$

$$\mathcal{S} = \int_0^\beta \mathrm{d}\tau \sum_{\boldsymbol{k}} \Psi^\dagger_{\boldsymbol{k}} \left(\partial_\tau + \boldsymbol{h}_0(\boldsymbol{k}) \cdot \boldsymbol{\sigma}\right) \Psi_{\boldsymbol{k}} + \sum_{\boldsymbol{k},\boldsymbol{q},p} \Psi^\dagger_{\boldsymbol{q}} h_V(\boldsymbol{k}, \boldsymbol{q}, p) \Psi_{\boldsymbol{k}} + \sum_{\boldsymbol{k},r} 6V\phi^r_{\boldsymbol{k}}\phi^r_{-\boldsymbol{k}}, \tag{4.14}$$

where we introduced the matrix $h_V(\boldsymbol{k},\boldsymbol{q},p)$ which can be interpreted as an interaction density matrix. Explicitly, it reads

$$h_V(\boldsymbol{k},\boldsymbol{q},p) = V\begin{pmatrix} e^{-\frac{i}{2}(\boldsymbol{k}-\boldsymbol{q})\cdot\boldsymbol{a}_p}\left(i\phi^0_{\boldsymbol{k}-\boldsymbol{q}}+\phi^z_{\boldsymbol{k}-\boldsymbol{q}}\right)-\frac{1}{2} & e^{\frac{i}{2}(\boldsymbol{k}+\boldsymbol{q})\cdot\boldsymbol{a}_p}\left(\phi^x_{\boldsymbol{k}-\boldsymbol{q}}-i\phi^y_{\boldsymbol{k}-\boldsymbol{q}}\right) \\ e^{-\frac{i}{2}(\boldsymbol{k}+\boldsymbol{q})\cdot\boldsymbol{a}_p}\left(\phi^x_{\boldsymbol{k}-\boldsymbol{q}}+i\phi^y_{\boldsymbol{k}-\boldsymbol{q}}\right) & e^{\frac{i}{2}(\boldsymbol{k}-\boldsymbol{q})\cdot\boldsymbol{a}_p}\left(i\phi^0_{\boldsymbol{k}-\boldsymbol{q}}-\phi^z_{\boldsymbol{k}-\boldsymbol{q}}\right)-\frac{1}{2}\end{pmatrix}. \tag{4.15}$$

In principle, one could also assign an imaginary time variable τ to the stochastic variables. Then this would result in a frequency dependence of the variables $\phi^r_{\boldsymbol{k}}$.

Below, we develop a variational approach to evaluate the stochastic variables within the ground state properties through an energy-minimization protocol. Therefore, we consider below a time-independent, static model and therefore restrict the analysis to the zero frequency contribution. For ground-state observables, this stochastic variational approach is in good agreement with an iDMRG approach which was performed as a complementary method to validate the results [26]. As we also show below, fluctuations of the stochastic variables around their value for the minimum of energy is well controlled.

Furthermore, we restrict the discussion to leading contribution in k-space for which scattering does not change momentum. Hence, we keep only the zero momentum contribution, i.e. $\boldsymbol{k}-\boldsymbol{q}=0$. It's important to remind that sampling stochastic variables in time suffers from the sign problem for the fermionic Haldane model, which justifies our present approach. It should be emphasized that to reproduce ground-state properties, one cannot ignore the particle-hole channel ϕ^x.

The action $\mathcal{S}$ now takes the form

$$\mathcal{S} = \sum_{\boldsymbol{k}}\Psi^\dagger_{\boldsymbol{k}}\left(\boldsymbol{h}_0(\boldsymbol{k})\cdot\boldsymbol{\sigma}+\sum_p h_V(\boldsymbol{k},p)\right)\Psi_{\boldsymbol{k}}+\sum_{\boldsymbol{k},r}6V\phi^r_{\boldsymbol{k}}\phi^r_{-\boldsymbol{k}}, \tag{4.16}$$

where the interaction density matrix now reads

$$h_V(\boldsymbol{k}, p) = V \begin{pmatrix} -\left(\phi^0 + \frac{1}{2}\right) + \phi^z & e^{i\boldsymbol{k}\cdot\boldsymbol{a}_p}\left(\phi^x - i\phi^y\right) \\ e^{-i\boldsymbol{k}\cdot\boldsymbol{a}_p}\left(\phi^x + i\phi^y\right) & -\left(\phi^0 + \frac{1}{2}\right) - \phi^z \end{pmatrix}. \tag{4.17}$$

Here, we skipped the zero-momentum index of the fields, i.e. $\phi^r \equiv \phi^r_0$, and re-defined the chemical potential $-i\phi^0 \to \phi^0$ such that ϕ^0 is now real for the matrix $h_V(\boldsymbol{k}, p)$ to be Hermitian (where it was imaginary before the substitution, such that $i\phi^0$ was real).

We set

$$\mathcal{H}_{\mathrm{mf}}(\boldsymbol{k}) = \boldsymbol{h}_0(\boldsymbol{k}) \cdot \boldsymbol{\sigma} + \sum_p h_V(\boldsymbol{k}, p), \tag{4.18}$$

and finally arrive at the effective mean field Hamiltonian

$$\mathcal{H}_{\mathrm{mf}} = \sum_{\boldsymbol{k}} \Psi^\dagger_{\boldsymbol{k}} \mathcal{H}_{\mathrm{mf}}(\boldsymbol{k}) \Psi_{\boldsymbol{k}} \tag{4.19}$$

where the mean field Hamiltonian density in matrix form reads

$$\mathcal{H}_{\mathrm{mf}}(\boldsymbol{k}) = \begin{pmatrix} \gamma(\boldsymbol{k}) - 3V(\phi^0 + \frac{1}{2}) & -g(\boldsymbol{k}) \\ -g^*(\boldsymbol{k}) & -\gamma(\boldsymbol{k}) - 3V(\phi^0 + \frac{1}{2}) \end{pmatrix}, \tag{4.20}$$

with the functions $\gamma(\boldsymbol{k})$ and $g(\boldsymbol{k})$ defined as

$$\gamma(\boldsymbol{k}) = 3V\phi^z - 2t_2 \sum_p \sin(\boldsymbol{k} \cdot \boldsymbol{b}_p), \tag{4.21}$$

$$g(\boldsymbol{k}) = [t_1 - V(\phi^x + i\phi^y)] \sum_p \left(\cos(\boldsymbol{k} \cdot \boldsymbol{a}_p) - i \sin(\boldsymbol{k} \cdot \boldsymbol{a}_p)\right). \tag{4.22}$$

The term $3V\phi^z$ assumes the role of a Semenoff mass term [35] in the Haldane model, whereas the fields ϕ^x and ϕ^y renormalize the nearest neighbor hopping amplitude t_1.

The field ϕ^0 can be absorbed in the chemical potential and will be fixed to $\phi^0 =$

$-1/2$ at half-filling. The field ϕ^z changes sign in sublattice space and therefore plays the role of a staggered chemical potential. On the one hand, it measures the particle density difference between sublattices A and B, and captures CDW order. Furthermore, it acts as a Semenoff mass term [35] on the Haldane model and therefore controls the Chern number of the system [14]. The variables ϕ^x and ϕ^y dress the nearest-neighbor hopping term and assuming t_1 is real then this favors $\phi^y = 0$ while $\phi^x \neq 0$. The ϕ^z variable is also real in the definition of the Hubbard-Stratonovitch transformation.

4.1.5 Self consistent mean field equations from a variational approach

Before deriving the self-consistent equations of the mean field Hamiltonian Eq. 4.20, we provide a general remark on the derivation of self-consistent mean field equations.

Consider some general Hamiltonian $\mathcal{H} = \mathcal{H}_t + \mathcal{H}_{Int}$ with a quadratic, kinetic part H_t and a quartic interaction part of the form $H_{Int} = -\sum_{i,j} U_{ij} c_i^\dagger c_i c_j^\dagger c_j \equiv -\sum_{i,j} n_i U_{ij} n_j$ with interaction matrix U_{ij}. The quartic term can be decoupled by means of a Hubbard-Stratonovich transformation as [77, 76]

$$\exp\left(n_i U_{ij} n_j\right) = \int \mathrm{d}\phi \exp\left(-\phi^i U_{ij} \phi^j - 2\phi^i U_{ij} n_j\right), \tag{4.23}$$

where we introduced some Gaussian auxiliary variable ϕ. From the partition function and action

$$\begin{aligned} \mathcal{Z} &= \int \mathrm{D}(c, c^\dagger, \phi) \exp\left(-\mathcal{S}\right), \\ \mathcal{S} &= \int_0^\beta \mathrm{d}\tau \sum_{i,j} c_i^\dagger \left(\partial_\tau + h_t\right) c_j + \phi^i U_{ij} \phi^j + 2\phi^i U_{ij} n_j, \end{aligned} \tag{4.24}$$

one then usually [77, 78] computes the self consistent mean field equations via

$$\left\langle \frac{\delta \mathcal{S}}{\delta \phi^i} \right\rangle \stackrel{!}{=} 0, \tag{4.25}$$

which would yield in the above example

$$0 = \left\langle U_{ij}\phi^j + 2U_{ij}n_j \right\rangle \Rightarrow \phi^j = -2\left\langle n_j \right\rangle. \tag{4.26}$$

Now, the problem is that this result is not unique. The auxiliary field ϕ can be thought of as gauge field. Essentially, we can make a transformation as $\phi^i \to \alpha\phi^i$ in Eq. 4.23 with some factor α to obtain

$$\mathcal{S} = \int_0^\beta \mathrm{d}\tau \sum_{i,j} c_i^\dagger \left(\partial_\tau + h_t\right) c_j + \alpha^2 \phi^i U_{ij} \phi^j + 2\alpha \phi^i U_{ij} n_j. \tag{4.27}$$

This produces the self-consistent mean field equation

$$\left\langle \frac{\delta \mathcal{S}}{\delta \phi^i} \right\rangle \stackrel{!}{=} 0, \qquad \Rightarrow \qquad \phi^j = -\frac{2}{\alpha}\left\langle n_j \right\rangle. \tag{4.28}$$

Hence, the self-consistent mean field equation depends on α and is therefore not gauge independent. The problem arises, as we only minimize the action (or energy) of the decoupled, ϕ-dependent Hamiltonian. Instead, we need to minimize the energy of the decoupled Hamiltonian (which can be seen as a choice of a trial Hamiltonian) with respect to the original, quartic Hamiltonian. This can be done in the following way.

Let $\mathcal{H}_{\mathrm{mf}}$ be (a choice of) a mean field or trial Hamiltonian and $\mathcal{H}$ the original, full Hamiltonian. Then, we can rewrite formally $\mathcal{H} = \mathcal{H}_{\mathrm{mf}} + (\mathcal{H} - \mathcal{H}_{\mathrm{mf}})$. On the level of the free energy it follows the Bogoliubov inequality [79, 80]

$$\mathcal{F} \leq \mathcal{F}_{\mathrm{mf}} + \left\langle \mathcal{F} - \mathcal{F}_{\mathrm{mf}} \right\rangle. \tag{4.29}$$

The right hand side of the inequality is a function of the mean field parameters and we need minimize it with respect to ϕ. In our case, for the full Hamiltonian $\mathcal{H}$ in Eq. 4.2 and the mean field Hamiltonian in Eq. 4.20, we obtain the following set of self-consistent mean field equations

$$\phi^0 = -\frac{1}{2}\left(\left\langle c_i^\dagger c_i\right\rangle + \left\langle c_{i+p}^\dagger c_{i+p}\right\rangle\right), \tag{4.30}$$

$$\phi^x = -\frac{1}{2}\left(\left\langle c_i^\dagger c_{i+p}\right\rangle + \left\langle c_{i+p}^\dagger c_i\right\rangle\right), \tag{4.31}$$

$$\phi^y = -\frac{1}{2}i\left(-\left\langle c_i^\dagger c_{i+p}\right\rangle + \left\langle c_{i+p}^\dagger c_i\right\rangle\right), \tag{4.32}$$

$$\phi^z = -\frac{1}{2}\left(\left\langle c_i^\dagger c_i\right\rangle - \left\langle c_{i+p}^\dagger c_{i+p}\right\rangle\right), \tag{4.33}$$

or in short hand notation using Pauli matrices

$$\phi^r = -\frac{1}{2}\left\langle c_i^\dagger \sigma_{ij}^r c_j\right\rangle. \tag{4.34}$$

The real space amplitudes are evaluated as mean over all lattice sites, for instance

$$\begin{aligned}\left\langle c_i^\dagger c_{i+p}\right\rangle &= \frac{2}{N_{\text{sites}}}\sum_{\boldsymbol{k}} e^{i\boldsymbol{k}\cdot\boldsymbol{a}_p}\left\langle c_{\boldsymbol{k}A}^\dagger c_{\boldsymbol{k}B}\right\rangle \\ &= \frac{2}{N_{\text{sites}}}\sum_{\boldsymbol{k}}\sum_{\mu',\nu'} e^{i\boldsymbol{k}\cdot\boldsymbol{a}_p}\mathcal{M}^*_{\boldsymbol{k}A\mu'}\mathcal{M}_{\boldsymbol{k}B\nu'}\left\langle \gamma_{\boldsymbol{k}\mu'}^\dagger\gamma_{\boldsymbol{k}\nu'}\right\rangle \\ &= \frac{2}{N_{\text{sites}}}\sum_{\boldsymbol{k}}\sum_{\lambda} e^{i\boldsymbol{k}\cdot\boldsymbol{a}_p}\mathcal{M}^*_{\boldsymbol{k}A\lambda}\mathcal{M}_{\boldsymbol{k}B\lambda}.\end{aligned} \tag{4.35}$$

In the first line, we performed a Fourier transform of the creation and annihilation operators in real space. In the second line, we used $\gamma_{\boldsymbol{k}} = \mathcal{M}_{\boldsymbol{k}}^\dagger\psi_{\boldsymbol{k}}$ where $\mathcal{M}_{\boldsymbol{k}}$ is a unitary matrix that diagonalizes $\mathcal{H}_{\text{mf}}$. The new spinor basis fulfills $\left\langle \gamma_{\boldsymbol{k}\mu'}^\dagger\gamma_{\boldsymbol{k}\nu'}\right\rangle = \delta_{\mu'\nu'}$ for occupied states. In Eq. 4.36, μ' and ν' run over all states, whereas λ in Eq. 4.36 runs only over occupied states. The results below are obtained when solving the coupled equations above.

4.1.6 Numeric solution to the self consistent mean field equations

In Fig. 4.1a), we present a two-dimensional $t_2 - V$ phase diagram obtained from the variational the mean-field theory approach. We confirm the presence of two phases [15, 16], a Chern insulator (CI) phase with a perfectly quantized Chern number and a Mott or charge density wave (CDW) phase. The CDW phase is characterized by a non-zero value of $\langle n_A - n_B \rangle$ or ϕ^z; as long as $\langle n_A - n_B \rangle$ is not equal to unity, then ϕ^x can remain finite above the transition as a result of quantum fluctuations. Fig. 4.1c) shows the numerical solution of the mean field equations for $t_2 = 0.1$. The jump in the CDW order parameter ϕ^z indicates the first-order phase transition. Here, we give some physical insight on the occurrence of a jump in ϕ^z, which is evaluated at the wave-vector $\mathbf{k} - \mathbf{q} = \mathbf{0}$.

At the Mott transition, the gap closes at one Dirac point such that for the ground state we have $\langle n_A(\mathbf{K}) \rangle = \langle n_B(\mathbf{K}) \rangle$ whereas the gap remains visible at the other Dirac point such that $\langle n_A(\mathbf{K}') \rangle = 1$. In real space, the system behaves (approximately) as if $\langle n_A - n_B \rangle \approx 1/2$ on a given unit cell and $|\phi^z| \approx 1/4$. It's relevant to highlight that the variable ϕ^z entering in the diagonal terms of the 2×2 matrix describing h_V is taken at the wave-vector $\mathbf{k} - \mathbf{q} = 0$ instead of a Dirac point, corresponding then to an average on all the unit cells of the lattice in real space. This argument implies a jump in the quantum Hall conductivity at the Mott transition. The closing of the gap at the $\mathbf{K}$ point gives a critical interaction value $V_c \approx 4\sqrt{3}t_2$ to enter into the Mott regime, suggesting then a linear relation between V_c and t_2 as observed in the phase diagram. In the stochastic approach, the particle-hole channel allows us to determine quantitatively $\langle n_A(\mathbf{K}) \rangle$ and $\langle n_B(\mathbf{K}) \rangle$ and the value of ϕ^z at wave-vector $\mathbf{k} - \mathbf{q} = \mathbf{0}$ according to Eq. 4.36, which then results in the phase diagram of Fig. 4.1. The linear relation between V_c and t_2 remains visible for the range of studied parameters.

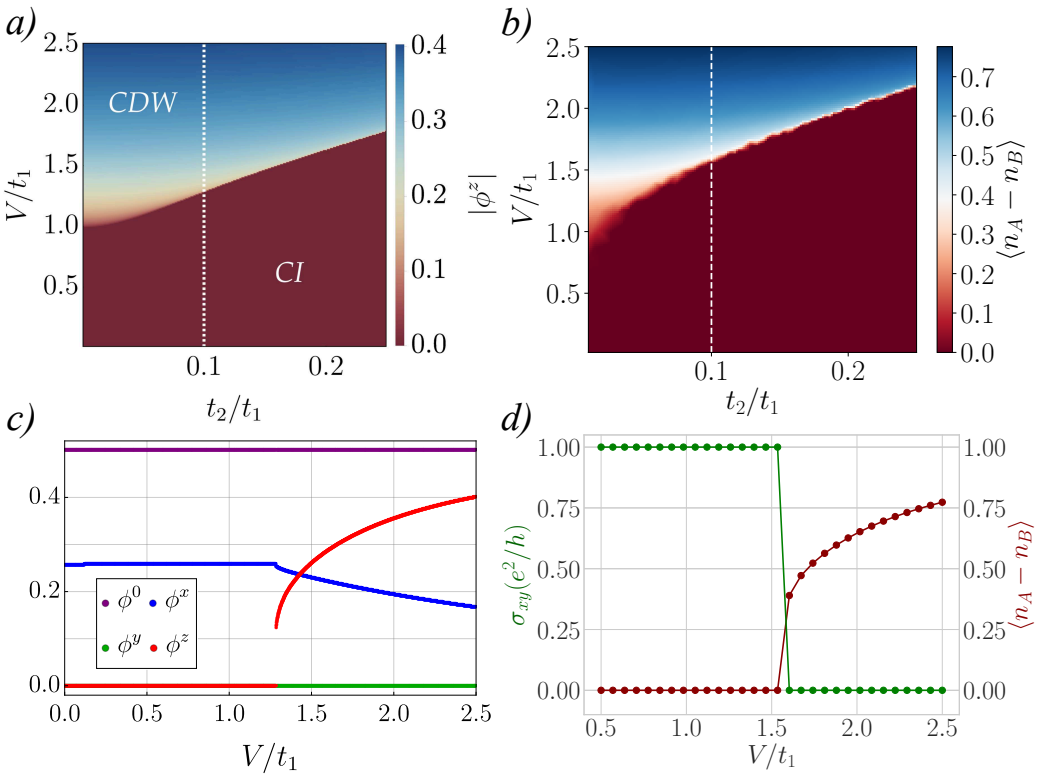

FIGURE 4.1: (a) $V - t_2$ mean field phase diagram from the method. The transition marks the condensation of the CDW order parameter ϕ^z. (b) Same phase diagram obtained with iDMRG [26]. (c) Absolute value of the self-consistent ϕ^r variable as a function of V for $t_2 = 0.1$. (d) Hall conductivity and $\langle n_A - n_B \rangle$ from iDMRG.

We compare [26] our mean field calculations with simulations using the infinite density matrix renormalization group (iDMRG) by means of the python package TENPY [81], written in the language of matrix product states. This numerical method calculates the ground-state of the model Eq. 4.2 in the infinite cylinder geometry, as well as the expectation of the CDW order parameter, $\langle n_A - n_B \rangle$, the Hall conductivity σ_{xy}, the correlation length ξ and the entanglement entropy S. The bond dimension χ is a measure of the maximum number of states kept by the algorithm, and sets the accuracy of the calculation. We have performed [26] calculations up to $\chi = 1200$ for cylinder circumferences of $L_y = 6, 12$ sites and our results show good convergence for bond dimensions as low as $\chi \gtrsim 200$,

consistent with previous iDMRG calculations [82].

The phase diagram for $\chi = 200$ and $L_y = 6$ is shown in Fig. 4.1b). In Fig. 4.1d) we show the CDW order parameter and the Hall conductivity along a cut at $t_2/t_1 = 0.1$, which show a discontinuity along the transition for all χs. These discontinuities are typical of a first-order phase transition, further supported by the saturation of the entanglement entropy at the transition as a function of correlation length. Comparing iDMRG results with the mean-field variational approach, our findings agree as long as the smallest band gap (relevant energy scale for CDW order) is located at the K-points (relevant for topology), which is the case for $t_2 \leq 0.2$, cf. Fig. 2.4. Therefore, we focus on this parameter regime.

4.2 Energetic analysis of the phase transition

We find at the mean field level a jump of the CDW order parameter ϕ^z at the phase transition for the choice of parameters regime. In Fig. 4.2 (top), we show the CDW order parameter as a function of V for different fixed values of t_2 ranging between $t_2 = 0.08$ and $t_2 = 0.20$. Here, the self-consistent mean field equations where solved for increasing V in small steps of $\Delta V = 0.0005$ in order to show clearly the jump in the order parameter ϕ^z. The jump becomes smaller the smaller t_2 is. Therefore, at the mean field level, a clear indication of a first order phase transition can only be given when t_2 is sufficiently large, i.e. at the order of $t_2 \sim 0.1$. From the Ginzburg-Landau and mean field theoretical point of view, a clear analysis of the nature of the mean field analysis for $t_2 < 0.05$ is not possible, the phase transition appears at most rather *weakly* first order when t_2 is close to zero. This observation seems to be in accordance with the literature [83], where a second order phase transition is predicted for vanishing t_2.

From our perspective, the regime of small t_2 seems therefore to be the middle ground between the clear indication of a first order phase transition in the range

$t_2 \in (0.08, 0.20)$ and the second order phase transition for vanishing t_2.

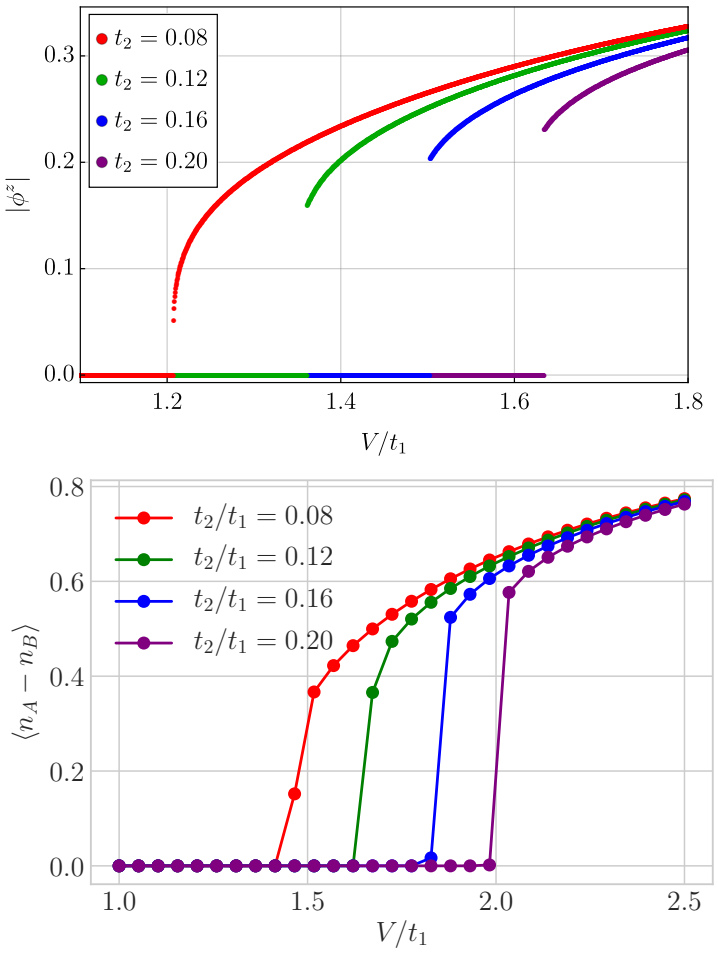

FIGURE 4.2: CDW order parameter from mean field theory (ϕ^z, top) and iDMRG ($L_y = 6$, $\chi = 200$, bottom) as a function of the interaction strength V/t for different values of the next-nearest neighbor hopping amplitude t_2. In both cases the smaller t_2 the smaller the jump in the order parameter (in agreement with known results in the literature for $t_2 = 0$ [83]). In the mean field diagram (left), we computed a solution to the self-consistent equations in small incremental steps of $\Delta V = 0.0005$ in order to show clearly the jump in the order parameter for the values of t_2 under investigation.

In order to confirm a first order transition on the mean field level for sufficiently large t_2, we evaluate the total free energy of system. Let $|\Omega_{\text{mf}}\rangle$ denote

the mean field ground state which in general depends on the self-consistently obtained field ϕ^r, i.e. $|\Omega_{\mathrm{mf}}\rangle \equiv |\Omega_{\mathrm{mf}}\rangle_{\boldsymbol{\phi}}$. Then, we compute the free energy of the system via $\mathcal{F}(\boldsymbol{\phi}) = \langle\Omega_{\mathrm{mf}}|\,\mathcal{H}\,|\Omega_{\mathrm{mf}}\rangle \equiv \langle\mathcal{H}\rangle$ where $\mathcal{H} = \mathcal{H}_0 + \mathcal{H}_V$ is the original Hamiltonian Eq. 4.2. This calculation involves exactly decomposing the quartic term $n_i n_j = c_i^\dagger c_i c_j^\dagger c_j$ using Wick's theorem [77] as

$$\langle c_i^\dagger c_i c_j^\dagger c_j\rangle = \langle c_i^\dagger c_i\rangle\langle c_j^\dagger c_j\rangle - \langle c_i^\dagger c_j^\dagger\rangle\langle c_i c_j\rangle - \langle c_i^\dagger c_j\rangle\langle c_j^\dagger c_i\rangle. \tag{4.36}$$

The amplitudes such as $\langle c_i^\dagger c_i\rangle$ are then evaluated similarly to the computation leading to Eq. 4.36.

Evaluating the energy in both phases around the transition shows that the energy curves cross at the transition line, see Fig. 4.3a) for $t_2 = 0.2$. This indicates a first order transition as the parameter will jump at the transition to the energetically preferable solution.

This can be further confirmed by computing the energy explicitly for small ϕ^z around the saddle-point solution right before the phase transition (also for $t_2 = 0.2$). The curve obtained, Fig. 4.3b), shows a typical *Mexican hat* form [77] with co-existing minima. We build a Ginzburg Landau theory, i.e. an expansion of the free energy curve. Finding appropriately relevant terms until the order $(\phi^z)^6$ is a difficult task here because V is large as well as ϕ^x, and therefore we perform this task numerically. The free energy can be approximated by a polynomial of the form

$$\mathcal{F}(\phi^z) = \mathcal{F}_0 + \alpha(\phi^z)^2 + \beta(\phi^z)^4 + \gamma(\phi^z)^6, \tag{4.37}$$

where the coefficients fulfill in general [84] $\alpha > 0$, $\beta < 0$, and $\gamma > 0$ to ensure the co-existence of local minima and that the free energy is bounded from below. We fit such a polynomial to the energy computed very close to the phase transition for different values of t_2. The results are shown in Table 4.1. In general, it is difficult to compare these coefficients for different values of t_2. For each value of

	$\mathcal{F}_0$	α	β	γ
$t_2 = 0.20$ and $V = 1.6250$	-2.0913	0.0402	-1.5045	15.6428
$t_2 = 0.08$ and $V = 1.2074$	-1.8445	0.0001	-0.2575	70.7487
$t_2 = 0.12$ and $V = 1.3610$	-1.8974	0.0010	-1.5419	31.4482
$t_2 = 0.14$ and $V = 1.4250$	-1.9232	0.0212	-1.2630	6.7646

TABLE 4.1: Ginzburg-Landau coefficients (of the polynomial Eq. 4.37). The coefficients for different values of t_2 are in general difficult to compare since we need for each t_2 to fix some V manually close to the phase transition, and the coefficients are subject to change in magnitude when only moving slightly towards the phase transition or away from it. Comparing signs is however possible, and the configuration at hand ($\alpha > 0$, $\beta < 0$, and $\gamma > 0$) determines a first order phase transition [84].

t_2 we need to fix a V that is close to the phase transition in order for Eq. 4.37 to be valid. Varying V in the vicinity of the phase transition slightly, i.e. moving either towards the phase transition or away from it, may change the magnitude of the coefficients in Table 4.1. However, we can make a statement on the signs of the coefficients. Since we get across all values of t_2 a consistent configuration of $\alpha > 0$, $\beta < 0$, and $\gamma > 0$, we can confirm the first order nature of the phase transition [84].

Furthermore, note that a plot of the energy landscape around a mean field solution such as Fig. 4.3b) is an important tool to check the validity of the mean field theory. If relevant mean field parameters are omitted, their weight is not correctly adjusted (the parameters η_r introduced above) in the self-consistent equations and the energy curve will not show a minimum.

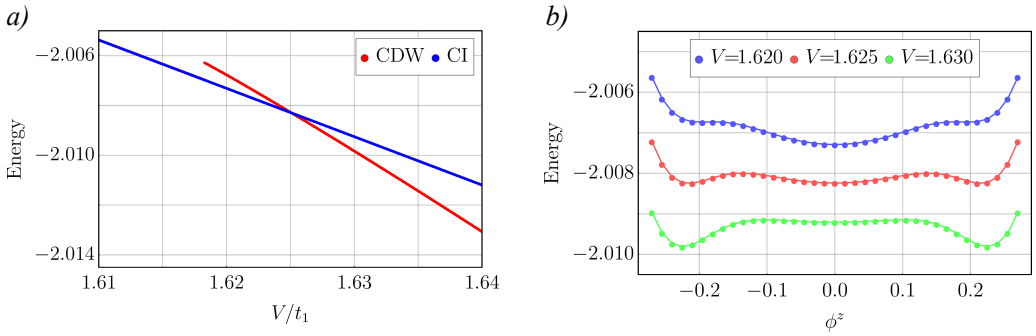

FIGURE 4.3: (a) Energy of the CI and CDW Mott phases obtained from mean field theory at $t_2 = 0.2$. The curves cut in one point, forcing the CDW order parameter to jump as the system abruptly prefers to change the phase in order to minimize energy. (b) Energy landscape around the mean field solution at $t_2 = 0.2$ as a function of the CDW order parameter ϕ^z at the phase transition. The coexistence of local minima indicates a first order transition according to Ginzburg-Landau theory.

4.3 Probing topology with light response

4.3.1 Circular dichroism of light at the Dirac points

In the theory chapter 2.3.5 we introduced the circular dichroism of light which had been suggested as a measure of the topological invariant of the Chern number [49, 50]. Shining light on a Chern insulator induces a population of the states in the upper band, above the band gap. The associated depletion rates and photocurrents [51] depend on the orientation of the circular drive. The Chern number is encoded in the difference of rates with opposite orientation.

Now, we address the formulation of the Chern number in terms of the light responses of the CI to circularly polarized light with different polarizations [49].

The topology in the Haldane honeycomb model is encoded in the high symmetry K and K′ points. As described in previous sections, the topology arises from the mass inversion at one of the two Dirac points.

The circular dichroism of light as introduced in Ref. [49] considers on the other hand the light response of the entire Brillouin zone to probe the topology

of an Chern insulator. In the case of the topological Haldane model, the natural question arises whether investigating the light response of the high symmetry K and K′ points is maybe already sufficient to probe the topology since the relevant information on mass inversion is encoded here.

In fact, it can be shown [26] that it suffices to consider the light response at the Dirac points K and K′ only in order to retrieve information of the topology in the Haldane honeycomb model. By expressing the transition amplitudes from the lower to the upper band in terms of eigenstates on the Bloch sphere, one can show [26] that the depletion rates $\Gamma^{\pm}_{l\to u}(\boldsymbol{k} = \boldsymbol{K}, \boldsymbol{K}')$ encode the mass term $|m| = 6\sqrt{3}t_2$ which determines the size of the band gap at the K-points.

Note that the next-nearest neighbor hopping term $t_2 e^{i\Phi}$ breaks time-reversal symmetry in the Haldane model, and therefore leads to different signs of m at the K and K′ points, and therefore, to non-trivial topology [14]. Numerically, we verify this observation by considering the depletion rate as derived in Ref. [49]

$$\Gamma^{\pm}_{l\to u}\left(\omega_{\boldsymbol{k}}, \boldsymbol{k}\right) = \frac{2\pi}{\hbar}\left(\frac{A_0}{\hbar\omega}\right)^2 |\mathcal{A}_{l\to u}|^2\, \delta\left(\epsilon^{\boldsymbol{k}}_u - \epsilon^{\boldsymbol{k}}_l - \hbar\omega\right) \tag{4.38}$$

and

$$\Gamma^{\pm}_{l\to u}\left(\omega_{\boldsymbol{k}}\right) = \sum_{\boldsymbol{k}\in \mathrm{BZ}} \Gamma^{\pm}_{l\to u}\left(\omega_{\boldsymbol{k}}, \boldsymbol{k}\right). \tag{4.39}$$

Here, the transition amplitude is given by

$$\mathcal{A}_{l\to u} = \langle u_{\boldsymbol{k}}| \frac{1}{i}\frac{\partial \mathcal{H}_0}{\partial k_x} \mp \frac{\partial \mathcal{H}_0}{\partial k_y} |l_{\boldsymbol{k}}\rangle, \tag{4.40}$$

where A_0 is a light-matter coupling constant with dimensionally equivalent to a vector potential in the original basis, $|u_{\boldsymbol{k}}\rangle$ and $|l_{\boldsymbol{k}}\rangle$ are the eigenstates corresponding to the lower and upper bands, $\epsilon^{\boldsymbol{k}}_{l,u}$ their eigenenergies, and the $\pm$ selects the polarization orientation. The sum on the momenta $\boldsymbol{k}$ involves the entire Brillouin zone.

The mass inversion occurring at one of the Dirac points is the source for the non-trivial topology in the Haldane model [14] and as it has been shown on the Bloch sphere [26], we can restrict ourselves to the Dirac K and K′ points, i.e. the substitution $\sum_{k\in \mathrm{BZ}} \to \sum_{k=K,K'}$. We verify numerically that we can evaluate the Chern number in the non-interacting Haldane model with the formula at the Dirac points only, and find for the frequency-integrated rates

$$\frac{1}{2}\int_0^\infty \mathrm{d}\omega \sum_{k=K,K'} \Gamma^+_{l\to u}(\omega_k, k) - \Gamma^-_{l\to u}(\omega_k, k) = \rho C \tag{4.41}$$

with the constant

$$\rho = 16\pi^3 A_0^2 \sqrt{3}\,|t_1|^2\, m^{-2}. \tag{4.42}$$

In the non-interacting case, the number C is one in the topological non-trivial phase of the Haldane model and exactly zero otherwise, and is thus the (ground state) Chern number.

4.3.2 Ground state circular dichroism

Using the light response of the entire Brillouin zone Eq. 4.38, we now compute the circular dichroism of light of the ground state of the effective mean field model of the interacting Haldane honeycomb model. In the mean field ground state, we find as expected that the topological Chern number is exactly one as in the CI phase and exactly zero in the CDW phase. However, when considering the light response of the Brillouin zone, we can still reveal differences in the depletion rate profiles for increasing interaction strength V, even though the Chern number does not change. Figs. 4.4 (a-c) visualize the results. 4.4 (a) and (b) show the ground state depletion in the TI phase (both have Chern number equal to one) for different interaction strengths V. In the TI phase, the CDW order parameter is zero. On the other hand however, the particle-hole channel ϕ^x is finite (cf. Fig. 4.1) and renormalizes thus for increasing V the function g in Eq. 4.22 which leads

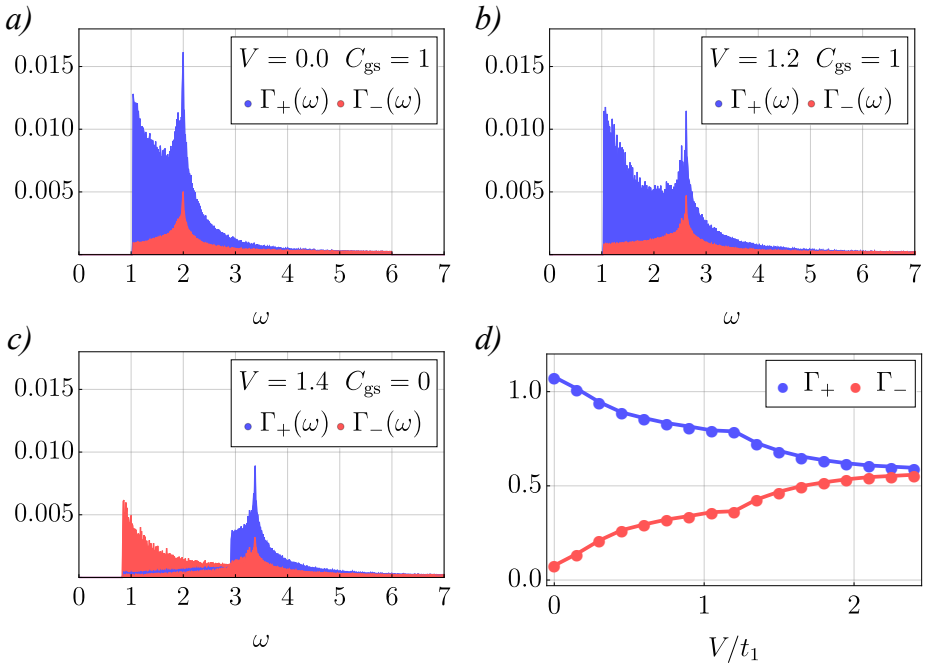

FIGURE 4.4: (a-c) Ground state depletion rate $\Gamma_\pm \equiv \sum_{k\in \mathrm{BZ}} \Gamma^\pm_{l\to u}(\omega_k, k)$ as a function of frequency for $t_2 = 0.1$ and different fixed values of the interaction strength V. (d) Stochastic frequency-integrated depletion rate $\Gamma_\pm \equiv \int \mathrm{d}\omega \sum_{k=K,K'} \Gamma^\pm_{l\to u}(\omega_k, k)$ at the Dirac points as a function of V.

to the difference in depletion rate profile in Eq. 4.4 (a) and (b). Finally, considering Fig. 4.4 (c), the sign flip of the mass term at one K-point at the CDW transition is reflected by regions of blue curve (Γ^+) turning red (Γ^-).

4.4 Stochastic Chern number

Here, we introduce the stochastic Chern number which accounts for the production of particle-hole pairs in the topological phase due to deviations of the stochastic variables from their ground state values, and more precisely, when sampling on the whole distribution of stochastic variables. First, we show that this formalism can e.g. describe randomness in the nearest-neighbors' interaction induced by a fluctuating staggered lattice potential and include the effect of an interacting environment [85, 86].

Then, we apply the methodology to study the light response and the Mott transition. We also show an analogy with temperature effects in the production of particle-hole pairs. This formalism then allows to classify different mechanisms creating particle-hole pairs due to interaction effects, regarding their topological response.

4.4.1 Stochastic Topological Number and Interpretation as a Disordered Situation

Here, we show that the sampling on the stochastic variable ϕ^z can be equally understood as a sampling on the interaction strength V. These arguments below then show that the stochastic topological number corresponds to situations with a slightly disordered interaction strength. Since we also have $n_A n_B = \hat{\phi}_0^2 - \hat{\phi}_z^2$, we deduce that fluctuations in the interaction V between nearest-neighbour sites can be produced either by a fluctuating mean-density or a fluctuating staggered potential on the lattice corresponding to a Semenoff mass with zero mean and a Gaussian distribution.

We define the stochastic topological number as

$$C = \int_{-\infty}^{+\infty} d\phi P(\phi) C(\phi), \tag{4.43}$$

with $\phi = \phi^z$ and the Gaussian distribution

$$P(\phi) = \frac{1}{\sqrt{2\pi\xi(V)}} e^{-\frac{1}{2}(\phi-\phi_{\mathrm{mf}})^2 \xi^{-1}(V)}, \tag{4.44}$$

with $\xi(V) = 1/(12V)$.

Since C can be equally measured through the pseudo-spin magnetizations $\langle \sigma^z \rangle$ at the poles [26], this is equivalent in this calculation of C as if $\phi^x = \phi^y = 0$ since $g(\mathbf{k}) = 0$ at the poles in the Hamiltonian h_V of Eq. 4.15. For a given value of

V, we can insert the precise value of ϕ_{mf} obtained from the variational mean-field approach with simply $\phi_{\text{mf}} = 0$ in the topological phase.

From statistical physics arguments, then we have

$$\langle \sigma^z(\phi) \rangle = \frac{1}{\mathcal{Z}} \text{Tr} \left(e^{-\beta h_V} \sigma^z \right), \tag{4.45}$$

assuming θ values equal to 0 and π. Therefore, Eq. 4.43 is then equivalent to define the ensembled-averaged variable

$$\langle \sigma^z \rangle = \int_{-\infty}^{+\infty} d\phi P(\phi) \langle \sigma^z(\phi) \rangle. \tag{4.46}$$

Now, h_V is symmetric under the variables ϕ and V. Therefore, we equivalently have

$$\langle \sigma^z \rangle = \int_{-\infty}^{+\infty} d\tilde{v} P(\tilde{v}) \langle \sigma^z(\tilde{v}) \rangle, \tag{4.47}$$

with

$$P(\tilde{v}) = \frac{1}{\sqrt{2\pi\xi(V)}} e^{-\frac{1}{2}\tilde{v}^2 \xi^{-1}(V)} \tag{4.48}$$

where $\tilde{v} = (\tilde{V} - V)/V = \phi - \phi^z_{\text{mf}}$ measures deviations from the mean value V for the interaction strength between sublattices A and B. Including fluctuations, the diagonal term in $\mathcal{H}_{\text{mf}}$ in Eq. 4.20 now involves $3V\tilde{v} + 3V\phi^z_{\text{mf}}$ showing the relation with a fluctuating staggered potential equal to $3V\tilde{v}$. From the formulation of C as a current density we infer that the stochastic topological number can be measured through the quantum Hall conductivity and the circular dichroism of light corresponding e.g. to an average on different samples.

Eq. 4.43 is therefore useful to describe lattice effects or the effect of an interacting environment. As the term $3V\phi^z$ plays the role of a Semenoff mass term acting on the Haldane model in Eq. 4.21, we can also define - for a given V - ϕ^z_c such that $3V|\phi^z_c| = 3\sqrt{3}t_2$. Then, all states with $|\phi^z| < |\phi^z_c|$ produce a Chern number $C(\phi) = 1$ to C_{st} while all other $|\phi^z|$ contribute zero.

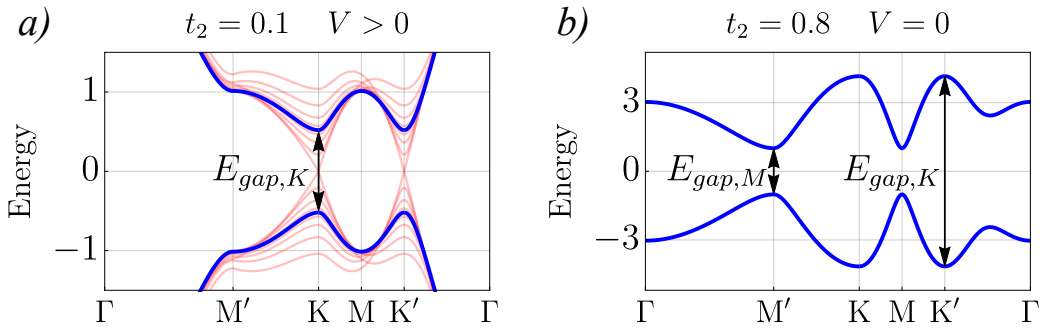

FIGURE 4.5: (a) Band structure (blue pair of bands) for small $t_2 < 0.2$ with $t_1 = 1$. The low energy physics is centered around the Dirac points, where the stochastic approach applies. If we allow for fluctuations at $V > 0$, the sampling of ϕ^z corresponds to the creation of quasi states that change the band gap at the K and K′ points. (b) Haldane band structure for large $t_2 > 0.2$ such that the low energy regime is located at the M-points.

When V approaches (energetically) the order of the the smallest band gap around the K-points in Fig. 2.4a), particle-hole pairs will start to form and this leads to the formation of a mixed state. The stochastic topological number is equivalent to

$$C_{st} = 1 - 2\int_{|\phi_c^z|}^{+\infty} d\phi P(\phi). \tag{4.49}$$

The integral goes to zero when $V \to 0$ corresponding to a pure (ground-)state, justifying that in this case $C_{st} = C_{gs} = 1$. For small interactions, C can be approximated as

$$C_{st} = 1 - 2\int_{|\phi_c^z|}^{+\infty} d\phi P(\phi)\delta(\phi \sim |\phi_c^z|) \approx 1 - 2P(\phi \sim |\phi_c^z|), \tag{4.50}$$

keeping the dominant term in the series development of the erfc-function. Therefore, this leads to

$$C_{st} - 1 \propto e^{-m^2/(k_B T_{eff})^2} \tag{4.51}$$

with $k_B T_{eff} \propto \sqrt{V}$. This argument then shows that deviations from unity of the topological number come from the creation of particle-hole pairs. This implies

that fluctuations in the interaction strength or fluctuations in the charge environment on the lattice is equivalent to produce a finite probability to reach the upper band. In this sense, the definition of the stochastic Chern number can describe the effect of interaction-induced particle-hole pairs in the topological phase. We also observe that $\tilde{V}$ plays a similar role as a Landau-Zener mechanism on the sphere [87]. In this sense, the stochastic Chern number may find various applications.

The parameter $k_B T_{eff}$ above leads to an analogy with temperature effects that we study below in Sec. 4.4.4.

4.4.2 Light-Matter Response and Mott Transition

To evaluate the light response in a mixed state, we consider Eq. 4.41, substitute $\mathcal{H}_0 \to \mathcal{H}^{\rm mf}$ and here sample all the stochastic variables with a distribution $P(\phi^r)$ according to Eq. 4.44. Importantly, ϕ^z acts as Semenoff mass term on the Haldane model modifying the band gap at the Dirac points. Sampling ϕ^z around the saddle point solution generates excited states with smaller energy band gaps, see the light red bands in Fig. 4.5a). We sample the fields $(\phi^x, \phi^y, \phi^z) = \boldsymbol{\phi}$ according to $P(\phi^r)$ while keeping the chemical potential constant at half-filling, i.e. $\phi^0 = -1/2$. In Fig. 4.4d), we show the evolution of the ensemble-averaged rates Γ_+ and Γ_- as a function of V, when sampling on the variables $\boldsymbol{\phi}$. These variables are now hidden in the eigenenergies in Eq. 4.38.

For each configuration we can also associate a $\boldsymbol{\phi}$-dependent Chern number $C(\boldsymbol{\phi})$ via Eq. 4.41 that will be either one or zero. Then, for completeness, we evaluate

$$C_{\rm st} \equiv \int_{-\infty}^{+\infty} {\rm d}\boldsymbol{\phi} P(\boldsymbol{\phi}) C(\boldsymbol{\phi}), \tag{4.52}$$

which can take non-integer values when it refers to a mixed state. Computing $C_{\rm st}$ for 10^5 random configurations, as a function of V, then we obtain the result in red in Fig. 4.6a), which can be compared to the ground state Chern number

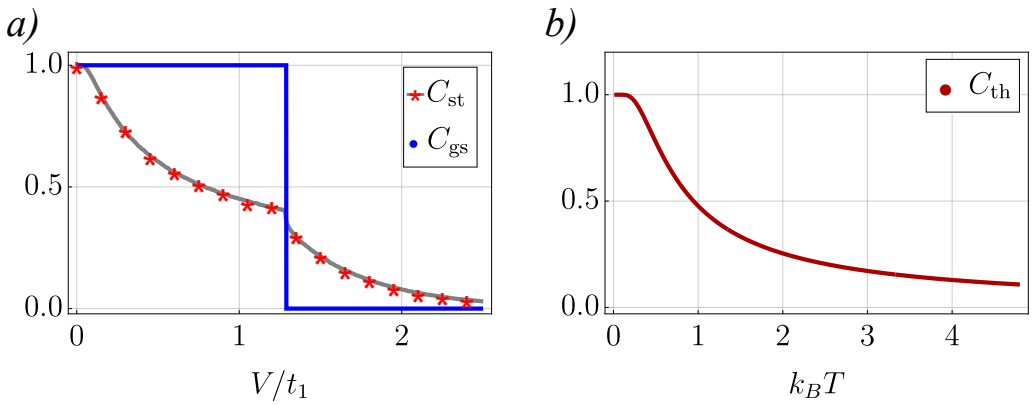

FIGURE 4.6: (a) Evaluation of the ground state Chern number C_{gs} and stochastic Chern number C_{st} as a function of V. The grey curve comes from the analytical formula in Eq. (4.50). (b) C_{th} from Eq. (4.54) at $V = 0$ as a function of k_BT.

C_{gs} in blue obtained when $\phi^z = \phi^z_{\mathrm{mf}}$. The quantity C_{gs} determines the quantum Hall conductivity, in agreement with iDMRG (see Fig. 4.1d)) and with the Bloch sphere arguments.

Hence, we can also write C_{st} via Eq. 4.50, which results in the grey curve in Fig. 4.6a). This highlights the correspondence between the ensemble-averaged values of $\Gamma_+ - \Gamma_-$ in Fig. 4.4d), and C_{st} as a function of V. It's interesting to observe that C_{st} still reveals the first-order Mott transition through a small jump in Fig. 4.6a).

4.4.3 Energy distribution of excited quasi particles

Finally, we would like to comment on the stochastic approach to the interacting Chern insulator from the energetic point of view. Allowing the mean field parameters ϕ^r to fluctuate around the saddle point solution changes the energy of the quasi state under consideration. We sample the fields $\phi^{x,y,z}$ and for each configuration we can compute the energy of this quasi state with respect to the wave function

$$|\Omega\rangle \equiv |\Omega(\phi^x, \phi^y, \phi^z)\rangle\,. \tag{4.53}$$

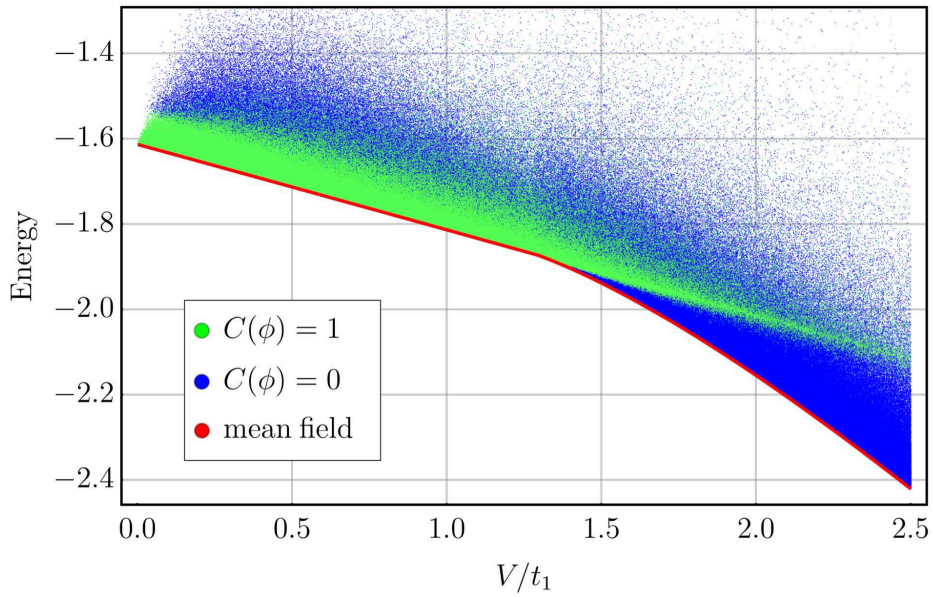

FIGURE 4.7: Energy of the mean field ground state as function of V (red line). Also shown is the energy distribution of quasi states obtained from sampling $(\phi^x, \phi^y, \phi^z) = \boldsymbol{\phi}$ around the saddle point. This creates quasi-excited states at energies higher than the mean field ground state. Each quasi-state can be attributed a Chern number $C(\boldsymbol{\phi})$ which will be either one (green) or zero (blue).

Repeating this procedure for 10^3 sampled configurations of the $\phi^{x,y,z}$ for each respective V yields Fig. 4.7. The red line gives the energy of the mean field ground state which is the lowest energy state for each V. Sampling the ϕ^p fields will result in a quasi state at a higher energy. Each quasi state can be associated with a Chern number of either one or zero (depending on ϕ^z).

For small V, the mean field ground state (red line) as well as states close to it have Chern number one. Close to the phase transition, it then becomes more likely to create a state with Chern number zero when moving away from the saddle point. At the phase transition, the ground state acquires Chern number 0 and for further increasing V it becomes more and more unlikely to create an

excited state with non-trivial topology. This analysis also shows the occurrence of a jump in the topological Chern number at the phase transition, from the ground state, as obtained with iDMRG in Fig. 4.1d).

4.4.4 Analogy with Temperature Effects

Here, we also formulate an analogy with the finite-temperature version of the Hall conductivity [88] and introduce a finite-temperature version of Eq. 4.41

$$\frac{1}{2}\int_0^\infty \mathrm{d}\omega \sum_{\alpha,\boldsymbol{k}} \left(p^{\boldsymbol{k}} \Gamma_\alpha^+ \left(\omega_{\boldsymbol{k}}, \boldsymbol{k}\right) - p^{\boldsymbol{k}} \Gamma_\alpha^- \left(\omega_{\boldsymbol{k}}, \boldsymbol{k}\right) \right) = \rho C_{\mathrm{th}} \tag{4.54}$$

where

$$p^{\boldsymbol{k}} = (1 + \exp(\epsilon_{u,l}^{\boldsymbol{k}} / k_B T))^{-1} \tag{4.55}$$

is the Fermi distribution, k_B is the Boltzmann constant, and the variable α here refers to $\{l \to u, u \to l\}$ such that $p^{\boldsymbol{k}}$ effectively mixes the states of the lower and upper band. We then allow in Eq. 4.54 for heating of the bulk to contribute to C_{th} [88]. From Eq. 4.54, we find that at low temperatures ($k_B T \ll m$), the finite-temperature Chern number C_{th} decreases smoothly as

$$1 - e^{-m/k_B T} \tag{4.56}$$

in Fig. 4.6.

In the presence of interactions, we observe an analogy with heating in the sense that the probability to create a particle-hole pair in the topological phase will be dominated by values of $|\phi^z| \sim |\phi_c^z|$, producing a reduction of C_{st} evolving as

$$P(|\phi^z| \sim |\phi_c^z|) \propto e^{-m^2/(k_B T_{eff})^2} \tag{4.57}$$

from Eq. 4.20, with an effective temperature such that $k_B T_{eff} \propto \sqrt{V}$ in Fig. 4.6.

We also observe a similar behavior of C in the presence of band-crossing effects on the Bloch sphere [87], which then suggests various possible further applications of this formalism.

Chapter 5

Analytical approach to the Kane-Mele-Hubbard model

In the previous sections, we learned that Haldane [14] proposed a model that realizes the IQHE without an external magnetic field. We reviewed how Haldane outlined how to explicitly break time-reversal symmetry in order to induce non-trivial topology in the bulk of graphene. While Haldane published his seminal paper in 1988, his ideas gained traction almost twenty years later when Kane and Mele [73, 89] and independently Zhang and Bernevig [90] described the *Quantum Spin Hall Effect* (QSHE). The QSHE is realized [73] by two copies of a Haldane model, where the Peierls phases Φ are chosen to be π and $-\pi$, respectively. Hence, (the lower band of) one copy carries a Chern $+1$, while the other one carries a Chern number of -1, cf. Fig. 2.3. The interpretation is that each copy corresponds to a spin-$\frac{1}{2}$ particle with opposing chirality, i.e. a $\uparrow$-particle with positive chirality (Chern number $+1$) and a $\downarrow$-particle with negative chirality (Chern number -1). Thus, in contrast to the Haldane model, the Kane-Mele model features counter-propagating, spin-filtered *helical* edge modes and most importantly, *does not* break time reversal symmetry.

Crucially, we note that the total Chern of the Kane-Mele vanishes, i.e. $1 - 1 = 0$. This hints that the Chern number is indeed not a suitable quantity in order to

classify the Kane-Mele model topologically. In fact, the helical nature of the edge modes in the Kane-Mele model points to a $\mathbb{Z}_2$ topological invariant which we will introduce in this section. Therefore, the Kane-Mele is the prototypical model of the so-called $\mathbb{Z}_2$ topological insulator.

5.1 The Kane-Mele model

5.1.1 Model Hamiltonian

Mathematically, the Kane-Mele model [73, 89, 47, 11, 31] can be written in real space as

$$\mathcal{H}_{KM} = -t_1 \sum_{\langle i,j \rangle} \sum_{\alpha} c^{\dagger}_{i\alpha} c_{j\alpha} - it_2 \sum_{\langle\langle i,j \rangle\rangle} \sum_{\alpha,\beta} \nu_{ij} c^{\dagger}_{i\alpha} \sigma^{z}_{\alpha\beta} c_{j\beta} \tag{5.1}$$

Here, $c^{\dagger}_{i\alpha}$ and $c_{i\alpha}$ denote regular fermionic creation and annihilation operators, respectively. t_1 and t_2 are the amplitudes of the nearest-neighbor and next-nearest neighbor hopping, respectively. That means that $\langle i,j \rangle$ denotes nearest neighbor lattice sites while $\langle\langle i,j \rangle\rangle$ denotes next-nearest neighbors. Furthermore, the coefficient ν_{ij} changes sign, i.e. $\nu_{ij} = \pm 1$ depending on whether going from i to j means moving clockwise or counter-clockwise around the plaquette. Moreover, σ^z denotes the third of the Pauli matrices that span spin space of the spin components $\alpha, \beta \in \{\uparrow, \downarrow\}$. Finally, note that we here present a version of the Kane-Mele model that does not consider Rashba spin-orbit coupling, [11].

We switch from real to momentum space by using the Fourier transform

$$c_{i\alpha} = \frac{2}{N_{\text{cells}}} \sum_{\boldsymbol{k}} e^{i\boldsymbol{k}\boldsymbol{R}_i} c_{\boldsymbol{k}\alpha} \tag{5.2}$$

where N_{cells} is the number of unit cells and $\boldsymbol{R}_i$ the lattice vector of lattice site i. In momentum space, the Kane-Mele Hamiltonian Eq. 5.1 can then be conveniently

written as $\mathcal{H}_{KM} = \sum_{\boldsymbol{k}} \Psi_{\boldsymbol{k}}^\dagger \mathcal{H}_{KM,\boldsymbol{k}} \Psi_{\boldsymbol{k}}$ where the spinor basis is defined as

$$\Psi_{\boldsymbol{k}}^\dagger = \left(c_{\boldsymbol{k}A\uparrow}^\dagger, c_{\boldsymbol{k}B\uparrow}^\dagger, c_{\boldsymbol{k}A\downarrow}^\dagger, c_{\boldsymbol{k}B\downarrow}^\dagger \right). \tag{5.3}$$

In analogy to the way we wrote the Hamiltonian density of the Haldane honeycomb model in momentum space, refer to Eq. 2.46, the Kane-Mele Hamiltonian density can be written as [47]

$$\mathcal{H}_{KM,\boldsymbol{k}} = \begin{pmatrix} \gamma(\boldsymbol{k}) & -g(\boldsymbol{k}) & & \\ -g^*(\boldsymbol{k}) & -\gamma(\boldsymbol{k}) & & \\ & & -\gamma(\boldsymbol{k}) & -g(\boldsymbol{k}) \\ & & -g^*(\boldsymbol{k}) & \gamma(\boldsymbol{k}) \end{pmatrix}. \tag{5.4}$$

The functions γ and g where defined in Eq. 2.32 and 2.47.

In Eq. 5.4, the upper left block matrix describes a Haldane honeycomb model with Chern number $+1$ as in Eq. 2.46, whereas the lower right block matrix describes a Haldane honeycomb model with Chern number -1. Each copy of a Haldane honeycomb model is attached to a spin flavor $\uparrow$ or $\downarrow$, as we can see from the definition of the spinor basis Eq. 5.3. Hence, armed with the knowledge of the Haldane honeycomb model, we can write Eq. 5.4 simply as

$$\mathcal{H}_{KM,\boldsymbol{k}} = \begin{pmatrix} \mathcal{H}_{h,\uparrow}(\boldsymbol{k}) & \\ & \mathcal{H}_{h,\downarrow}(\boldsymbol{k}) \end{pmatrix}. \tag{5.5}$$

The bulk band structures of the Kane-Mele model will therefore resemble the band structures of the Haldane model, cf. Fig. 2.4, only that each band is now doubly degenerate.

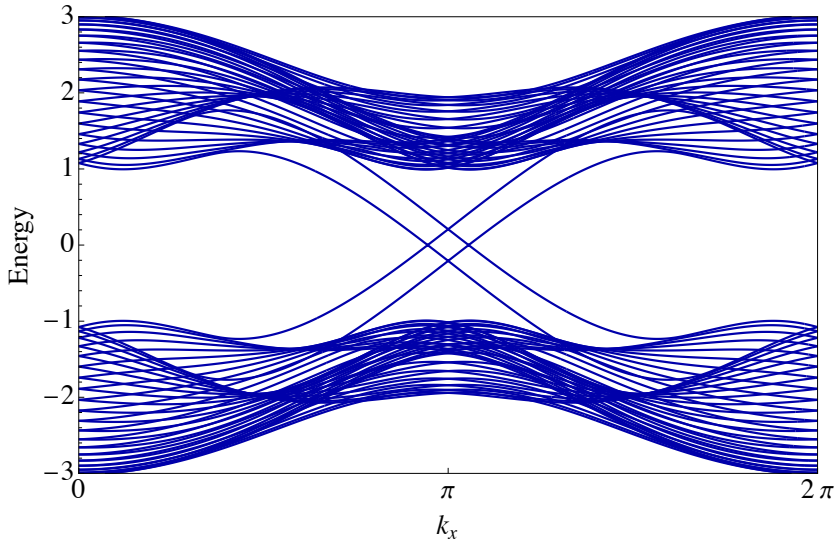

FIGURE 5.1: Edge spectrum of the Kane-Mele model for $t_1 = 1$, $t_2 = 1/3$, and $\Phi = \pi/2$. Here, a Semenoff mass term $M = 0.2\sqrt{3}$ has been imposed to make the degenerate, counter-propagating helical modes visible. Bulk bands are gapped, only the counter-propagating, helical modes located at the two edges are gapless.

5.1.2 The $\mathbb{Z}_2$ topological invariant

We already noted that the total Chern number in the Kane-Mele model is zero. However, since the Chern number of each band is non-zero, it makes sense to define a new topological quantity which takes this fact into account. Hence, we define the *spin Chern number* $C_{\uparrow\downarrow}$ as [71]

$$C_{\uparrow\downarrow} = (C_{\uparrow} - C_{\downarrow})/2 \tag{5.6}$$

where $C_{\uparrow/\downarrow}$ refers to the Chern number of the lower band of $\mathcal{H}_{h,\uparrow/\downarrow}$. This quantity is robust [71] since we noted that the Kane-Mele Hamiltonian can be decomposed into two independent parts corresponding to the two spin components $\uparrow$ and $\downarrow$.

Another way to quantify the topology in the time reversal symmetric topological insulator was introduced by Kane and Mele [73, 89] who made use of the Pfaffian invariant in order to define a $\mathbb{Z}_2$ invariant. While several formulations of

the $\mathbb{Z}_2$ invariant exist, here, we follow Fu and Kane [69].

To this end, we introduce the notation as introduced in Ref. [69, 47], i.e. we rewrite the Hamiltonian density Eq. 5.4 as

$$\mathcal{H}_{KM,\boldsymbol{k}} = \sum_{i=1}^{5} d_i(\boldsymbol{k})\Gamma^i. \tag{5.7}$$

Here, we introduced the coefficients d_i in Eq. 5.7 can be identified in the following way [69, 47]. d_1 and d_2 correspond to the real and imaginary part of the function g, cf. Eq. 4.22, d_5 corresponds to the function γ, cf. Eq. 4.21, and finally, d_3 and d_4 are zero here (in the absence of Rashba term [73, 89, 69].

Furthermore, we introduced the gamma matrices Γ^i which are defined as

$$\Gamma^1 = \tau^x \otimes I \tag{5.8}$$

$$\Gamma^2 = \tau^y \otimes I \tag{5.9}$$

$$\Gamma^3 = \tau^z \otimes \sigma^x \tag{5.10}$$

$$\Gamma^4 = \tau^z \otimes \sigma^y \tag{5.11}$$

$$\Gamma^5 = \tau^z \otimes \sigma^z. \tag{5.12}$$

where I refers to the 2×2 identity matrix, τ to the Pauli matrices in sublattice space and σ the Pauli matrices in spin space. As we saw already, the Kane-Mele Hamiltonian can be written as a 4×4 matrix. In other words, it can be written as the sum of an identity matrix and 15 generators of the SU(4) group [11]. The Γ^i are 5 of these 15 generators, which form a Clifford or Dirac algebra [11], i.e.

$$\{\Gamma^i, \Gamma^j\} = 2\delta_{ij}, \tag{5.13}$$

where $\{\cdot,\cdot\}$ is the anticommutator. The other 10 generators are formed by the commutators [69, 11, 47]

$$\Gamma^{ij} = \frac{1}{2i}\left[\Gamma^i, \Gamma^j\right]. \tag{5.14}$$

Now, we introduce the time reversal operator $\mathcal{T}$ [69] as

$$\mathcal{T} = i(I \otimes \sigma^y)\mathcal{K} \tag{5.15}$$

where $\mathcal{K}$ refers to the complex conjugation operator. And furthermore, we introduce the parity operator $\mathcal{P}$ as [47]

$$\mathcal{P} = \tau^x \times I = \Gamma^1. \tag{5.16}$$

We note that the Gamma matrices above are invariant under time reversal parity $\mathcal{PT}$, i.e. [47]

$$(\mathcal{PT})\Gamma^i(\mathcal{PT})^{-1} = \Gamma^i. \tag{5.17}$$

Hence, $\mathcal{PT}$ commutes with the Hamiltonian [47, 69].

Now, we consider some special points [69] $\boldsymbol{k} = \xi_i$, $i = 1, \ldots, 4$, which are the only time reversal points in the Brillouin zone. Time reversal points need to fulfil $\xi_i = \frac{1}{2}(n_1\nu_1 + n_2\nu_2)$ where ν are the reciprocal lattice vectors, cf. Eq. 2.1 and $n_i \in \{0, 1\}$. This can be seen [69] from the fact that these points need to fulfil $-\xi_i = \xi_i + \boldsymbol{G}$ where G is a reciprocal lattice such that a corresponding wave function is periodic in the Brillouin zone, i.e. $|\Psi_{\boldsymbol{k}}\rangle = |\Psi_{\boldsymbol{k}+\boldsymbol{G}}\rangle$.

Refering to Fig. 2.1, the points ξ_i correspond to the high symmetry points Γ, M and M'. Then, the $\mathbb{Z}_2$ invariant $z = 0, 1$ which is either zero for a conventional insulator and one for a topological insulator can then be defined [69, 47] as

$$(-1)^z = \prod_{i=1}^{4} \delta(\xi_i) \tag{5.18}$$

where

$$\delta(\xi_i) = -\mathrm{sgn}(d_1(\Gamma_i)). \tag{5.19}$$

In particular, one finds for the Kane-Mele model [47] that $\delta(\xi_{1,2,3}) = -1$ (for $t_1 = 1$) and $\delta(\xi_4) = 1$ such that

$$z = 1. \tag{5.20}$$

Hence, the Kane-Mele model is a $\mathbb{Z}_2$ topological insulator since z does not vanish and the bulk band spectrum is gapped throughout the Brillouin zone.

5.2 The Kane-Mele-Hubbard model

The Kane-Mele model is as a prototypical model exactly solvable within a tight-binding approach as presented above. When electron-electron interactions are added to the model, and the topological band insulator is challenged by correlation physics, this is not anymore the case. The Kane-Mele-Hubbard model has been extensively studied [31, 47, 70, 91, 92, 93, 94, 95, 96, 97, 98, 99, 100, 101, 102, 103] with various approximative methods in the past decade, and its behavior is in principle well understood.

The Kane-Mele-Hubbard model reads

$$\mathcal{H}_{\mathrm{KMH}} = \mathcal{H}_0 + \mathcal{H}_U \qquad \mathcal{H}_U = U \sum_i n_{i\uparrow} n_{i\downarrow} \tag{5.21}$$

where $\mathcal{H}_0$ is the Kane-Mele Hamiltonian Eq. 5.1 and $\mathcal{H}_U$ is the repulsive Hubbard on-site interaction with the interaction strength $U > 0$ that acts on spin space. A solution of this model comprises two phases. First, up to some critical interaction strength [31] $U_c \gtrapprox t_1$ the topological band insulator is stable towards electron-electron interactions. Upon reaching the critical U_c, the system transitions to a magnetically ordered phase (spin density wave). In this phase, the system prefers to antiferromagnetically order in the $x - y$ plane only. This behavior has been

previously explained by the derivation of an effective Hamiltonian in the strong coupling limit [47, 31]

$$\mathcal{H}_{eff} = \frac{4t_1^2}{\mathcal{U}} \sum_{\langle i,j \rangle} \boldsymbol{S}_i \boldsymbol{S}_j + \frac{4t_2^2}{\mathcal{U}} \sum_{\langle\langle i,j \rangle\rangle} \left(-S_i^x S_j^x - S_i^y S_j^y + S_i^z S_j^z \right). \tag{5.22}$$

Due to the bipartite nature of the honeycomb lattice, the Heisenberg model (the first part of the above equation concerning interacting nearest neighbor spins), exhibits Néel order in the ground state [31]. Therefore, the next-nearest neighbor terms in the z-plane compete with the nearest neighbor terms. Hence, the system chooses to solve this frustration by ordering in the $x - y$ plane [31, 47] so that the z-interaction is neutralized.

This result has been pointed out [31] to be in good agreement with several numeric studies [70, 96, 97, 103, 99, 104].

5.3 The Kane-Mele-Hubbard model from a variational principle

Here, we follow an approach similar to the one we used to treat the interacting Haldane model in the previous chapter. This variational mean field approach will describe the correct decomposition scheme of the Kane-Mele-Hubbard model by all relevant physical channels, including those that were missing in previous studies [47].

We present a new analytical approach to the Kane-Mele-Hubbard model in chapter 5.4 that builds directly on the decomposition scheme outlined in this section.

5.3.1 Kane-Mele-Hamiltonian decoupling scheme

In order to prepare the decoupling of the quartic interaction term, we can write $\mathcal{H}_U$ exactly as

$$U\sum_i n_{i\uparrow}n_{i\downarrow} = U\sum_i c^\dagger_{i\uparrow}c_{i\uparrow}c^\dagger_{i\downarrow}c_{i\downarrow} \tag{5.23}$$

$$= U\sum_{i,r}\eta_r\left(c^\dagger_{i\alpha}\sigma^r_{\alpha\beta}c_{i\beta}\right)^2 \tag{5.24}$$

where i denotes a lattice site, $r \in \{0,x,y,z\}$, and σ^r denotes the Pauli matrices acting on spin space spanned by $\{\uparrow,\downarrow\}$ The coefficients η_r need to fulfill the relations

$$\eta_0 = -\eta_z \qquad f\eta_x = \eta_y \qquad \frac{1}{4} = \eta_0 - \eta_x. \tag{5.25}$$

By means of a variational approach to the construction of the mean field theory which we will outline below, we find that the following choice of the coefficients η_r.

$$-\eta_0 = \eta_x = \eta_y = \eta_z = -\frac{1}{8}. \tag{5.26}$$

5.3.2 Hubbard-Stratonovich transformations

Now, we turn to the decoupling of the decomposed quartic terms and write down the partition function and action

$$\mathcal{Z} = \int \mathrm{D}(\Psi,\Psi^\dagger)e^{-\mathcal{S}} \tag{5.27}$$

$$\mathcal{S} = \int_0^\beta \mathrm{d}\tau\sum_{\boldsymbol{k}}\Psi^\dagger_{\boldsymbol{k}}\left(\partial_\tau + \mathcal{H}_{0,\boldsymbol{k}}(\boldsymbol{k})\right)\Psi_{\boldsymbol{k}} + \mathcal{H}_U \tag{5.28}$$

where we defined the spinor basis $\Psi^\dagger_{\boldsymbol{k}}$ in Eq. (5.3) and the Hamiltonian density of the Kane-Mele model in momentum space in Eq. (5.4).

Decoupling the quartic interaction term $\mathcal{H}_U$ via a Hubbard-Stratonovich [77] transformation for each $r \in \{x, y, z\}$ yields

$$\exp\left(\frac{U}{8}\sum_i \left(c_{i\alpha}^\dagger \sigma_{\alpha\beta}^r c_{i\beta}\right)^2\right) \tag{5.29}$$

$$= \int \mathrm{D}\phi^r \exp\left(-\sum_i 2U(\phi_i^r)^2 + U\phi_i^r\left(c_{i\alpha}^\dagger \sigma_{\alpha\beta}^r c_{i\beta}\right)\right), \tag{5.30}$$

and for $r = 0$

$$\exp\left(-\frac{U}{8}\sum_i \left(c_{i\alpha}^\dagger \sigma_{\alpha\beta}^0 c_{i\beta}\right)^2\right) \tag{5.31}$$

$$= \int \mathrm{D}\phi^0 \exp\left(-\sum_i 2U(\phi_i^0)^2 + iU\phi_i^0\left(c_{i\alpha}^\dagger \sigma_{\alpha\beta}^0 c_{i\beta}\right)\right). \tag{5.32}$$

Here we introduced for each r an auxiliary field ϕ_i^r on each lattice site i. Effectively, we traded a quartic interaction for the introduction of additional order parameters ϕ_i^r that will need to be solved for self-consistently.

5.3.3 Interaction density matrix

Now, we consider the auxiliary fields ϕ^r to be homogeneous on the lattice, i.e. we suppress the index lattice index i. Then, we rewrite the decoupled interaction part in Fourier space and obtain the partition function

$$\mathcal{Z} = \int \mathrm{D}(\Psi, \Psi^\dagger, \phi^0, \phi^x, \phi^y, \phi^z) e^{-\mathcal{S}} \tag{5.33}$$

where the action $\mathcal{S}$ reads

$$\mathcal{S} = \int_0^\beta \mathrm{d}\tau \sum_{\boldsymbol{k}} \Psi_{\boldsymbol{k}}^\dagger \left(\partial_\tau + \mathcal{H}_{0,\boldsymbol{k}}\right) \Psi_{\boldsymbol{k}} + \sum_{\boldsymbol{k},\boldsymbol{q},p} \Psi_{\boldsymbol{q}}^\dagger \mathcal{H}_{U,\boldsymbol{k},\boldsymbol{q},p} \Psi_{\boldsymbol{k}} + \sum_{\boldsymbol{k},r} 2U\phi_{\boldsymbol{k}}^r \phi_{-\boldsymbol{k}}^r \tag{5.34}$$

where the interaction density matrix reads

$$\mathcal{H}_{U,\boldsymbol{k},\boldsymbol{q},p} = U \begin{pmatrix} i\phi^0_{\boldsymbol{k}-\boldsymbol{q}} + \phi^z_{\boldsymbol{k}-\boldsymbol{q}} & & \phi^x_{\boldsymbol{k}-\boldsymbol{q}} - i\phi^y_{\boldsymbol{k}-\boldsymbol{q}} & \\ & i\phi^0_{\boldsymbol{k}-\boldsymbol{q}} + \phi^z_{\boldsymbol{k}-\boldsymbol{q}} & & \phi^x_{\boldsymbol{k}-\boldsymbol{q}} - i\phi^y_{\boldsymbol{k}-\boldsymbol{q}} \\ \phi^x_{\boldsymbol{k}+\boldsymbol{q}} + i\phi^y_{\boldsymbol{k}-\boldsymbol{q}} & & i\phi^0_{\boldsymbol{k}-\boldsymbol{q}} - \phi^z_{\boldsymbol{k}-\boldsymbol{q}} & \\ & \phi^x_{\boldsymbol{k}-\boldsymbol{q}} + i\phi^y_{\boldsymbol{k}-\boldsymbol{q}} & & i\phi^0_{\boldsymbol{k}-\boldsymbol{q}} - \phi^z_{\boldsymbol{k}-\boldsymbol{q}} \end{pmatrix}. \tag{5.35}$$

We would like to consider a time-independent, static model and therefore restrict the analysis to the zero frequency contribution. Furthermore, we restrict the discussion to leading contribution in momentum space for which scattering does not change momentum. Hence, we keep only the zero momentum contribution, i.e. $\boldsymbol{k} - \boldsymbol{q} = 0$. The action $\mathcal{S}$ now takes the form

$$\mathcal{S} = \sum_{\boldsymbol{k}} \Psi^\dagger_{\boldsymbol{k}} \left(\mathcal{H}_{0,\boldsymbol{k}} + \mathcal{H}_{U,\boldsymbol{k},p} \right) \Psi_{\boldsymbol{k}} + \sum_{\boldsymbol{k},r} 2U\phi^r_{\boldsymbol{k}}\phi^r_{-\boldsymbol{k}}, \tag{5.36}$$

where the interaction density matrix now reads

$$\mathcal{H}_{U,\boldsymbol{k},p} = \begin{pmatrix} \phi^0 + \phi^z & & \phi^x - i\phi^y & \\ & \phi^0 + \phi^z & & \phi^x - i\phi^y \\ \phi^x + i\phi^y & & \phi^0 - \phi^z & \\ & \phi^x + i\phi^y & & \phi^0 - \phi^z \end{pmatrix} \tag{5.37}$$

Here we skipped the zero-momentum index of the fields, i.e. $\phi^r \equiv \phi^r_0$, and redefined the chemical potential $-i\phi^0 \to \phi^0$ such that ϕ^0 is now real for the matrix $\mathcal{H}_{U,\boldsymbol{k},p}$ to be Hermitian (where it was imaginary before the substitution, such that $i\phi^0$ was real).

We set

$$\mathcal{H}^{\mathrm{mf}}_{\mathrm{KMH},\boldsymbol{k}} = \mathcal{H}_{0,\boldsymbol{k}} + \mathcal{H}_{U,\boldsymbol{k},p}, \tag{5.38}$$

and finally arrive at the effective mean field Hamiltonian

$$\mathcal{H}^{\mathrm{mf}}_{\mathrm{KMH}} = \sum_{\boldsymbol{k}} \Psi^{\dagger}_{\boldsymbol{k}} \mathcal{H}^{\mathrm{mf}}_{\mathrm{KMH},\boldsymbol{k}} \Psi_{\boldsymbol{k}}. \tag{5.39}$$

where the mean field Hamiltonian density in matrix form explicitly reads

$$\mathcal{H}^{\mathrm{mf}}_{\mathrm{KMH},\boldsymbol{k}} = \mathcal{H}_{KM,\boldsymbol{k}} + \begin{pmatrix} U(\phi^0_A + \phi^z_A) & & U(\phi^x_A - i\phi^y_A) & \\ & U(\phi^0_B + \phi^z_B) & & U(\phi^x_B - i\phi^y_B) \\ U(\phi^x_A + i\phi^y_A) & & U(\phi^0_A - \phi^z_A) & \\ & U(\phi^x_B + i\phi^y_B) & & U(\phi^0_B - \phi^z_B) \end{pmatrix}. \tag{5.40}$$

Here, $\mathcal{H}_{KM,\boldsymbol{k}}$ is the Kane-Mele model Hamiltonian density in momentum space, Eq. 5.4. Furthermore, in Eq. 5.40 we distinguished ϕ^r by the sublattice $s \in \{A, B\}$ they are living on.

Having set up the mean field Hamiltonian, we now turn the derivation of the fields ϕ^r in a self-consistent manner.

5.3.4 Self-consistent mean field equations

We minimize the total energy $\langle \mathcal{H}_{\mathrm{KMH}} \rangle$ of the system (before the decoupling) Eq. 5.21 with respect to the wave function of the mean field Hamiltonian Eq. 5.39. This way, the mean field energy of the mean field Hamiltonian Eq. 5.39 equates the total energy, i.e. $\langle \mathcal{H}^{\mathrm{mf}}_{\mathrm{KMH}} \rangle = \langle \mathcal{H}_{\mathrm{KMH}} \rangle$. We find the following self-consistent

equations for $r \in \{0, x, y, z\}$

$$\phi^0 = -\frac{1}{2}\left(\left\langle c^\dagger_{i\uparrow} c_{i\uparrow}\right\rangle + \left\langle c^\dagger_{i\downarrow} c_{i\downarrow}\right\rangle\right) \tag{5.41}$$

$$\phi^x = -\frac{1}{2}\left(\left\langle c^\dagger_{i\downarrow} c_{i\uparrow}\right\rangle + \left\langle c^\dagger_{i\uparrow} c_{i\downarrow}\right\rangle\right) \tag{5.42}$$

$$\phi^y = -\frac{1}{2}\left(-i\left\langle c^\dagger_{i\downarrow} c_{i\uparrow}\right\rangle + i\left\langle c^\dagger_{i\uparrow} c_{i\downarrow}\right\rangle\right) \tag{5.43}$$

$$\phi^z = -\frac{1}{2}\left(\left\langle c^\dagger_{i\uparrow} c_{i\uparrow}\right\rangle - \left\langle c^\dagger_{i\downarrow} c_{i\downarrow}\right\rangle\right) \tag{5.44}$$

or in shorthand notation

$$\phi^r = -\frac{1}{2}\left\langle c^\dagger_{i\alpha} \sigma^r_{\alpha\beta} c_\beta\right\rangle . \tag{5.45}$$

Here, ϕ^0 is a chemical potential, and $\phi^{x,y,z}$ are magnetic order parameters. The amplitudes of the form $\langle c^\dagger_{i\alpha} c_{i\beta}\rangle$ are computed in the following manner [105].

We introduce the matrix $\mathcal{U}$ that diagonalizes the matrix $\mathcal{H}^{\mathrm{mf}}_{\mathrm{KMH},\boldsymbol{k}}$ for a fixed set of parameters ϕ^r and fixed $\boldsymbol{k}$ as

$$\Psi^\dagger_{\boldsymbol{k}} \mathcal{H}^{\mathrm{mf}}_{\mathrm{KMH},\boldsymbol{k}} \Psi_{\boldsymbol{k}} = \Psi^\dagger_{\boldsymbol{k}} \mathcal{U}_{\boldsymbol{k}} \mathcal{U}^\dagger_{\boldsymbol{k}} \mathcal{H}^{\mathrm{mf}}_{\mathrm{KMH},\boldsymbol{k}} \mathcal{U}_{\boldsymbol{k}} \mathcal{U}^\dagger_{\boldsymbol{k}} \Psi_{\boldsymbol{k}} \tag{5.46}$$

$$= \Omega^\dagger_{\boldsymbol{k}} \tilde{\mathcal{H}}^{\mathrm{mf}}_{\mathrm{KMH},\boldsymbol{k}} \Omega_{\boldsymbol{k}} \tag{5.47}$$

where $\mathcal{U}_{\boldsymbol{k}}$ is an appropriate unitary matrix. The new spinor basis is defined as $\Omega_{\boldsymbol{k}} \equiv \mathcal{U}^\dagger_{\boldsymbol{k}} \Psi_{\boldsymbol{k}}$, and the diagonal matrix as $\tilde{\mathcal{H}}^{\mathrm{mf}}_{\mathrm{KMH},\boldsymbol{k}} \equiv \mathcal{U}^\dagger_{\boldsymbol{k}} \mathcal{H}^{\mathrm{mf}}_{\mathrm{KMH},\boldsymbol{k}} \mathcal{U}_{\boldsymbol{k}}$.
Now we compute the amplitudes in Eq. (5.41-5.44) as

$$\left\langle c^\dagger_{i\alpha} c_{i\beta}\right\rangle = \frac{2}{N_{\mathrm{sites}}} \sum_{\boldsymbol{k}} \left\langle c^\dagger_{\boldsymbol{k}\alpha} c_{\boldsymbol{k}\beta}\right\rangle \tag{5.48}$$

$$= \frac{2}{N_{\mathrm{sites}}} \sum_{\boldsymbol{k}} \sum_{\mu',\nu'} \mathcal{U}^*_{\boldsymbol{k}\mu\mu'} \mathcal{U}_{\boldsymbol{k}\nu\nu'} \left\langle \Omega^\dagger_{\boldsymbol{k}\mu'} \Omega_{\boldsymbol{k}\nu'}\right\rangle \tag{5.49}$$

$$= \frac{2}{N_{\mathrm{sites}}} \sum_{\boldsymbol{k},\lambda} \mathcal{U}^*_{\boldsymbol{k}\mu\lambda} \mathcal{U}_{\boldsymbol{k}\nu\lambda} \tag{5.50}$$

In the first line, we carried out a Fourier transform. The composite indices μ and ν

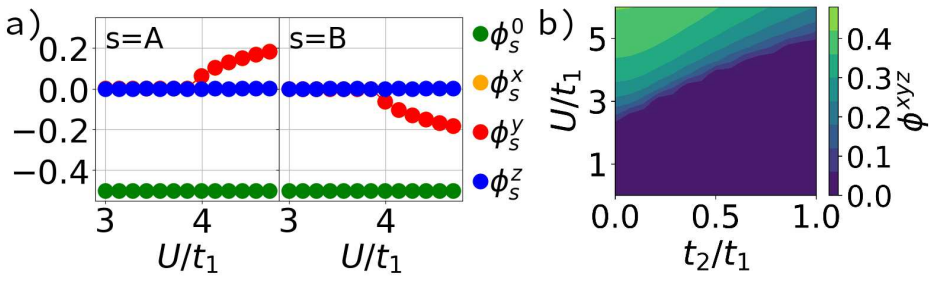

FIGURE 5.2: (a) Honeycomb lattice with sublattices A (red) and B (blue). The vectors $u_{x,y}$ are the lattice vectors and the vectors $a_{x,y,z}$ ($b_{x,y,z}$) denote the (next) nearest neighbor displacements. (b) Brioullin zone of the honeycomb lattice in momentum space. We denote the reciprocal lattice vectors by $\nu_{x,y}$ and show high symmetry points.

correspond to $i\alpha$ and $i\beta$, respectively. Furthermore, the indices μ' and ν' run over all eigenvectors, while λ in the last line only runs over occupied states. Finally, $N_{\text{sites}} = 2N_{\text{cells}}$ is the number of lattice sites.

We now solve the self-consistent mean field equations Eq. (5.41-5.44) for a given set of initial values for the fields ϕ^r by iteration. In each step, a new set of ϕ^r is computed from the previous set by computing the amplitudes $\langle c_{i\alpha}^\dagger c_{i\beta} \rangle$. This procedure is repeated until sufficient convergence is reached.

5.3.5 Solution to the self-consistent mean field equations

Fig. 5.2 shows the solution of the self-consistent mean field equations. Fig 5.2 (a) shows the evolution of the mean field parameters for fixed $t_2 = 0.5$. At the phase transition, the magnetic order parameters condense, i.e. $\phi^x = \phi^y \neq 0$ in the Mott phase. Furthermore, they change sign depending on the sublattice ($s = A$ or $s = B$) which indicates an antiferromagnetic behavior. Hence, the topological insulator transitions to a antiferromagnetic with net magnetization in the $x - y$ plane.

Finally, Fig. 5.2 (b) shows a two-dimensional $U - t_2$ phase diagram. Here, the quantity $\phi^{xyz} = \sqrt{(\phi^x)^2 + (\phi^y)^2 + (\phi^z)^2}$ captures the net magnetization. The

position of the transition line is in overall good accordance with previous results [31].

5.4 Analytical approach to the Kane-Mele-Hubbard model

In this section, we follow closely Ref. [27]. We show a new analytical approach to the Kane-Mele-Hubbard model, that was presented in Ref. [27]. This approach directly builds on the decomposition scheme described in the previous section.

5.4.1 Decomposition and Hubbard-Stratonovich transformation

We start off, by reminding ourselves of the important Eq. 5.52 in combination with the side constraints on the coefficients η_r in Eq. 5.25. In Here, we choose to write Eq. 5.52 as

$$U\sum_i n_{i\uparrow}n_{i\downarrow} = U\sum_i c^\dagger_{i\uparrow}c_{i\uparrow}c^\dagger_{i\downarrow}c_{i\downarrow} \tag{5.51}$$

$$= U\sum_{i,r}\eta_r S^r_i S^r_i \tag{5.52}$$

where we set $S^r_i \equiv c^\dagger_{i\alpha}\sigma^r_{\alpha\beta}c_{i\beta}$. Then, we use the symmetric decomposition corresponding to the choice of the Eq. 5.26, i.e. $\eta_0 = 1/8$, $\eta_{x,y,z} = -1/8$ and choose to write the interaction Hamiltonian $\mathcal{H}_\mathcal{U}$ as [27]

$$\mathcal{H}_U = \frac{U}{8}\sum_i \langle \boldsymbol{S}_i, \boldsymbol{S}_i\rangle_\mathcal{M} + \frac{U}{4}\sum_i (n_{i\uparrow}+n_{i\downarrow}), \tag{5.53}$$

where we used the Minkowski inner product $\langle \boldsymbol{S}_i, \boldsymbol{S}_i\rangle_\mathcal{M} = (S^0_i)^2 - (S^x_i)^2 - (S^y_i)^2 - (S^z_i)^2$.

Analogously to the previous section, we now perform a Hubbard-Stratonovich transformation in order to decouple the quartic interaction terms. We start with

the action [27]

$$\mathcal{S}[\psi^\dagger,\psi] = \mathcal{S}_0[\psi^\dagger,\psi] + \int_0^\beta d\tau \frac{U}{8}\sum_i \langle \boldsymbol{S}_i, \boldsymbol{S}_i\rangle_{\mathcal{M}}, \tag{5.54}$$

where $S_0[\psi^\dagger,\psi]$ is the action for the non-interacting Kane-Mele model (including the chemical potential shift $\frac{U}{4}$ from Eq. 5.53.

We perform the Hubbard-Stratonovich transformation [76, 77] by introducing Gaussian auxiliary bosonic fields ϕ_i^r corresponding to each S_i^r channel and renormalize by the constant determinant. The resulting path integral is [27]

$$\mathcal{Z} = \int \Pi_r \mathrm{D}\phi^r \int \mathrm{D}\psi^\dagger \mathrm{D}\psi \exp\Big(- \mathcal{S}[\psi^\dagger,\psi] - 2U\int_0^\beta \mathrm{d}\tau \sum_{i,r}\phi_i^r\phi_i^r\Big), \tag{5.55}$$

where Π_r refers to the product on $r = 0, x, y, z$.

Now, we use the linear transformations of the bosonic fields [27]

$$\phi_i^0 \to \frac{i}{2}\phi_i^0 + \frac{i}{4}S_i^0, \qquad \phi_i^p \to \frac{1}{2}\phi_i^p + \frac{1}{4}S_i^p \tag{5.56}$$

where $p \in x, y, z$. We then compensate the interaction term in $-\mathcal{S}[\psi^\dagger,\psi]$ such that

$$\begin{aligned}\mathcal{Z} = \frac{i}{16}\int \Pi_r \mathrm{D}\phi^r \int \mathrm{D}\psi^\dagger \mathrm{D}\psi \exp\Big(&- \mathcal{S}_0[\psi^\dagger,\psi] \\ &+ \frac{U}{2}\int_0^\beta \mathrm{d}\tau \sum_i (\langle \boldsymbol{\phi}_i, \boldsymbol{\phi}_i\rangle_{\mathcal{M}} + \langle \boldsymbol{\phi}_i, \boldsymbol{S}_i\rangle_{\mathcal{M}})\Big),\end{aligned} \tag{5.57}$$

where we have defined the four-vector $\boldsymbol{\phi}_i \equiv (\phi_i^0, \phi_i^x, \phi_i^y, \phi_i^z)$ and used the Minkowski inner product again.

In the previous section, we derived the self-consistent mean field equations by minimizing the total energy of the system (i.e. the energy derived from the Hamiltonian before decoupling it into the various channels ϕ^r) with respect to the wave function of the mean field Hamiltonian. This way, the total energy of the equates the mean field energy, i.e. $\langle \mathcal{H}^{\mathrm{mf}}_{\mathrm{KMH}}\rangle = \langle \mathcal{H}_{\mathrm{KMH}}\rangle$.

Here, we rather obtain the classical field equations from minimization of the mean field Hamiltonian with respect to the various parameters ϕ^r, i.e.

$$\frac{\delta \mathcal{S}}{\delta \phi_i^r} = 0. \tag{5.58}$$

This way, we find that analogously to the previous section

$$\boldsymbol{\phi}_i = -\frac{1}{2}\langle \boldsymbol{S}_i \rangle = -\frac{1}{2}\langle c_{i\alpha}^\dagger \boldsymbol{\sigma}_{\alpha\beta} c_{i\beta} \rangle. \tag{5.59}$$

In Ref. [27], in order to obtain an insulator, we fix the particle density at half-filling such that $\phi^0 = -1/2$. The stochastic fields are static variables allowing us to evaluate the electron Green's function and energetics for a given fields configuration and then to apply the variational principle to find the most favorable distribution of those variables [27].

Similarly to the previous section (cf. Eq. 5.40), we find the following mean field Hamiltonian

$$\mathcal{H}_{\mathrm{MF}}(\boldsymbol{k}) = \begin{pmatrix} \gamma(\boldsymbol{k}) + \frac{U}{2}\phi_A^z & -g(\boldsymbol{k}) & \frac{U}{2}(\phi_A^x + i\phi_A^y) & 0 \\ -g^*(\boldsymbol{k}) & -\gamma(\boldsymbol{k}) + \frac{U}{2}\phi_B^z & 0 & \frac{U}{2}(\phi_B^x + i\phi_B^y) \\ \frac{U}{2}(\phi_A^x - i\phi_A^y) & 0 & -\gamma(\boldsymbol{k}) - \frac{U}{2}\phi_A^z & -g(\boldsymbol{k}) \\ 0 & \frac{U}{2}(\phi_B^x - i\phi_B^y) & -g^*(\boldsymbol{k}) & \gamma(\boldsymbol{k}) - \frac{U}{2}\phi_B^z \end{pmatrix}. \tag{5.60}$$

with the corresponding action [27]

$$\mathcal{S} = \int^\beta \mathrm{d}\tau \left[\sum_{\boldsymbol{k}} \psi_{\boldsymbol{k}}^\dagger \left(\partial_\tau + \frac{U}{2} + \mathcal{H}_{\mathrm{MF}}(\boldsymbol{k}) \right) \psi_{\boldsymbol{k}} - \frac{U}{2} \sum_{\boldsymbol{k},s} \langle \boldsymbol{\phi}_{\boldsymbol{k}s}, \boldsymbol{\phi}_{-\boldsymbol{k}s} \rangle_{\mathcal{M}} \right]. \tag{5.61}$$

Here, the functions γ and g are as previously defined in Eq. 2.47 and 2.32.

5.4.2 Transition line from saddle point conditions

Then, we transform the action into frequency space so that $\boldsymbol{\phi}_{n\boldsymbol{k}s} = \beta\delta_{i\omega_n,0}\boldsymbol{\phi}_{\boldsymbol{k}s}$ or equivalently $\phi^r_{n\boldsymbol{k}s} = \beta\delta_{i\omega_n,0}\phi^r_{\boldsymbol{k}s}$, where ω_n are fermionic Matsubara frequencies and $\boldsymbol{\phi}_{\boldsymbol{k}s}$ is independent of frequency and time [27]

$$\psi(\tau) = \frac{1}{\beta}\sum_{i\omega_n}\psi_n e^{-i\omega_n\tau}. \tag{5.62}$$

Next, we follow Ref. [27] and integrate out the fermions to get a determinant

$$\begin{aligned}\mathcal{Z} =& \frac{i}{16}\int \Pi_{r,\boldsymbol{k},s}\mathrm{d}\phi^r_{\boldsymbol{k}s}\,\det(-\beta\mathcal{G}^{-1}(i\omega_n)) \\ &\times\exp\left(\frac{\beta U}{2}\sum_{\boldsymbol{k},s}(\boldsymbol{\phi}_{\boldsymbol{k}s}\cdot\boldsymbol{\phi}_{-\boldsymbol{k}s})\right),\end{aligned} \tag{5.63}$$

where the inverse fermion Green's function is

$$\mathcal{G}^{-1}_{\boldsymbol{q}\boldsymbol{k}}(i\omega_n) = \left(i\omega_n - \frac{U}{2} - \mathcal{H}_{\mathrm{MF}}(\boldsymbol{k})\right)\delta_{\boldsymbol{q},\boldsymbol{k}}. \tag{5.64}$$

Thus, we have the effective Hubbard-Stratonovich action [27]

$$\mathcal{S}_{\mathrm{HS}} = -\beta U\sum_{\boldsymbol{k}}(\boldsymbol{\phi}_{\boldsymbol{k}}\cdot\boldsymbol{\phi}_{-\boldsymbol{k}}) - \mathrm{tr}(\ln(-\beta\mathcal{G}^{-1}(i\omega_n))), \tag{5.65}$$

where tr denotes the trace over Matsubara frequencies, momentum space, spin space and pseudospin space.

Following our previous results, Fig. 5.2, we impose the following assumptions concerning the mean field parameters ϕ^r

$$\phi^{x,y,z}_{\boldsymbol{k}A} = -\phi^{x,y,z}_{\boldsymbol{k}B} \equiv \phi^{x,y,z}_{\boldsymbol{k}} \tag{5.66}$$

We vary the Hubbard-Stratonovich action with respect to the HS fields to get the saddle-point conditions [27]

$$\frac{\delta \mathcal{S}_{\mathrm{HS}}}{\delta \phi^r_{\boldsymbol{p}}} = \pm\, 2\beta U \phi^r_{-\boldsymbol{p}} - \mathrm{tr}\left[\mathcal{G}(i\omega_n)\frac{\delta \mathcal{G}^{-1}(i\omega_n)}{\delta \phi^r_{\boldsymbol{p}}}\right], \tag{5.67}$$

Here, the positive sign holds for $r \in \{x, y, z\}$ and the negative sign holds for $r = 0$. In particular, we have [27]

$$\frac{\delta \mathcal{S}_{\mathrm{HS}}}{\delta \phi^0_0} = -2\beta\sqrt{N}U\phi^0 - \frac{U}{2\sqrt{N}}\sum_{i\omega_n,\boldsymbol{k}} \mathrm{tr}(\mathcal{G}(i\omega_n,\boldsymbol{k})), \tag{5.68}$$

$$\frac{\delta \mathcal{S}_{\mathrm{HS}}}{\delta \phi^r_0} = 2\beta\sqrt{N}U\phi^r + \frac{U}{2\sqrt{N}}\sum_{i\omega_n,\boldsymbol{k}} \mathrm{tr}\Big(\mathcal{G}(i\omega_n,\boldsymbol{k})(\sigma^r \otimes \tau^z)\Big),. \tag{5.69}$$

where N is the number of unit cells (not to be confused with N_{sites}, the number of lattice sites that we introduced earlier). Note that τ refers to the Pauli matrices in sublattice space, while σ refers to the Pauli matrices in spin space as usual.

In Ref. [27], we evaluated the Matsubara Green's function as

$$\mathcal{G}(i\omega_n, \underline{\mathrm{k}}) = \frac{(i\omega_n - \frac{U}{2})\mathbb{I} + \mathcal{H}_{\mathrm{MF}}(\underline{\mathrm{k}})}{(i\omega_n - E_{\underline{\mathrm{k}}+})(i\omega_n - E_{\underline{\mathrm{k}}-})}, \tag{5.70}$$

where the poles of the Green's function are the quasi-particle energies

$$E_{\boldsymbol{k}\pm} = \frac{U}{2} \pm \sqrt{\epsilon^2_{\boldsymbol{k}} + 2\gamma_{\boldsymbol{k}}\left(\frac{U}{2}\right)\phi^z + \left(\frac{U}{2}\right)^2 \boldsymbol{\phi}\cdot\boldsymbol{\phi}}. \tag{5.71}$$

Here, we can see that the chemical potential is effectively shifted by $\frac{U}{2}$.

The traces in Eq. (5.68), (5.69) are readily evaluated [27]. At zero temperature, the saddle-point conditions $\frac{\delta \mathcal{S}_{\mathrm{HS}}}{\delta \phi^r} = 0$ then yield [27]

$$\phi^{x,y} = \frac{U\phi^{x,y}}{4N}\sum_{\boldsymbol{k}} \frac{1}{\sqrt{\epsilon^2_{\boldsymbol{k}} + 2\gamma_{\boldsymbol{k}}(\frac{U}{2})\phi^z + (\frac{U}{2})^2\boldsymbol{\phi}\cdot\boldsymbol{\phi}}}. \tag{5.72}$$

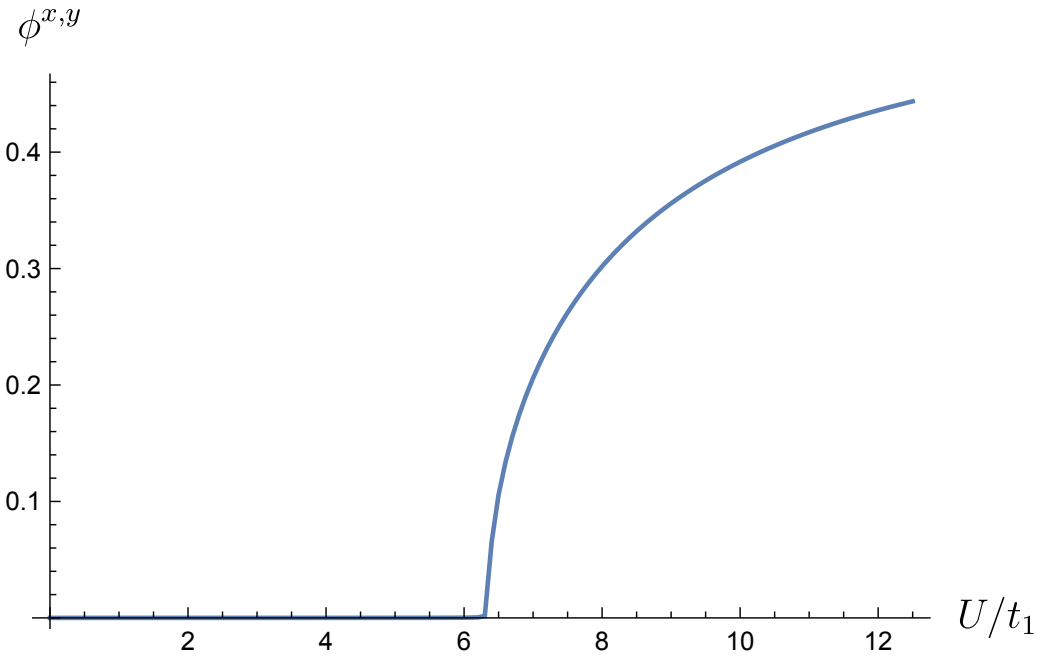

FIGURE 5.3: Magnetization profile for $t_2 = 0.3t_1$. Figure extracted from Ref. [27]

There is a second-order transition in this magnetic order parameter as shown in Fig. 5.3. Linearizing $\boldsymbol{\phi}$ around the zero vector, one finds the critical coupling

$$\frac{1}{U_c^{x,y}} = \frac{1}{4N}\sum_{\boldsymbol{k}}\frac{1}{\epsilon_{\boldsymbol{k}}}, \tag{5.73}$$

as shown in Fig. 5.4. This result shows remarkable quantitative agreement with quantum Monte Carlo and cluster dynamical mean field theory for small t_2 [97, 70, 106].

Then, as pointed out in Ref. [27], the saddle-point condition for ϕ^z is

$$\phi^z = \frac{1}{2N}\sum_{\boldsymbol{k}}\frac{\gamma_{\boldsymbol{k}} + \frac{U}{2}\phi^z}{\sqrt{\epsilon_{\boldsymbol{k}}^2 + 2\gamma_{\boldsymbol{k}}(\frac{U}{2})\phi^z + (\frac{U}{2})^2\boldsymbol{\phi}\cdot\boldsymbol{\phi}}}. \tag{5.74}$$

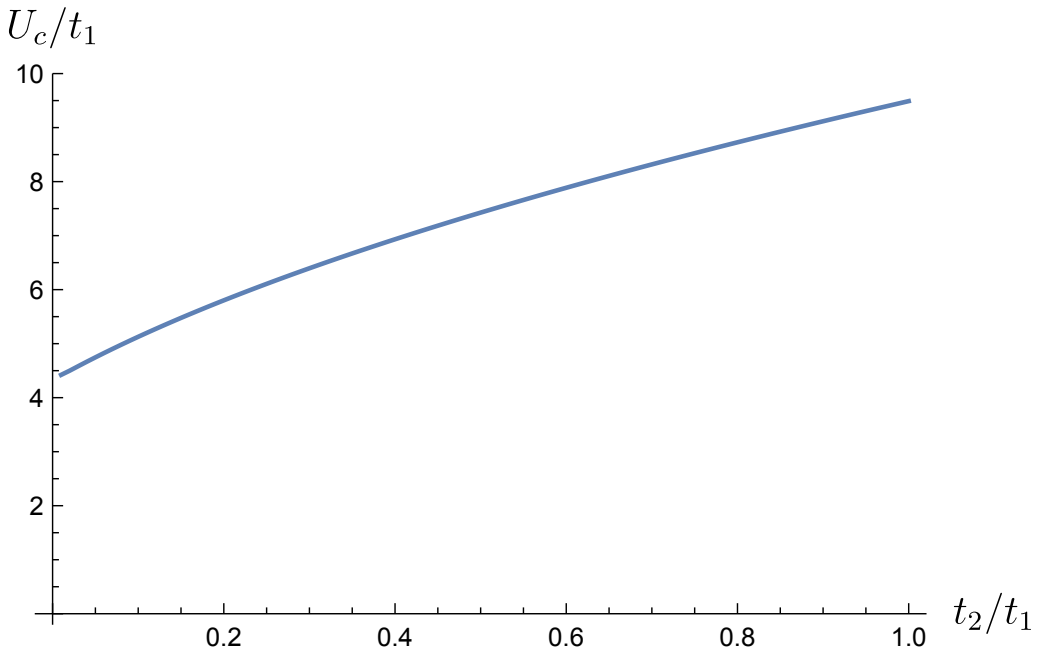

FIGURE 5.4: Onset of antiferromagnetic XY order at the Mott transition line defined through U_c in Eq. 5.72 versus t_2/t_1. Figure extracted from Ref. [27]

Linearizing $\boldsymbol{\phi}$ about the zero vector, and noting that γ_k is odd under inversion also gives the critical coupling [27]

$$\frac{1}{U_c^z} = \frac{1}{4N}\sum_k \frac{|g_k|^2}{\epsilon_k^3}. \tag{5.75}$$

Since $|g_k|^2 < \epsilon_k^2$ for all $t_2 > 0$, we see that $U_c^{x,y} < U_c^z$ except at $t_2 = 0$ at which point the transition lines are identical and the full SU(2) symmetry is restored. Thus as we approach from the normal state, the spins will first order antiferromagnetically in the $x-y$ plane. In fact, we can go a step further. For $t_2 > 0$, it turns out that ϕ^z must vanish for any U. We can see this by combining Eq. 5.72 and 5.74 to get [27]

$$\phi^z = \phi^z + \frac{1}{2N}\sum_k \frac{\gamma_k}{\sqrt{\epsilon_k^2 + 2\gamma_k(\frac{U}{2})\phi^z + (\frac{U}{2})^2\boldsymbol{\phi}\cdot\boldsymbol{\phi}}}. \tag{5.76}$$

In order for the sum to vanish at finite t_2, the denominator must be invariant under inversion. This only happens for $\phi^z = 0$, so we confirm that the ordering strictly takes place in the plane for all U, in agreement with quantum Monte Carlo and strong-coupling results [97, 47]. As long as $\phi^z = 0$, then we verify from Eq. 5.71 that the gap does not close at the phase transition, but is uniformly renormalized by $(U/2)^2 \boldsymbol{\phi} \cdot \boldsymbol{\phi}$.

5.5 Conclusion and comparison of the two methods

First, in chapter 5.3, we derived a variational decomposition scheme for the on-site Hubbard interaction acting on the Kane-Mele model. We then derived self-consistent mean field equations from a variational principle in which we minimize the mean field wave function with respect to the *original* (i.e. non-decoupled) Hamiltonian. Finally, we solved the self-conistent mean field equations numerically to find the Mott transition line in Fig. 5.2.

Secondly, in chapter 5.4, we followed Ref. [27] and explored an alternative approach to find the Mott transition line. Here, we started off with the same decomposition scheme as developed in chapter 5.3. Most notably, this method yields a closed form equation for the Mott transition line, Eq. 5.73.

However, we notice that the transition lines in Fig. 5.2 and 5.4 are not the same. In fact, they differ by a factor of two. This difference can be explained by a different choice of mean field in the methods.

As we explain in Ref. [27], the choice in chapter 5.4 corresponds to a Heisenberg-like mean field that preserves the SU(2) symmetry of the interaction. We write the interaction as a "spin" Hamiltonian, where the spin vectors $\boldsymbol{S}_i = c^\dagger_{i\alpha} \boldsymbol{\sigma}_{\alpha\beta} c_{i\beta}$ form

the natural mean fields

$$\begin{aligned}\mathcal{H}_U &= \frac{U}{8}\sum_i \langle \boldsymbol{S}_i, \boldsymbol{S}_i\rangle_{\mathcal{M}} + \frac{U}{4}\sum_i (n_{i\uparrow}+n_{i\downarrow}) \\ &\approx \frac{U}{8}\sum_i \Big(\langle\langle \boldsymbol{S}_i\rangle, \boldsymbol{S}_i\rangle_{\mathcal{M}} + \langle \boldsymbol{S}_i, \langle \boldsymbol{S}_i\rangle\rangle_{\mathcal{M}} - \langle\langle \boldsymbol{S}_i\rangle, \langle \boldsymbol{S}_i\rangle\rangle_{\mathcal{M}} + 2S_i^0 \Big).\end{aligned} \tag{5.77}$$

Recalling that $\langle \boldsymbol{S}_i\rangle = -2\boldsymbol{\phi}_i$, we have [27]

$$\mathcal{H}_U \approx -\frac{U}{2}\sum_i \langle \boldsymbol{\phi}_i, \boldsymbol{S}_i\rangle_{\mathcal{M}} - \frac{U}{2}\sum_i \langle \boldsymbol{\phi}_i, \boldsymbol{\phi}_i\rangle_{\mathcal{M}} + \frac{U}{4}\sum_i S_i^0. \tag{5.79}$$

Fourier transforming gives [27]

$$\mathcal{H}_U \approx \sum_{\boldsymbol{k}} \psi_{\boldsymbol{k}}^\dagger \frac{U}{2}\mathcal{H}_{\text{int}}\psi_{\boldsymbol{k}} - \frac{UN}{2}(\langle \boldsymbol{\phi}_A, \boldsymbol{\phi}_A\rangle_{\mathcal{M}} + \langle \boldsymbol{\phi}_B, \boldsymbol{\phi}_B\rangle_{\mathcal{M}}), \tag{5.80}$$

where

$$\mathcal{H}_{\text{int}} \equiv \begin{pmatrix} 1/2 - \phi_A^0 + \phi_A^z & 0 & \phi_A^x + i\phi_A^y & 0 \\ 0 & 1/2 - \phi_B^0 + \phi_B^z & 0 & \phi_B^x + i\phi_B^y \\ \phi_A^x - i\phi_A^y & 0 & 1/2 - \phi_A^0 - \phi_A^z & 0 \\ 0 & \phi_B^x - i\phi_B^y & 0 & 1/2 - \phi_B^0 - \phi_B^z \end{pmatrix}.$$

(5.80)

On the other hand, the choice in chapter 5.3 corresponds to an Hartree-Fock-like

mean field decomposition where $\langle n_\sigma \rangle$, $\langle c_\uparrow^\dagger c_\downarrow \rangle$, $\langle c_\downarrow^\dagger c_\uparrow \rangle$ (which are linear combinations of the ϕ's) form the natural mean fields [27]

$$U \sum_i n_{i\uparrow} n_{i\downarrow} \approx U \sum_i \Big[\langle n_\uparrow \rangle n_\downarrow + n_\uparrow \langle n_\downarrow \rangle - \langle c_\uparrow^\dagger c_\downarrow \rangle c_\downarrow^\dagger c_\uparrow - \langle c_\downarrow^\dagger c_\uparrow \rangle c_\uparrow^\dagger c_\downarrow - \langle n_\uparrow \rangle \langle n_\downarrow \rangle + \langle c_\uparrow^\dagger c_\downarrow \rangle \langle c_\downarrow^\dagger c_\uparrow \rangle \Big] \tag{5.81}$$

$$= U \sum_i \Big[(\phi_i^x + i\phi_i^y) c_{i\uparrow}^\dagger c_{i\downarrow} + (\phi_i^x - i\phi_i^y) c_{i\downarrow}^\dagger c_{i\uparrow} - (\phi_i^0 - \phi_i^z) n_{i\uparrow} - (\phi_i^0 + \phi_i^z) n_{i\downarrow} - \langle \boldsymbol{\phi}_i, \boldsymbol{\phi}_i \rangle_{\mathcal{M}} \Big]. \tag{5.82}$$

Fourier transforming gives [27]

$$U \sum_i n_{i\uparrow} n_{i\downarrow} \approx \sum_{\boldsymbol{k}} \psi_{\boldsymbol{k}}^\dagger U \left(\mathcal{H}_{\text{int}} - \frac{1}{2} \mathbb{I} \right) \psi_{\boldsymbol{k}} - UN(\langle \boldsymbol{\phi}_A, \boldsymbol{\phi}_A \rangle_{\mathcal{M}} + \langle \boldsymbol{\phi}_B, \boldsymbol{\phi}_B \rangle_{\mathcal{M}}). \tag{5.83}$$

Comparing to Eq. 5.80, we see that this decomposition gives a mean-field interaction that is a factor of two larger than the Heisenberg-like decoupling.

Chapter 6

Conclusion

In chapter 2, we introduced relevant concepts of topological band theory and graphene as a Dirac metal. Then, in chapter 3 we directly build on this knowledge and studied in depth a new interface between the Haldane honeycomb model - the prototypical model of a Chern insulator - and graphene.

We revealed the mechanism of a topological proximity effect. Here, *proximity* refers to particle hole processes between the Haldane and graphene layer. We showed how this interlayer hopping induces a gap in the bulk of graphene and we argued by means of an approximative model how graphene acquires therefore non-trivial topology. In fact, we observered that the Haldane model with Chern number $+1$ induced a Chern number -1 in the graphene layer.

Moreover, we illustrated the bulk-edge correspondence in relation with the Kane-Mele model and described the state of the system in the strong coupling limit.

Finally, we proposed in detail a possible pathway for an experimental realization of the topological proximity effect in cold atoms. In particular, we generalized the effects observed in the Haldane-graphene model to a Haldane bilayer model with asymmetric Semenoff masses which could possibly be realized in cold atoms.

In chapter 4, we have introduced a stochastic theory to describe interaction effects in the spinless, fermionic Haldane model with nearest-neighbor interactions. In particular, we derived a stochastic mean field decomposition scheme from a variational principle. We found that from the solution of the self-consistent mean field equations we were able to accurately describe the Mott transition in the interacting Haldane honeycomb model. These results were supported by complementary iDMRG calculations [26]. In fact, we were able to confirm the speculated [15] first order nature of the Mott transition, by means of our mean field theory, iDMRG computations, and Ginzburg-Landau arguments.

Furthermore, we have studied the effect of light-matter coupling and we have shown that the Mott transition can be probed through circular dichroism of light.

Then, we have introduced in new quantity dubbed *stochastic Chern number* which corresponds to a sampling of the ground-state Chern number on the whole ensemble of stochastic variables. Physically, this situation can describe disorder effects in the interaction strength resulting, e.g., from fluctuations in the lattice potential and producing a mixed state.

Moreover, we pointed out that fluctuations resulting from interaction effects produce a substantial amount of excited particle-hole pairs which act on the ground Chern number. We provided with the stochastic Chern number a non-quantized quantity which can act as a measure of the number of excited states in the system. Therefore, the stochastic Chern number can be seen as a stochastic manifestation of the topology in the system in the presence of strong interactions.

Finally, we fleshed out an analogy of these stochastic measures with temperature effects.

The stochastic approach to the interacting Haldane honeycomb model is physically intuitive, easy to implement, and leads the way to further studies of interaction effects. In particular, possible generalizations to bi- or multilayer systems, or similar systems such as the Kane-Mele model provide exciting pathways for

future research. Another interesting direction could be a possible application of the approach to attractive interactions instead of repulsive ones.

Last but not least, in chapter 5.4, we applied our variational stochastic functional path integral approach to the Mott transition in the interacting Kane-Mele-Hubbard model. In particular, we described - starting from the same variational decomposition scheme - two different kinds of mean field theories, which are in principal both valid approaches but deliver different results for the Mott transition line in the Kane-Mele-Hubbard model.

First, we described a variational mean field ansatz which aims (similar to the approach in the interacting Haldane model) to minimize the total energy of the original (i.e. undecoupled) Hamiltonian with respect to a variational mean field wave function. This approach delivers a set of self-consistent equations which are independent from the choice of gauge of the Gaussian auxiliary field introduced by means of a Hubbard-Stratonovich transformation.

One the other hand, we described an alternative pathway to a mean field theory. This method, although in principle not gauge independent, is based on the idea of SU(2) symmetry preservation. It delivers an analytic transition line that has proved to be very close to results obtained from approximative numeric simulations. The method may be developed further to study fractional topological phases and interacting topological superconductors.

Résumé en français

Une phase de matière est une région de l'espace des paramètres physiques correspondants dans laquelle toutes les propriétés physiques d'un matériau sont essentiellement uniformes [1]. Landau a pu établir un mécanisme de classification des différentes phases de la matière sur la base des symétries sous-jacentes au système physique [2, 3]. La notion de paradigme de Landau est que, si les systèmes physiques sont *désordonnés* à haute température, ils acquièrent un *ordre* en raison d'une rupture spontanée de symétrie en dessous d'une température critique T_c. Cela signifie qu'en dessous de T_c, un paramètre d'ordre magnétique local devient fini, de sorte que le système établit un certain ordre à longue portée. Quantitativement, la rupture de symétrie peut être capturée par le comportement d'un paramètre d'ordre local à la transition de phase. Lors d'une transition de phase de premier ordre, le paramètre d'ordre local change de façon discontinue, alors que lors d'une transition de phase de second ordre, le changement est continu.

Von Klitzing [6] a décrit en 1980 la quantification de la conductivité de Hall dans un gaz d'électrons bidimensionnel exposé à un champ magnétique externe. Cet effet, connu sous le nom d'effet Hall quantique entier (IQHE), est l'une des découvertes les plus importantes qui décrivent la physique *au-delà* du paradigme de Landau.

Il s'avère que la classification d'une phase de Hall quantique ne peut pas reposer sur un paramètre d'ordre *local*. Au contraire, il est apparu clairement qu'un

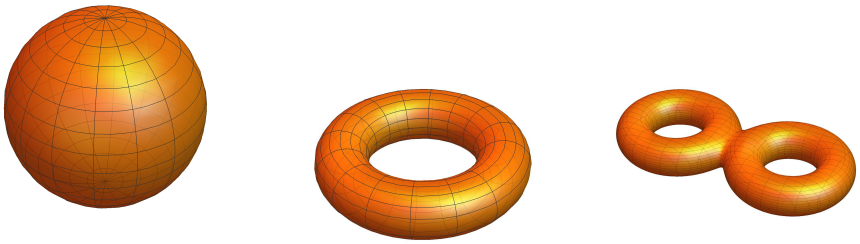

FIGURE 1: Variétés topologiques avec différents genres g. A gauche : Une sphère avec $g = 0$. Au milieu : Un tore avec $g = 1$. A droite : Un tore double avec $g = 2$.

autre type de mécanisme est en jeu, impliquant des propriétés *globales* de la fonction d'onde. Mathématiquement, le domaine de la *topologie* est entré en jeu.

La topologie est la branches des mathématiques qui s'intéresse à la description et à la classification de la forme des objets mathématiques. La topologie considère deux objets mathématiques comme équivalents tant qu'ils peuvent être déformés de façon continue l'un dans l'autre, c'est-à-dire qu'il existe une déformation continue entre eux [7]. Dans le cadre de la classification des états fondamentaux en l'absence de brissure de symétrie, une phase obéit à un *ordre topologique* lorsque la dégénérescence de l'état fondamental dépend de la topologie de la variété sous-jacent [8]. Plus précisément, la dégénérescence de l'état fondamental est de 2^{2g} où g est le genre de la variété [9]. Le genre d'une variété topologique et orientable est un entier relatif représentant le nombre maximum de coupes le long de courbes simples fermées non intersectées sans couper la surface en morceaux [10]. Plus intuitivement, le genre g compte le nombre de *trous* dans une variété, voir Fig. 1.

Sur la base de la topologie du réseau, l'état fondamental d'un système d'ordre topologique peut être séparé en différents secteurs topologiques [8]. Chaque secteur correspond à une fonction d'onde distincte de l'état fondamental qui contribue à la dégénérescence de l'état fondamental. La nature *globale* de l'ordre

topologique est exprimée par le fait qu'il n'existe pas de paramètre d'ordre local pouvant expliquer la dégénérescence de l'état fondamental (sur la base de toutes les fonctions d'onde de tous les secteurs), et par conséquent, la théorie de Landaus n'est pas applicable [11, 8, 9].

Dans cette thèse

Dans le chapitre 2, nous présentons au lecteur les principaux concepts de la théorie des bandes topologiques, le graphène en tant que métal de Dirac et le modèle de Haldane - le modèle prototypique d'un isolant de Chern. Tout d'abord, nous passons en revue les principaux concepts des phases de Berry [12] et introduisons sur cette base la notion de courbure de Berry et le premier nombre de Chern. De plus, nous récapitulons le calcul indépendant de la jauge de ces quantités sur un réseau discret.

Ensuite, nous introduisons le concept d'un métal de Dirac à l'exemple du graphène [13]. Nous nous plongeons dans sa description mathématique et étoffons sa riche phénoménologie à basse énergie.

Ensuite, nous suivons les traces de Haldane [14] et explorons son chemin pour trouver un moyen de réaliser un effet Hall quantique sans l'application d'un champ magnétique externe dans une couche de graphène.

Dans le chapitre 3, nous révélons un effet de proximité entre un isolant à bande topologique (Chern) décrit par un modèle de Haldane et des particules de Dirac d'une couche de graphène. Nous montrons qu'en couplant faiblement ces deux systèmes (c'est-à-dire par proximité), nous sommes capables d'induire un index topologique non triviale dans la couche de graphène. Nous plongeons dans les mécanismes sous-jacents et explorons en détail la riche phénoménologie de ce système. De manière importante, nous présentons des protocoles expérimentaux

conçus pour révéler ses effets. En particulier, nous proposons un modèle de Haldane bicouche, conçu pour observer l'effet de proximité topologique dans un dispositif expérimental à atomes froids.

Dans le chapitre 4, nous quittons le domaine des modèles exactement solvables et considérons les corrélations fortes dans un isolant de Chern. Au cours de la dernière décennie, des progrès ont été réalisés dans la description des systèmes de Chern fortement corrélés, dans le cas bosonique [15, 16], et à la fois pour les systèmes sans spin [15, 17, 18, 19] et avec spin [20, 21, 22, 23, 24]. Cependant, le système que nous souhaitons étudier dans ce chapitre, c'est-à-dire le modèle de Haldane fortement corrélé *sans spin* n'a pas été résolu de manière convaincante au moyen d'un modèle approximatif. Par conséquent, nous développons une nouvelle description stochastique des propriétés topologiques du modèle de Haldane en nid d'abeille en présence des fortes corrélations. Nous confirmons la nature de premier ordre de la transition de Mott (qui a été précédemment spéculée [15]) au moyen d'une approche variationnelle du champ moyen soutenue par les résultats du groupe de renormalisation de la matrice de densité (iDMRG) et les arguments de Ginzburg-Landau.

Plus important encore, nous introduisons une nouvelle quantité appelée *nombre de Chern stochastique* qui fournit une mesure de la topologie du système en présence de fortes corrélations. En particulier, cette quantité compte de manière stochastique le nombre de paires de particules-trous produites en raison des effets de corrélation qui agissent sur le nombre de Chern de l'état fondamental. Nous utilisons le dichroïsme de la lumière pour faire le lien dans la quantification des quasi-particules excitées et montrons une analogie entre les paires de particules-trous induites par les corrélations et les effets de température.

Enfin, dans le chapitre 5, nous revisitons le model de Kane-Mele-Hubbard. De même que pour le modèle de Haldane avec des fortes corrélations, dans le chapitre 4, nous développons une approche variationnelle de l'isolant topologique

à forte corrélation $\mathbb{Z}_2$. Nous présentons deux méthodes différentes pour calculer la transition de Mott. En particulier, nous montrons une approche analytique partant de notre schéma de découplage stochastique qui permet de décrire la ligne de transition de Mott avec une seule équation.

Acknowledgments

First and foremost, I would like to thank my thesis advisor Karyn Le Hur. During my time at École Polytechnique, I had the great opportunity to learn from her and work with her on extremely interesting projects. Karyn is a brilliant advisor, she loves to teach and do research with young physicists with a great amount of dedication and passion. Especially, I am grateful for the great freedom she provided me with, so that I could find my professional path.

Then, I would like to thank Nathan Goldman and Mark-Oliver Goerbig for reviewing this thesis as well as the members of the jury Sylvain Capponi, Thierry Jolicoeur, Luca Perfetti and Tim Ziman.

Furthermore, I would like to thank my collaborators and other brilliant physicists with whom I had the privilege to share enriching discussions with: Adolfo Grushin, Kirill Plekhanov, Monika Aidelsburger, Christoph Weitenberg, Achim Rosch, and Yong-Baek Kim.

Also, I would like to thank my thesis mentors Silke Biermann and Nicolas Regnault for their advice and great help they provided me with.

Moreover, I would like to thank my colleagues at École Polytechnique for their company: Fan Yang, Ariane Soret, Joel Hutchinson, Cheng Peng, Ephraim Bernhardt and Julian Legendre.

Finally, I would like to thank my family for their enduring support.

Bibliography

[1] E. Fermi. *Thermodynamics*. Dover books in physics and mathematical physics. Dover Publications, 1956. ISBN: 9780486603612.

[2] L.D. Landau et al. *Statistical physics*.

[3] V. Ginzburg and L. Landau. "Toward the superconductivity theory". In: *Zhurnal Eksp. Yheoret. Physics* 29 (1950). cited By 1, p. 1064.

[4] N. Goldenfeld. *Lectures on phase transitions and the renormalization group*. 1992.

[5] P. M. Chaikin and T. C. Lubensky. *Principles of Condensed Matter Physics*. Sept. 2000, p. 720.

[6] K. v. Klitzing, G. Dorda, and M. Pepper. "New Method for High-Accuracy Determination of the Fine-Structure Constant Based on Quantized Hall Resistance". In: *Phys. Rev. Lett.* 45 (6 1980), pp. 494–497. DOI: 10.1103/PhysRevLett.45.494. URL: https://link.aps.org/doi/10.1103/PhysRevLett.45.494.

[7] M. Nakahara. *Geometry, Topology and Physics, Second Edition*. Graduate student series in physics. Taylor & Francis, 2003. ISBN: 9780750306065. URL: https://books.google.fr/books?id=cH-XQB0Ex5wC.

[8] Mahito Kohmoto. "Topological invariant and the quantization of the Hall conductance". In: *Annals of Physics* 160.2 (1985), pp. 343–354. ISSN: 0003-4916. DOI: https://doi.org/10.1016/0003-4916(85)90148-4. URL: https://www.sciencedirect.com/science/article/pii/0003491685901484.

[9] X. G. Wen and Q. Niu. "Ground-state degeneracy of the fractional quantum Hall states in the presence of a random potential and on high-genus Riemann surfaces". In: *Phys. Rev. B* 41 (13 1990), pp. 9377–9396. DOI: 10.1103/PhysRevB.41.9377.

[10] J.R. Munkres. *Topology*. Featured Titles for Topology Series. Prentice Hall, Incorporated, 2000. ISBN: 9780131816299.

[11] B.A. Bernevig and T.L. Hughes. *Topological Insulators and Topological Superconductors*. Princeton University Press, 2013. ISBN: 9780691151755. URL: https://books.google.fr/books?id=w0n7JHSSxrsC.

[12] M. V. Berry. "Quantal Phase Factors Accompanying Adiabatic Changes". In: *Proceedings of the Royal Society of London. Series A, Mathematical and Physical Sciences* 392.1802 (1984), pp. 45–57. ISSN: 00804630.

[13] A. H. Castro Neto et al. "The electronic properties of graphene". In: *Rev. Mod. Phys.* 81 (1 2009), pp. 109–162. DOI: 10.1103/RevModPhys.81.109. URL: https://link.aps.org/doi/10.1103/RevModPhys.81.109.

[14] F. D. M. Haldane. "Model for a Quantum Hall Effect without Landau Levels: Condensed-Matter Realization of the "Parity Anomaly"". In: *Phys. Rev. Lett.* 61 (18 1988), pp. 2015–2018. DOI: 10.1103/PhysRevLett.61.2015. URL: https://link.aps.org/doi/10.1103/PhysRevLett.61.2015.

[15] Christopher N. Varney et al. "Interaction effects and quantum phase transitions in topological insulators". In: *Phys. Rev. B* 82 (11 2010), p. 115125. DOI: 10.1103/PhysRevB.82.115125. URL: https://link.aps.org/doi/10.1103/PhysRevB.82.115125.

[16] . "Chiral bosonic phases on the Haldane honeycomb lattice". In: *Phys. Rev. B* 91 (9 2015), p. 094502. DOI: 10.1103/PhysRevB.91.094502. URL: https://link.aps.org/doi/10.1103/PhysRevB.91.094502.

[17] Christopher N. Varney et al. "Topological phase transitions for interacting finite systems". In: *Phys. Rev. B* 84 (24 2011), p. 241105. DOI: 10.1103/PhysRevB.84.241105. URL: https://link.aps.org/doi/10.1103/PhysRevB.84.241105.

[18] Lei Wang et al. *Charge-density-wave and topological transitions in interacting Haldane model*. 2010. arXiv: 1012.5163 [cond-mat.str-el].

[19] E Alba, J K Pachos, and J J García-Ripoll. "Winding number order in the Haldane model with interactions". In: *New Journal of Physics* 18.3 (2016), p. 033022. DOI: 10.1088/1367-2630/18/3/033022. URL: https://doi.org/10.1088%2F1367-2630%2F18%2F3%2F033022.

[20] C. Hickey, P. Rath, and A. Paramekanti. "Competing chiral orders in the topological Haldane-Hubbard model of spin-$\frac{1}{2}$ fermions and bosons". In: *Phys. Rev. B* 91 (13 2015), p. 134414. DOI: 10.1103/PhysRevB.91.134414. URL: https://link.aps.org/doi/10.1103/PhysRevB.91.134414.

[21] Joseph Maciejko and Andreas Rüegg. "Topological order in a correlated Chern insulator". In: *Phys. Rev. B* 88 (24 2013), p. 241101. DOI: 10.1103/PhysRevB.88.241101. URL: https://link.aps.org/doi/10.1103/PhysRevB.88.241101.

[22] Diana Prychynenko and Sebastian D. Huber. "Z2 slave-spin theory of a strongly correlated Chern insulator". In: *Physica B: Condensed Matter* 481 (2016), pp. 53–58. ISSN: 0921-4526. DOI: 10.1016/j.physb.2015.10.027. URL: http://dx.doi.org/10.1016/j.physb.2015.10.027.

[23] , Lei Wang, and Matthias Troyer. "First-order topological phase transition of the Haldane-Hubbard model". In: *Phys. Rev. B* 94 (3 2016), p. 035109. DOI: 10.1103/PhysRevB.94.035109. URL: https://link.aps.org/doi/10.1103/PhysRevB.94.035109.

[24] T. I. Vanhala et al. “Topological Phase Transitions in the Repulsively Interacting Haldane-Hubbard Model”. In: *Phys. Rev. Lett.* 116 (2016), p. 225305. DOI: 10.1103/PhysRevLett.116.225305. URL: https://journals.aps.org/prl/abstract/10.1103/PhysRevLett.116.225305.

[25] Peng Cheng et al. “Topological proximity effects in a Haldane graphene bilayer system”. In: *Phys. Rev. B* 100 (8 2019), p. 081107. DOI: 10.1103/PhysRevB.100.081107. URL: https://link.aps.org/doi/10.1103/PhysRevB.100.081107.

[26] Philipp W. Klein, Adolfo G. Grushin, and Karyn Le Hur. “Interacting stochastic topology and Mott transition from light response”. In: *Phys. Rev. B* 103 (3 2021), p. 035114. DOI: 10.1103/PhysRevB.103.035114. URL: https://link.aps.org/doi/10.1103/PhysRevB.103.035114.

[27] Joel Hutchinson, Philipp W. Klein, and Karyn Le Hur. “Analytical approach for the Mott transition in the Kane-Mele-Hubbard model”. In: *Phys. Rev. B* 104 (7 2021), p. 075120. DOI: 10.1103/PhysRevB.104.075120. URL: https://link.aps.org/doi/10.1103/PhysRevB.104.075120.

[28] A. Messiah. *Quantum Mechanics*. Dover books on physics. Dover Publications, 1999. ISBN: 9780486409245. URL: https://books.google.fr/books?id=mwssSDXzkNcC.

[29] J.D. Jackson. *Classical Electrodynamics*. Wiley, 2012. ISBN: 9788126510948. URL: https://books.google.fr/books?id=8qHCZjJHRUgC.

[30] Raffaele Resta. “Manifestations of Berrys phase in molecules and condensed matter”. In: *Journal of Physics: Condensed Matter* 12.9 (2000), R107–R143. DOI: 10.1088/0953-8984/12/9/201. URL: https://doi.org/10.1088/0953-8984/12/9/201.

[31] Stephan Rachel. “Interacting topological insulators: a review”. In: *Reports on Progress in Physics* 81.11 (2018), p. 116501. ISSN: 1361-6633. DOI: 10.

1088/1361-6633/aad6a6. URL: http://dx.doi.org/10.1088/1361-6633/aad6a6.

[32] D. J. Thouless et al. "Quantized Hall Conductance in a Two-Dimensional Periodic Potential". In: *Phys. Rev. Lett.* 49 (6 1982), pp. 405–408. DOI: 10.1103/PhysRevLett.49.405. URL: https://link.aps.org/doi/10.1103/PhysRevLett.49.405.

[33] Takahiro Fukui, Yasuhiro Hatsugai, and Hiroshi Suzuki. "Chern Numbers in Discretized Brillouin Zone: Efficient Method of Computing (Spin) Hall Conductances". In: *Journal of the Physical Society of Japan* 74.6 (2005), 1674–1677. ISSN: 1347-4073. DOI: 10.1143/jpsj.74.1674. URL: http://dx.doi.org/10.1143/JPSJ.74.1674.

[34] Jérôme Cayssol. "Introduction to Dirac materials and topological insulators". In: *Comptes Rendus Physique* 14.9-10 (2013), 760–778. ISSN: 1631-0705. DOI: 10.1016/j.crhy.2013.09.012. URL: http://dx.doi.org/10.1016/j.crhy.2013.09.012.

[35] Gordon W. Semenoff. "Condensed-Matter Simulation of a Three-Dimensional Anomaly". In: *Phys. Rev. Lett.* 53 (26 1984), pp. 2449–2452. DOI: 10.1103/PhysRevLett.53.2449. URL: https://link.aps.org/doi/10.1103/PhysRevLett.53.2449.

[36] M. Z. Hasan and C. L. Kane. "Colloquium: Topological insulators". In: *Reviews of Modern Physics* 82.4 (2010), 3045–3067. ISSN: 1539-0756. DOI: 10.1103/revmodphys.82.3045. URL: http://dx.doi.org/10.1103/RevModPhys.82.3045.

[37] Chao-Xing Liu, Shou-Cheng Zhang, and Xiao-Liang Qi. "The quantum anomalous Hall effect". In: *Annual Review of Condensed Matter Physics* 7 (2016), pp. 301–321. DOI: https://doi.org/10.1146/annurev-conmatphys-

031115-011417. URL: https://www.annualreviews.org/doi/abs/10.1146/annurev-conmatphys-031115-011417.

[38] J. W. McIver et al. "Light-induced anomalous Hall effect in graphene". In: *Nature Physics* (2019). ISSN: 1745-2481. DOI: 10.1038/s41567-019-0698-y. URL: http://dx.doi.org/10.1038/s41567-019-0698-y.

[39] F. D. M. Haldane and S. Raghu. "Possible Realization of Directional Optical Waveguides in Photonic Crystals with Broken Time-Reversal Symmetry". In: *Phys. Rev. Lett.* 100 (1 2008), p. 013904. DOI: 10.1103/PhysRevLett.100.013904. URL: https://link.aps.org/doi/10.1103/PhysRevLett.100.013904.

[40] Ling Lu, John D. Joannopoulos, and Marin Soljacic. "Topological photonics". In: *Nature Photonics* 8.11 (2014), pp. 821–829. ISSN: 1749-4893. DOI: 10.1038/nphoton.2014.248. URL: http://dx.doi.org/10.1038/nphoton.2014.248.

[41] Mikael C. Rechtsman et al. "Photonic Floquet topological insulators". In: *Nature* 496.7444 (2013), pp. 196–200. ISSN: 1476-4687. DOI: 10.1038/nature12066. URL: http://dx.doi.org/10.1038/nature12066.

[42] Jens Koch et al. "Time-reversal-symmetry breaking in circuit-QED-based photon lattices". In: *Phys. Rev. A* 82 (4 2010), p. 043811. DOI: 10.1103/PhysRevA.82.043811. URL: https://link.aps.org/doi/10.1103/PhysRevA.82.043811.

[43] Karyn Le Hur et al. "Many-body quantum electrodynamics networks: Non-equilibrium condensed matter physics with light". In: *Comptes Rendus Physique* 17.8 (2016), pp. 808–835. ISSN: 1631-0705. DOI: 10.1016/j.crhy.2016.05.003. URL: http://dx.doi.org/10.1016/j.crhy.2016.05.003.

[44] Tomoki Ozawa et al. “Topological photonics”. In: *Rev. Mod. Phys.* 91 (1 2019), p. 015006. DOI: 10.1103/RevModPhys.91.015006. URL: https://link.aps.org/doi/10.1103/RevModPhys.91.015006.

[45] Gregor Jotzu et al. “Experimental realization of the topological Haldane model with ultracold fermions”. In: *Nature* 515.7526 (2014), pp. 237–240. ISSN: 1476-4687. DOI: 10.1038/nature13915. URL: http://dx.doi.org/10.1038/nature13915.

[46] N. Flaschner et al. “Experimental reconstruction of the Berry curvature in a Floquet Bloch band”. In: *Science* 352.6289 (2016), pp. 1091–1094. ISSN: 1095-9203. DOI: 10.1126/science.aad4568. URL: http://dx.doi.org/10.1126/science.aad4568.

[47] S. Rachel and K. Le Hur. “Topological Insulators and Mott Physics from the Hubbard Interaction”. In: *Phys. Rev. B* 82 (2010), p. 075106. DOI: https://doi.org/10.1103/PhysRevB.82.075106. URL: https://journals.aps.org/prb/abstract/10.1103/PhysRevB.82.075106.

[48] Markus König et al. “The Quantum Spin Hall Effect: Theory and Experiment”. In: *Journal of the Physical Society of Japan* 77.3 (2008), p. 031007. DOI: 10.1143/JPSJ.77.031007. eprint: https://doi.org/10.1143/JPSJ.77.031007. URL: https://doi.org/10.1143/JPSJ.77.031007.

[49] Duc Thanh Tran et al. “Probing topology by heating: Quantized circular dichroism in ultracold atoms”. In: *Science Advances* 3.8 (2017), e1701207. ISSN: 2375-2548. DOI: 10.1126/sciadv.1701207. URL: http://dx.doi.org/10.1126/sciadv.1701207.

[50] Luca Asteria et al. “Measuring quantized circular dichroism in ultracold topological matter”. In: *Nature Physics* 15.5 (2019), pp. 449–454. ISSN: 1745-2481. DOI: 10.1038/s41567-019-0417-8. URL: http://dx.doi.org/10.1038/s41567-019-0417-8.

[51] Fernando de Juan et al. "Quantized circular photogalvanic effect in Weyl semimetals". In: *Nature Communications* 8 (2017), p. 15995. DOI: 10.1038/ncomms15995. URL: https://www.nature.com/articles/ncomms15995.

[52] "Nonperturbative Calculation of Transition Amplitudes". In: *Atom—Photon Interactions*. John Wiley Sons, Ltd, 1998. Chap. 3, pp. 165–255. ISBN: 9783527617197. DOI: https://doi.org/10.1002/9783527617197.ch3. eprint: https://onlinelibrary.wiley.com/doi/pdf/10.1002/9783527617197.ch3. URL: https://onlinelibrary.wiley.com/doi/abs/10.1002/9783527617197.ch3.

[53] Karyn Le Hur. "Andreev scattering in the asymmetric ladder with preformed bosonic pairs". In: *Physical Review B* 64.6 (2001). ISSN: 1095-3795. DOI: 10.1103/physrevb.64.060502. URL: http://dx.doi.org/10.1103/PhysRevB.64.060502.

[54] Karyn Le Hur, Smitha Vishveshwara, and Cristina Bena. "Double-gap superconducting proximity effect in armchair carbon nanotubes". In: *Phys. Rev. B* 77 (4 2008), p. 041406. DOI: 10.1103/PhysRevB.77.041406. URL: https://link.aps.org/doi/10.1103/PhysRevB.77.041406.

[55] T Shoman et al. "Topological proximity effect in a topological insulator hybrid". In: *Nature communications* 6 (Mar. 2015), p. 6547. DOI: 10.1038/ncomms7547.

[56] Timothy H. Hsieh et al. "Bulk Topological Proximity Effect". In: *Phys. Rev. Lett.* 116 (8 2016), p. 086802. DOI: 10.1103/PhysRevLett.116.086802. URL: https://link.aps.org/doi/10.1103/PhysRevLett.116.086802.

[57] Jun-Hui Zheng and Walter Hofstetter. "Topological invariant for two-dimensional open systems". In: *Phys. Rev. B* 97 (19 2018), p. 195434. DOI: 10.1103/PhysRevB.97.195434. URL: https://link.aps.org/doi/10.1103/PhysRevB.97.195434.

[58] Leticia Tarruell et al. “Creating, moving and merging Dirac points with a Fermi gas in a tunable honeycomb lattice”. In: *Nature* 483.7389 (2012), 302–305. ISSN: 1476-4687. DOI: 10.1038/nature10871. URL: http://dx.doi.org/10.1038/nature10871.

[59] P. Roushan et al. “Observation of topological transitions in interacting quantum circuits”. In: *Nature* 515.7526 (2014), 241–244. ISSN: 1476-4687. DOI: 10.1038/nature13891. URL: http://dx.doi.org/10.1038/nature13891.

[60] M. D. Schroer et al. “Measuring a Topological Transition in an Artificial Spin-1/2 System”. In: *Phys. Rev. Lett.* 113 (5 2014), p. 050402. DOI: 10.1103/PhysRevLett.113.050402. URL: https://link.aps.org/doi/10.1103/PhysRevLett.113.050402.

[61] Loïc Henriet et al. “Topology of a dissipative spin: Dynamical Chern number, bath-induced nonadiabaticity, and a quantum dynamo effect”. In: *Phys. Rev. B* 95 (5 2017), p. 054307. DOI: 10.1103/PhysRevB.95.054307. URL: https://link.aps.org/doi/10.1103/PhysRevB.95.054307.

[62] Philipp Hauke, Maciej Lewenstein, and André Eckardt. “Tomography of Band Insulators from Quench Dynamics”. In: *Phys. Rev. Lett.* 113 (4 2014), p. 045303. DOI: 10.1103/PhysRevLett.113.045303. URL: https://link.aps.org/doi/10.1103/PhysRevLett.113.045303.

[63] T. Li et al. “Bloch state tomography using Wilson lines”. In: *Science* 352.6289 (2016), 1094–1097. ISSN: 1095-9203. DOI: 10.1126/science.aad5812. URL: http://dx.doi.org/10.1126/science.aad5812.

[64] M. Aidelsburger et al. “Measuring the Chern number of Hofstadter bands with ultracold bosonic atoms”. In: *Nature Physics* 11.2 (2014), 162–166. ISSN: 1745-2481. DOI: 10.1038/nphys3171. URL: http://dx.doi.org/10.1038/nphys3171.

[65] Matthias Braun, Luca Chirolli, and Guido Burkard. "Signature of chirality in scanning-probe imaging of charge flow in graphene". In: *Phys. Rev. B* 77 (11 2008), p. 115433. DOI: 10.1103/PhysRevB.77.115433. URL: https://link.aps.org/doi/10.1103/PhysRevB.77.115433.

[66] Mark A. Topinka, Robert M. Westervelt, and Eric J. Heller. "Imaging Electron Flow". In: *Physics Today* 56.12 (2003), pp. 47–52. DOI: 10.1063/1.1650228. eprint: https://doi.org/10.1063/1.1650228. URL: https://doi.org/10.1063/1.1650228.

[67] M. I. Katsnelson, K. S. Novoselov, and A. K. Geim. "Chiral tunnelling and the Klein paradox in graphene". In: *Nature Physics* 2.9 (2006), 620–625. ISSN: 1745-2481. DOI: 10.1038/nphys384. URL: http://dx.doi.org/10.1038/nphys384.

[68] N. Stander, B. Huard, and D. Goldhaber-Gordon. "Evidence for Klein Tunneling in Graphene $p-n$ Junctions". In: *Phys. Rev. Lett.* 102 (2 2009), p. 026807. DOI: 10.1103/PhysRevLett.102.026807. URL: https://link.aps.org/doi/10.1103/PhysRevLett.102.026807.

[69] Liang Fu and C. L. Kane. "Topological insulators with inversion symmetry". In: *Phys. Rev. B* 76 (4 2007), p. 045302. DOI: 10.1103/PhysRevB.76.045302. URL: https://link.aps.org/doi/10.1103/PhysRevB.76.045302.

[70] Wei Wu et al. "Quantum Spin Hall Insulators with Interactions and Lattice Anisotropy". In: *Phys. Rev. B* 85 (2010), p. 205102. DOI: https://doi.org/10.1103/PhysRevB.85.205102. URL: https://journals.aps.org/prb/abstract/10.1103/PhysRevB.85.205102.

[71] D. N. Sheng et al. "Quantum Spin-Hall Effect and Topologically Invariant Chern Numbers". In: *Phys. Rev. Lett.* 97 (3 2006), p. 036808. DOI: 10.1103/

PhysRevLett.97.036808. URL: https://link.aps.org/doi/10.1103/PhysRevLett.97.036808.

[72] Joel Hutchinson and Karyn Le Hur. "Quantum Entangled Fractional Topology and Curvatures". In: *Communications Physics* 4.1 (2021), p. 144. DOI: 10.1038/s42005-021-00641-0. URL: https://hal.archives-ouvertes.fr/hal-02507659.

[73] C. L. Kane and E. Mele. "Quantum Spin Hall effect in Graphene". In: *Phys. Rev. Lett.* 95 (2005), p. 226801. DOI: 10.1103/PhysRevLett.95.226801. URL: https://journals.aps.org/prl/abstract/10.1103/PhysRevLett.95.226801.

[74] Jun Kondo. "Resistance Minimum in Dilute Magnetic Alloys". In: *Progress of Theoretical Physics* 32.1 (July 1964), pp. 37–49. ISSN: 0033-068X. DOI: 10.1143/PTP.32.37. eprint: https://academic.oup.com/ptp/article-pdf/32/1/37/5193092/32-1-37.pdf. URL: https://doi.org/10.1143/PTP.32.37.

[75] N. F. MOTT. "Metal-Insulator Transition". In: *Rev. Mod. Phys.* 40 (4 1968), pp. 677–683. DOI: 10.1103/RevModPhys.40.677. URL: https://link.aps.org/doi/10.1103/RevModPhys.40.677.

[76] H. J. Schulz. *Functional Integrals for Correlated Electrons*. 1994. arXiv: cond-mat/9402103 [cond-mat].

[77] Alexander Altland and Ben D. Simons. *Condensed Matter Field Theory*. 2nd ed. Cambridge University Press, 2010. DOI: 10.1017/CBO9780511789984.

[78] Piers Coleman. *Introduction to Many-Body Physics*. Cambridge University Press, 2015. DOI: 10.1017/CBO9781139020916.

[79] Rafael Agra, Frédéric van Wijland, and Emmanuel Trizac. "On the free energy within the mean-field approximation". In: *European Journal of Physics*

27.2 (2006), pp. 407–412. ISSN: 1361-6404. DOI: 10.1088/0143-0807/27/2/022. URL: http://dx.doi.org/10.1088/0143-0807/27/2/022.

[80] J. J. Binney et al. *The Theory of Critical Phenomena: An Introduction to the Renormalization Group*. New York, NY, USA: Oxford University Press, Inc., 1992. ISBN: 0198513933, 9780198513933.

[81] Johannes Hauschild and Frank Pollmann. "Efficient numerical simulations with Tensor Networks: Tensor Network Python (TeNPy)". In: *SciPost Phys. Lect. Notes* (2018), p. 5. DOI: 10.21468/SciPostPhysLectNotes.5. URL: https://scipost.org/10.21468/SciPostPhysLectNotes.5.

[82] Adolfo G. Grushin et al. "Characterization and stability of a fermionic ν=1/3 fractional Chern insulator". In: *Phys. Rev. B* 91.3 (2015), p. 035136. DOI: https://doi.org/10.1103/PhysRevB.91.035136. URL: https://journals.aps.org/prb/abstract/10.1103/PhysRevB.91.035136.

[83] Sylvain Capponi. "Phase diagram of interacting spinless fermions on the honeycomb lattice". In: *Journal of Physics: Condensed Matter* 29.4 (2016), p. 043002. DOI: 10.1088/1361-648x/29/4/043002. URL: https://doi.org/10.1088%2F1361-648x%2F29%2F4%2F043002.

[84] P.C. Hohenberg and A.P. Krekhov. "An introduction to the Ginzburg?Landau theory of phase transitions and nonequilibrium patterns". In: *Physics Reports* 572 (2015), pp. 1–42. ISSN: 0370-1573. DOI: 10.1016/j.physrep.2015.01.001. URL: http://dx.doi.org/10.1016/j.physrep.2015.01.001.

[85] L. Henriet et al. "Topology of a dissipative spin: dynamical Chern number, bath induced non-adiabaticity and a quantum dynamo effect". In: *Phys. Rev. B* 95 (2017), p. 054307. DOI: https://doi.org/10.1103/PhysRevB.95.054307. URL: https://doi.org/10.1103/PhysRevB.95.054307.

[86] Julian Legendre and Karyn Le Hur. "Magnetic topological kagome systems". In: *Phys. Rev. Research* 2 (2020), 022043(R). DOI: https://doi.org/10.1103/PhysRevResearch.2.022043. URL: https://journals.aps.org/prresearch/abstract/10.1103/PhysRevResearch.2.022043.

[87] Joel Hutchinson and Karyn Le Hur. "Quantum Entangled Fractional Topology in Curvatures". In: *arXiv:2002.11823* (2020).

[88] A. Rivas, O. Viyuela, and M. A. Martin-Delgado. "Density-matrix Chern insulators: Finite-temperature generalization of topological insulators". In: *Phys. Rev. B* 88 (15 2013), p. 155141. DOI: 10.1103/PhysRevB.88.155141. URL: https://link.aps.org/doi/10.1103/PhysRevB.88.155141.

[89] C. L. Kane and E. J. Mele. "Z_2 Topological Order and the Quantum Spin Hall Effect". In: *Phys. Rev. Lett.* 95 (14 2005), p. 146802. DOI: 10.1103/PhysRevLett.95.146802. URL: https://link.aps.org/doi/10.1103/PhysRevLett.95.146802.

[90] B. Andrei Bernevig and Shou-Cheng Zhang. "Quantum Spin Hall Effect". In: *Phys. Rev. Lett.* 96 (10 2006), p. 106802. DOI: 10.1103/PhysRevLett.96.106802. URL: https://link.aps.org/doi/10.1103/PhysRevLett.96.106802.

[91] Christian Griset and Cenke Xu. "Phase diagram of the Kane-Mele-Hubbard model". In: *Physical Review B* 85.4 (2012). ISSN: 1550-235X. DOI: 10.1103/physrevb.85.045123. URL: http://dx.doi.org/10.1103/PhysRevB.85.045123.

[92] Ignacio J. Hamad, Claudio J. Gazza, and José A. Riera. "Helical currents in metallic Rashba strips". In: *Phys. Rev. B* 93 (20 2016), p. 205113. DOI: 10.1103/PhysRevB.93.205113. URL: https://link.aps.org/doi/10.1103/PhysRevB.93.205113.

[93] Dung-Hai Lee. "Effects of Interaction on Quantum Spin Hall Insulators". In: *Phys. Rev. Lett.* 107 (16 2011), p. 166806. DOI: 10.1103/PhysRevLett.107.166806. URL: https://link.aps.org/doi/10.1103/PhysRevLett.107.166806.

[94] Masoud Mardani, Mohammad-Sadegh Vaezi, and Abolhassan Vaezi. *Slave-spin approach to the strongly correlated systems*. 2011. arXiv: 1111.5980 [cond-mat.str-el].

[95] D. Soriano and J. Fernández-Rossier. "Spontaneous persistent currents in a quantum spin Hall insulator". In: *Phys. Rev. B* 82 (16 2010), p. 161302. DOI: 10.1103/PhysRevB.82.161302. URL: https://link.aps.org/doi/10.1103/PhysRevB.82.161302.

[96] M. Hohenadler, T. C. Lang, and F. F. Assaad. "Correlation Effects in Quantum Spin-Hall Insulators: A Quantum Monte Carlo Study". In: *Phys. Rev. Lett.* 106 (10 2011), p. 100403. DOI: 10.1103/PhysRevLett.106.100403. URL: https://link.aps.org/doi/10.1103/PhysRevLett.106.100403.

[97] M. Hohenadler et al. "Quantum phase transitions in the Kane-Mele-Hubbard model". In: *Phys. Rev. B* 85 (11 2012), p. 115132. DOI: 10.1103/PhysRevB.85.115132. URL: https://link.aps.org/doi/10.1103/PhysRevB.85.115132.

[98] Hsiang-Hsuan Hung et al. "Topological phase transition in a generalized Kane-Mele-Hubbard model: A combined quantum Monte Carlo and Green's function study". In: *Phys. Rev. B* 87 (12 2013), p. 121113. DOI: 10.1103/PhysRevB.87.121113. URL: https://link.aps.org/doi/10.1103/PhysRevB.87.121113.

[99] Manuel Laubach et al. "Rashba spin-orbit coupling in the Kane-Mele-Hubbard model". In: *Phys. Rev. B* 90 (16 2014), p. 165136. DOI: 10.1103/PhysRevB.90.165136. URL: https://link.aps.org/doi/10.1103/PhysRevB.90.165136.

[100] Zi Yang Meng, Hsing-Hsuan Hung, and Thomas C. Lang. "The Characterization of topological properties in Quantum Monte Carlo Simulations of the Kane–Mele–Hubbard Model". In: *Modern Physics Letters B* 28.01 (2013), p. 1430001. ISSN: 1793-6640. DOI: 10.1142/s0217984914300014. URL: http://dx.doi.org/10.1142/S0217984914300014.

[101] Youhei Yamaji and Masatoshi Imada. "Mott physics on helical edges of two-dimensional topological insulators". In: *Phys. Rev. B* 83 (20 2011), p. 205122. DOI: 10.1103/PhysRevB.83.205122. URL: https://link.aps.org/doi/10.1103/PhysRevB.83.205122.

[102] Shun-Li Yu, X. C. Xie, and Jian-Xin Li. "Mott Physics and Topological Phase Transition in Correlated Dirac Fermions". In: *Phys. Rev. Lett.* 107 (1 2011), p. 010401. DOI: 10.1103/PhysRevLett.107.010401. URL: https://link.aps.org/doi/10.1103/PhysRevLett.107.010401.

[103] Dong Zheng, Guang-Ming Zhang, and Congjun Wu. "Particle-hole symmetry and interaction effects in the Kane-Mele-Hubbard model". In: *Phys. Rev. B* 84.20 (2011), p. 205121. DOI: 10.1103/physrevb.84.205121. URL: http://dx.doi.org/10.1103/PhysRevB.84.205121.

[104] Tian-Sheng Zeng et al. "Nature of continuous phase transitions in interacting topological insulators". In: *Phys. Rev. B* 96 (19 2017), p. 195118. DOI: 10.1103/PhysRevB.96.195118. URL: https://link.aps.org/doi/10.1103/PhysRevB.96.195118.

[105] Robert Schaffer, Subhro Bhattacharjee, and Yong Baek Kim. "Quantum phase transition in Heisenberg-Kitaev model". In: *Physical Review B* 86.22 (2012). ISSN: 1550-235X. DOI: 10.1103/physrevb.86.224417. URL: http://dx.doi.org/10.1103/PhysRevB.86.224417.

[106] Sandro Sorella, Yuichi Otsuka, and Seiji Yunoki. "Absence of a Spin Liquid Phase in the Hubbard Model on the Honeycomb Lattice". In: *Scientific Reports* 2.1 (2012), p. 992. DOI: 10.1038/srep00992.

ECOLE
DOCTORALE

Titre : Effet de proximité topologique dans les systèmes bicouches et approche stochastique des phases topologiques fortement corrélées

Mots clés : Phases topologiques, modèle bicouche, physique de Mott, phases fortement corrélées

Résumé : Ces dernières décennies, de grands progrès ont été réalisés dans la description des phases de la matière quantique au-delà du paradigme de Ginzburg-Landau. Parmi les développements les plus cruciaux figure l'observation expérimentale de l'effet Hall quantique par von Klitzing. C'est ensuite Haldane qui a développé un modèle simple et élégant - le modèle prototypique d'un isolant de Chern - qui présente un effet Hall quantique sans la nécessité d'un champ magnétique externe appliqué. Près de vingt ans après la publication de Haldane, Kane et Mele ont décrit l'effet Hall quantique de spin (QSHE).
Dans cette thèse, nous explorons la riche phénoménologie du modèle de Haldane ainsi que du modèle de Kane-Mele dans un contexte de nouvelles interfaces et d'effets des correlations fortes. Nous étudions d'abord le modèle Haldane-graphène bicouche et révélons un effet de proximité intrigant qui permet d'induire un indice topologique dans le graphène. Nous explorons en détail la riche phénoménologie de ce système. De manière importante, nous présentons des protocoles expérimentaux conçus pour révéler les effets. En particulier, nous proposons un modèle de Haldane bicouche généralisé qui est conçu pour observer l'effet de proximité topologique dans un contexte expérimental d'atomes froids.
Ensuite , nous étudions le modèle de Haldane avec des interactions fortes. Nous développons un schéma de découplage stochastique, calculons la ligne de transition de Mott soutenue par des calculs iDMRG et confirmons la nature de premier ordre de la transition de phase au moyen d'arguments de Ginzburg-Landau. Ensuite, nous proposons une nouvelle quantité appelée *nombre de Chern stochastique* qui fournit une mesure de la topologie du système en présence de fortes corrélations. Nous utilisons le dichroïsme de la lumière pour faire le lien dans la quantification des quasi particules excitées et montrons une analogie entre les paires de particules-trous induites par correlation et les effets de température.
Enfin, nous étudions la transition de Mott dans le modèle de Kane-Mele-Hubbard en appliquant notre schéma de décomposition stochastique variationnelle. Nous comparons deux types de théories de champ moyen dont l'une fournit une expression analytique décrivante la ligne de transition de Mott.

Title : Topological proximity effect in bilayer systems and stochastic approach to interacting topological phases

Keywords : Topological phases, bilayer model, Mott physics, strongly-correlated phases

Abstract : The past decades have shown great progress in the description of phases of quantum matter beyond the Ginzburg-Landau paradigm. Among the most crucial developments was von Klitzings experimental observation of the quantum Hall effect. It was then Haldane who developed a simple, elegant model - the prototypical model of a Chern insulator - that exhibits a quantum Hall effect without the necessity of an applied external magnetic field. The, almost twenty years after Haldane seminal paper, Kane and Mele described the Quantum Spin Hall Effect (QSHE).
In this thesis, we explore the rich phenomenology of the Haldane honeycomb model as well as the Kane-Mele model in a context of novel interfaces and interaction effects. First we study the Haldane-graphene bilayer model and reveal an intriguing proximity effect that allows to induce a topological index into the bulk of graphene. We explore in detail the rich phenomenology of this system. Importantly, we present experimental protocols designed to reveal the effects. In particular, we propose a generalized Haldane bilayer model that is designed to observe the topological proximity effect in a cold atom experimental setup.
Furthermore, we study the Haldane honeycomb model with nearest neighbor interactions. We develop a stochastic decoupling scheme, compute the Mott transition line supported with iDMRG calculations and confirm the first order nature of the phase transition by means of Ginzburg-Landau arguments. Then, we propose a new quantity dubbed *stochastic Chern number* which provides a measure for the topology in the system in the presence of strong correlations. We utilize the dichroism of light to build a bridge in quantifying excited quasi particles and show an analogy between interaction induced particle-hole pairs and temperature effects.
Finally, we study the Mott transition in the Kane-Mele-Hubbard model by applying our variational stochastic decomposition scheme. We compare two kinds of mean field theories where one of them provides a closed analytic expression for the Mott transition line.

Institut Polytechnique de Paris
91120 Palaiseau, France